Summer 2016

Spectroscopic studies of silica nanoparticles: magnetic resonance and nanomaterial-biological interactions

Sean E. Lehman
University of Iowa

SPECTROSCOPIC STUDIES OF SILICA NANOPARTICLES: MAGNETIC RESONANCE AND NANOMATERIAL-BIOLOGICAL INTERACTIONS

by

Sean E. Lehman

A thesis submitted in partial fulfillment
of the requirements for the Doctor of Philosophy
degree in Chemistry in the
Graduate College of
The University of Iowa

August 2016

Thesis Supervisor: Professor Sarah C. Larsen

Graduate College
The University of Iowa
Iowa City, Iowa

CERTIFICATE OF APPROVAL

PH.D. THESIS

This is to certify that the Ph.D. thesis of

Sean E. Lehman

has been approved by the Examining Committee for
the thesis requirement for the Doctor of Philosophy degree
in Chemistry at the August 2016 graduation.

Thesis Committee: _____
Sarah C. Larsen, Thesis Supervisor

_____
Vicki H. Grassian

_____
M. Lei Geng

_____
Leonard R. MacGillivray

_____
Markus Wohlgenannt

I dedicate this work to my parents, who always encouraged me to walk my own path.

“Yet such is oft the course of deeds that move the wheels of the world:
Small hands do them because they must, while the eyes of the great are elsewhere.”
-J. R. R. Tolkien.

“It doesn't matter how beautiful your theory is.
It doesn't matter how smart you are.
If it doesn't agree with experiment, it's wrong.”
-Richard P. Feynman.

ACKNOWLEDGEMENTS

A great many people contributed to the work contained in this thesis. However, without the contributions from these people, none of this work would have come to pass in the form it takes now. I must first acknowledge the deep and varied contributions of my thesis supervisor, Professor Sarah Larsen. You have been an outstanding mentor to me, and I thank you for giving me the opportunity to work with you, as well as a great deal of freedom to pursue projects in my own way as I chose. You have inspired me to teach, to mentor, and be fair but kind. We have not always agreed, but you have always respected my opinion as a scientist. For that, I am deeply grateful to you. You were the best advisor I could have asked for.

I would like to thank the many faculty at the University of Iowa who I have worked with/for and learned much from. I am particularly indebted to Professor Vicki Grassian, from whom I have gained learned much of what I know about surface chemistry and thermodynamics. I also thank Professor Gary Small who I have taught with many times. I very much enjoyed all the time we spent together in the classroom and the laboratory, the freedom you allowed me in my instruction, and the opportunity to learn from you to be a better teacher.

I must thank all of the many staff in the Chemistry Building who assisted me in many ways throughout my years here. Sharon and Janet who kept things running smoothly, and now Lindsay who has taken over for Sharon, as well as Shelli in the front office for scheduling so many things at different times and for different reasons. I also extend my gratitude to Dr. Santhana Velupillai in the UI NMR Facility. Your encyclopedic knowledge of modern NMR spectroscopy is awe-inspiring and you have

helped me many times throughout my research here. I also thank Dr. Fu Chen for his assistance with solid-state NMR experiments.

I thank all of past graduate students in the Larsen Research Group who helped me in different ways at different times: Dr. Ashish Datt, Dr. Yulia Tataurova, and Dr. Paul Mueller. I wish to thank my colleague Shani Egodawatte who has been a great lab friend to me and who helped me many times. I also extend my thanks to my collaborator Angie Morris who worked on many things with me, and taught with me many times. I also thank my excellent undergraduate Alyssa Hopman who worked very hard for me for quite some time. I also want to thank all of my good friends including Andrea, CJ, Veronica, and AB for all the fun times we have spent together in and out of the lab. I also thank all of my dear friends from my incoming group (Michael, Nick, Mitch, Katie, Jon); you have made this all much more enjoyable than it would have been without you and I have enjoyed the journey with you. I also thank all of my students (~300) who I have taught during my time here. I have learned from all of you even as you learned from me.

Finally, I express deepest gratitude to my undergraduate advisor, Professor Cindy Strong. Under your gentle instruction I learned the rudiments of being a modern scientist. You set me on this path long ago, and taught me what it means to be a scientist. I would not be the scientist I am today without your guidance. I offer my thanks to all of my friends and family, and many other people too numerous to mention who have helped me along the way with words of advice or encouragement. The work in this thesis is yours as well, in some small measure. It has been a fun journey. Thank you all for your help.

S.E.L.
Iowa City, IA
August 2016

ABSTRACT

Primarily concerned with manipulation and study of matter at the nanoscale, the concept of nanoscience encompasses ideas such as nanomaterial synthesis, characterization, and applications to modern scientific and societal problems. These problems encompass a broad range of issues such as energy storage and conversion, medical diagnostics and treatment, environmental remediation and detection, carbon economy and as well as many others. Silica nanoparticles of porous morphology have broad application to many of these issues. In particular, the utility of silica nanoparticles is facilitated by their large intrinsic surface area, tunable surface chemistry, and synthetic variability in both their size and morphology. This facilitates applications to these problems. However, extensive characterization and deeper understanding is needed before full implementation in key applications can be realized.

The work described in this thesis aims to explore fundamental and applied characterization of silica nanoparticles that might be used in biomedical and environmental applications. Fundamental studies of functionalized nanomaterials using NMR spectroscopy reveal complex, dynamic phenomena related to-and ultimately deriving from-the intrinsic and/or modified surface chemistry. Applied studies of nanomaterial-biological interfaces demonstrate free radical chemistry as dominating the toxic response of the materials when exposed to biological systems of interest. Characterization of protein adsorbed on the interface reinforces the ubiquitous nature of protein adsorption on nanomaterial surface in biological and environmental media. Overall, this work illuminates and highlights complex changes that take place in aqueous solution for silica nanoparticles of varied morphology and surface chemistry.

PUBLIC ABSTRACT

Nanoscience and nanotechnology are emergent interdisciplinary areas of research and development. Nanoscience is concerned with materials that have dimensions on the order of 1 to 100 nanometers, which is a billionth of a meter. These materials are manipulated on the smallest scale currently possible. The ability to design, synthesize, and manipulate matter on this scale gives us the capability to fundamentally control the properties of matter at a high level of precision. This ability enables nanoscientists to design and manufacture materials for various applications of interest to the public including energy storage for better, longer-lasting batteries, and stronger, enhanced materials for use in everyday lives. However, the growth of nanoscience has only taken off in the last decade or so to become a field of immense scientific and creative endeavors. Silica nanoparticles are small particles of the amorphous glass we commonly encounter and use every day.

The applications of silica nanoparticle are wide-ranging and broad in application. However, there is still a great deal of fundamental understanding lacking to modern nanoscientists. The work reported in this thesis seeks to explore and expand this fundamental understanding in terms of how these particles react and behave when placed into environmental or biological aqueous compartments. By using advanced chemical characterization, this thesis advances knowledge about how we can design better materials to be less toxic to humans and animals, to be safer for the delivery of drug molecules to specific sites, and how to understand modifications to the materials that occur when the materials are exposed to biological solutions. The outlook for these materials is very positive, but studies like these are needed for a complete understanding.

TABLE OF CONTENTS

LIST OF TABLES

LIST OF FIGURES

CHAPTER 1
INTRODUCTION

1.1 Silica Structure and Physicochemical Properties

Mesoporous silica is a porous, amorphous material composed of silica tetrahedra covalently bonded to generate a solid network.[1] The material can be synthesized as a nanomaterial through controlled synthetic conditions.[2] Silica nanoparticles are currently in development for biological, environmental, and catalytic applications, among others.[3] The pores of the material manifest through controlled reaction conditions involving a surfactant. In the general reaction to prepare nanoscale silica, a silicon source such as tetraethylorthosilicate (TEOS) is hydrolyzed under aqueous conditions and then condensed to form the material. This can be represented schematically in the reactions given below:

Hydrolysis: $Si(OCH_2CH_3)_{4(aq)} + 2H_2O_{(l)} \rightarrow Si(OH)_{4(aq)} + 4CH_3CH_2OH_{(aq)}$

Condensation: $(HO)_3Si\text{-}OH_{(aq)} + HO\text{-}Si(OH)_{3(aq)} \rightarrow (HO)_3Si\text{-}O\text{-}Si(OH)_{3(s)} + H_2O_{(l)}$

The size of the synthesized silica particles depends on the solution conditions, primarily concentration of the relevant species.[2] The general hydrolysis reaction is catalytically accelerated by addition of acid or base. To generate materials of a controlled porosity, a surfactant molecule such as cetyltrimethylammonium bromide (CTAB) is added to the solution. In a process that is still not completely understood, the surfactant molecules first self-assemble into micelles, then the micelles self-associate to generate rod-like structures.[2] The silica condenses around these surfactant molecules as the reaction proceeds. The surfactant is then removed via calcination in air, or by using a solvent extraction procedure. This affords the porous silica material after the templated surfactant

molecules have been removed. A typical synthesis for the mesoporous silica known as MCM-41 is shown below.

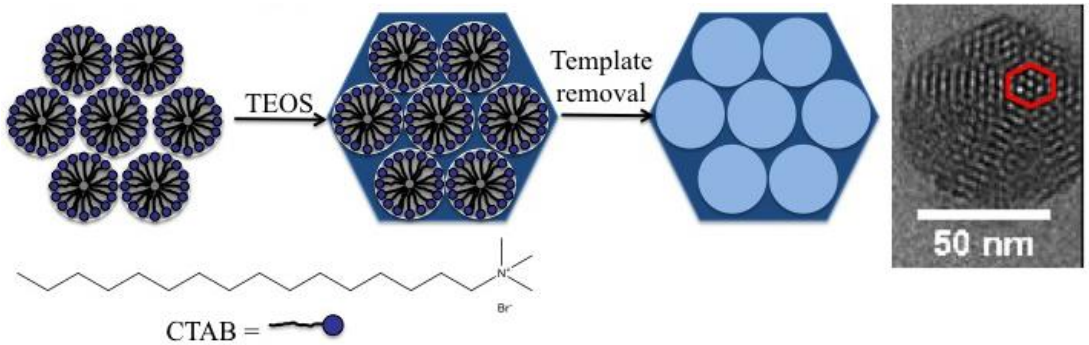

Figure 1.1 Mesoporous silica synthesis proceeds by the formation of micellar rods of the surfactant. The silicon source condenses around the rods and is removed, giving the mesoporous material. The image on the right is an actual TEM image of MCM-41. [Reproduced with permission from Reference 3. Copyright 2014, Royal Society of Chemistry.]

Mesoporous silica, by definition, has pores of 2-50 nm in diameter.[4] The size and exact arrangement of the pores in the material is controlled by the synthesis conditions. The porosity of the material gives rise to unique and advantageous properties such as a very large surface area ($\geq 1000\ m^2\ g^{-1}$). This large surface area facilitates heterogeneous processes such as adsorption or catalysis. Due to the structure consisting of SiO_4 tetrahedra covalently-bonded to each other, the surface terminates in silanol (Si-OH) moieties.

These moieties are chemically similar to alcohol moieties, although the silanol is orders of magnitude more acidic (pKa(Si-OH) ≈ 3.0 vs. pKa(C-OH) ≈ 15). Surface silanols are also quite nucleophilic, due to the oxygen atom, which enables a high reactivity for chemical modification. In the general reaction scheme, the surface silanols are reacted with a trialkoxysilane molecule ($(RO)_3$-Si-X) to install the X group onto the surface of the molecule. A wide variety of functionalities have been implemented including amine, thiol, carboxylic and sulfonic acids, amide, aldehyde, and others.[5]

The most commonly employed functionality is a propylamine such as aminopropyltriethoxysilane. More recently, even large polymeric functionalities such as polyethylene glycol (PEG) have been added to the surface of silica nanoparticles through multi-step cross-coupling approaches. Silica itself is quite stable in most aqueous solutions, is stable against acid and dilute base, and is mostly chemically inert in and of itself. These favorable chemical and physical properties, coupled with the rapid growth and development of nanotechnology and silica nanoparticles makes it a material worthy of many research efforts as can be currently seen in the rapid pace of publications on it.

Before the advent of mesoporous silica, Werner Stöber synthesized the nonporous variant known as Stöber silica over 40 year ago.[6] This synthetic procedure enables the preparation of solid silica nanoparticles of high homogeneity through controlled hydrolysis and condensation reactions identical to the chemical reactions described above. In this synthesis, no surfactant is utilized to give solid spherical silica particles. The synthesis is carried out in aqueous conditions using ammonia as a base, and silyl ethers such as TEOS are used as the silicon source. Varying types and amounts of short-chain alcohols are added to control the reaction, enabling a wide range of sizes to be prepared through controlled reactions.[7]

1.2 Nuclear Magnetic Resonance (NMR) Spectroscopy

This section describes fundamental aspects and the theory of NMR spectroscopy. This spectroscopic technique is widely used in modern chemical analysis to investigate every phase of matter including solids, liquids, and gases. This technique probes the local electronic structure of matter by using radiofrequency radiation in a static magnetic field. Several key aspects of the technique are described, including aspects that are directly related to the reporting of experimental data contained in later chapters of the thesis.

1.2.1 The NMR Experiment

NMR spectroscopy is a spectroscopic technique that principally depends on the presence of magnetic nuclei in chemical species. In nuclei with a non-zero spin angular momentum (spin), a magnetic moment manifests in the nucleus of the atom. This magnetic moment is then probed by the NMR experiment. A list of commonly encountered nuclei is shown below in Table 1.1 including their NMR-relevant properties.

Table 1.1 Selected Properties of Common Nuclei in NMR Spectroscopy.

Isotope	Spin	Natural Abundance (%)	Magnetogyric Ratio (MHz T^{-1})	Larmor Frequency (MHz) [B_0 =11.75 T]	Sensitivity (Relative to ^{1}H)
^{1}H	½	99.9885	42.58	500.00	1.000
^{2}H	1	0.0115	6.54	76.75	9.65×10^{-3}
^{13}C	½	1.07	10.71	125.75	1.59×10^{-2}
^{14}N	1	99.63	3.09	36.14	1.01×10^{-3}
^{15}N	½	0.368	-4.32	50.70	1.04×10^{-3}
^{17}O	5/2	0.038	-5.77	67.81	2.91×10^{-2}
^{19}F	½	100	40.08	470.34	8.32×10^{-1}
^{29}Si	½	4.68	-8.47	99.41	7.86×10^{-3}
^{31}P	½	100	17.25	202.59	6.65×10^{-2}

The magnetic moment (μ) and the spin angular momentum (I) are related by a fundamental physical constant known as the magnetogyric ratio (γ) in the relation:

$$\mu = \gamma I \qquad (1)$$

These are all nuclei-dependent properties and for the most commonly-interrogated nucleus, the proton (^{1}H), and the magnetogyric ratio is 267.5 rad s^{-1} T^{-1} or more

commonly given as 42.6 MHz T^{-1}. In the NMR experiment, a strong static magnetic field is applied in a single direction. In the presence of the magnetic field the degeneracy of the spin states of the nucleus is lifted. The proton (I=1/2), for example, has only two spin states in the presence of a magnetic field:

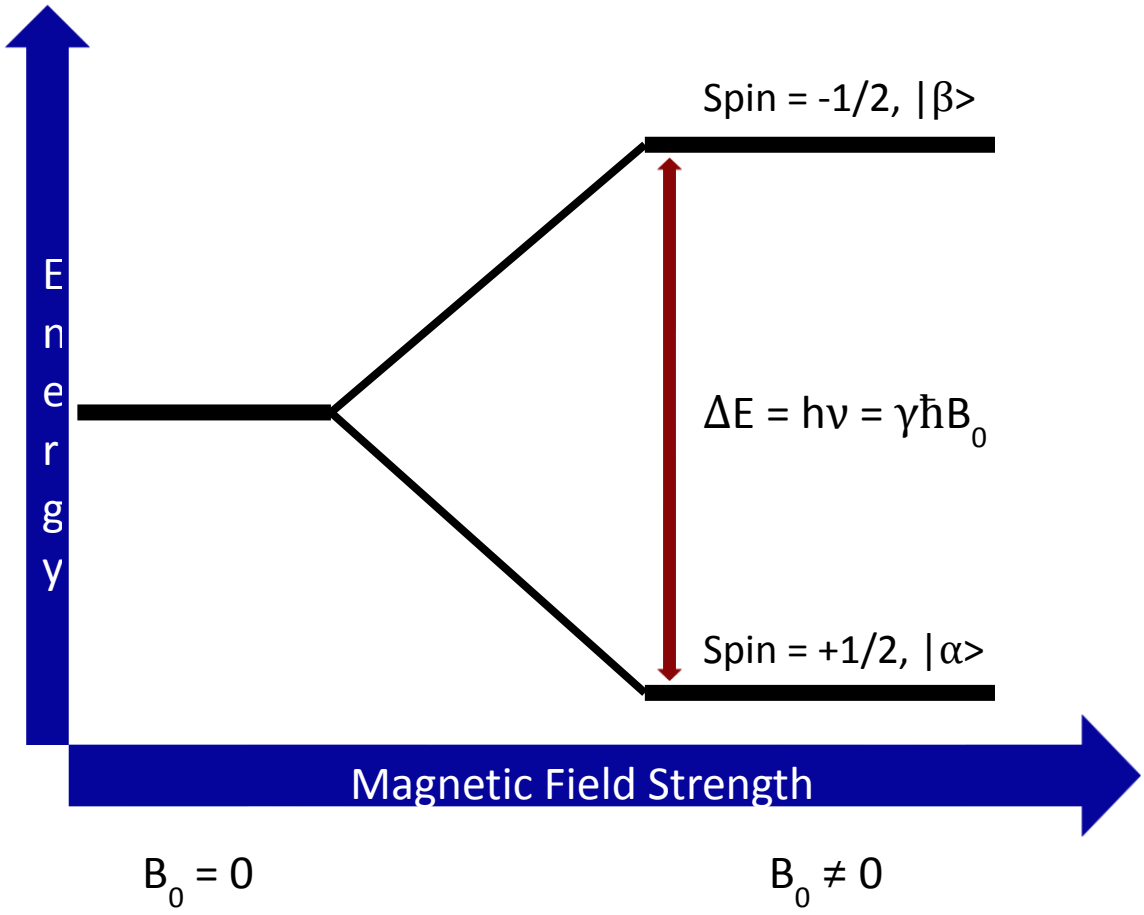

Figure 1.2 Energy splitting diagram for magnetic nuclei in the presence of a magnetic field.

The energy separation of the spin states is proportional to:

$$\Delta E = h\nu = \gamma \hbar B_0 \qquad (2)$$

Herein, γ is the magnetogyric ratio as described above, ħ is the reduced Planck's constant, and B_0 is the applied magnetic field strength (SI unit, Tesla). The population of

the spin states in the presence of the magnetic field is given by the Boltzmann population equilibrium:

$$\frac{N_\beta}{N_\alpha} = e^{-\Delta E/k_B T} \qquad (3)$$

Here N gives the population of the spin states, ΔE is the energy separation, k_B is Boltzmann's constant, and T is absolute temperature. As the energy separation between the nuclear spin states is quite small, the population of the lower energy state is only slightly in excess of the higher energy state, such that the population ratio is ≈ 0.99995 at 298 K and moderate magnetic field strengths (B_0 = 7.05 T, 300 MHz).

In modern NMR spectroscopy, it is exclusively executed as Fourier transform (FT-NMR). In the presence of the magnetic field, the nuclei precess about the field at a frequency proportional to the magnetic field strength. In a field of 9.40 T, for example, protons resonate around 400 MHz. This is given in terms of the angular frequency, ω_0:

$$\omega_0 = -\gamma B_0 \qquad (4)$$

Different nuclei will resonate at different frequencies due to their different magnetogyric ratios. For ^{13}C nuclei, the resonance frequency is closer to 100 MHz in an applied field of 9.4 T. Due to local electronic effects, the protons have different exact resonance frequencies depending on their local electronic structure. This dependence on the local electronic structure is referred to as the chemical shift.

In an NMR experiment, a pulse of radiofrequency (rf) radiation is used to induce transitions between the spin states. As the population of the lower energy state is in excess, this results in a net absorption of radiation. In the classical regime, the excess of nuclei in the lower energy state (which is aligned with the field) gives rise to a net bulk magnetization upon summation of the individual magnetic moments of the nuclei.

Application of the rf field perpendicular to the applied magnetic field shifts the bulk magnetization from its equilibrium value. Irradiation with a so-called 90 ° pulse (also referred to as a $\pi/2$ pulse) equalizes the spin states and-in Cartesian space-tilts the bulk magnetization into the xy plane. This gives rise to a transverse magnetization that is spectroscopically detectable.

Once the magnetization is perturbed from its initial value then the molecules undergo relaxation processes, which restore the Boltzmann equilibrium. This then tilts the bulk magnetization back to align with the magnetic field. However, the nuclei continue to precess about the field as relaxation through various mechanisms. The net effect is that the bulk magnetization wraps into a spiral that decays back to the equilibrium position of alignment with the static magnetic field. When a magnetic moment is moved through a static field it fundamentally generates a current. A coil wrapped around the sample in the NMR spectrometer is used to detect this current. However, the intrinsic resistance of the coil modulates the current, which is ultimately detected as a voltage (via Ohm's Law).

The voltage is an oscillating sinusoidal wave, which is damped due to relaxation. This can be given a generic mathematical form using both the real and imaginary parts as:

$$S(t) = S_0 \, (\cos \Omega t + i \sin \Omega t) * e^{-t/T_2} \qquad (5)$$

S is the observed signal at time t, S_0 is the initial maximal signal (corresponding to the initial amount of magnetization in the xy plane), Ω is the frequency offset from the exact Larmor frequency, and T_2 is a characteristic transverse relaxation time of the system, which will be described in the next section. The exponential in the second portion describes the damping effect of relaxation on the observed signal. In this case, the signal is detected as a time-domain signal as the Boltzmann population is restored through

relaxation processes. Fourier transformation of the time-domain signal gives rise to a frequency-domain signal that is the NMR spectrum. This gives spectral intensity as a function of energy. Due to the small shifts in frequency from the Larmor frequency of each nucleus, the signal is often given in relative units by calculating thus:

$$\delta\ (ppm) = \frac{\nu_{sample} - \nu_{reference}}{\nu_{reference}} * 10^6 \quad (6)$$

In this case the measured frequencies are referenced to a standard material's resonant frequency agreed upon (commonly tetramethylsilane, TMS) and then multiplied by the factor of 10^6 to give the frequencies in field-independent units of ppm chemical shift.

1.2.2 Spin-Lattice (Longitudinal) Relaxation

Once the magnetization is perturbed from the equilibrium value, by a π/2 pulse for example, the magnetization in the z-direction (Cartesian coordinates) is zero. However, it immediately begins to be restored through the process known as spin-lattice relaxation. This can be described by a Bloch equation, which is a differential equation given as:

$$\frac{dM_z}{dt} = -\frac{M_z - M_0}{T_1} \quad (7)$$

In this, M_z is the magnetization in the z direction, M_0 is the equilibrium magnetization, and T_1 is the characteristic time for the process known as the spin-lattice relaxation time. This is given in its integrated form to describe the magnetization as a function of time:

$$M_z(t) = M_0(1 - e^{-\frac{t}{T_1}}) \quad (8)$$

For protons in fluid solution, T_1 is around a few seconds whereas for ^{13}C it can be tens or even hundreds of seconds depending on the molecular structure. Many mechanisms contribute to this process, but the primary cause in NMR is dipole-dipole coupling. In fluid-solution, the molecules move rapidly (translation) on the timescale of the NMR experiment. This rapid motion generates a local magnetic field that fluctuates rapidly in

time. The field fluctuations induce transitions of the nuclei between spin states, and thus the Boltzmann population is restored through these fluctuations. The efficiency of this process is maximized when the frequency of the molecular motion is very close to the frequency at which the nuclei are precessing in the NMR experiment.

1.2.3 Spin-Spin (Transverse) Relaxation

Upon the initial irradiation of the nuclei by the π/2 pulse, the nuclear magnetic moments are aligned and in-phase in the xy plane. This phase coherence only exists for a short time before it is broken. The sample of nuclei probed in the NMR experiment has a finite volume, but the magnetic field, which passes through this volume, is not perfectly homogeneous. Therefore, each nucleus experiences a slightly different frequency as it moves through the solution. This in turn causes nuclei in different parts of the probed volume to experience a different local magnetic field, which causes dephasing to occur. Thus, as the spin packet evolves in time, the initial phase coherence is lost. This can be similarly described by a differential equation similar to that given in the previous section:

$$\frac{dM_y}{dt} = -\frac{M_y}{T_2} \qquad (9)$$

Here M_y is the magnetization in the y-plane and T_2 is the characteristic spin-spin relaxation time. The practical effect of the spin-spin relaxation is that the dephasing of the nuclear spins causes the magnetization in the xy plane to decay in time. Since the only detectable portion of the magnetization is that which is in the xy plane, this causes the measured induced voltage to decay exponentially as the experiment proceeds. The ultimate consequence of this is that the decay time is directly related to the spectral linewidth. In an analogous fashion to Heisenberg's uncertainty principle, the more quickly the dephasing takes place (i.e. the shorter the spin-spin relaxation time) the larger

the spectral linewidth will be in the final spectrum. This can be given in terms of the full-width at half-max (FWHM):

$$FWHM = \frac{1}{\pi T_2^*} \qquad (10)$$

In this case, the time T_2^* is the observed spin-spin relaxation time, which is given as the sum of two factors: homogenous broadening which arises by spin-spin relaxation as dephasing occurs, and inhomogeneous broadening caused by the intrinsic heterogeneity of the applied static magnetic field.

1.2.4 Two-Dimensional NMR Techniques

The standard NMR experiment described above allows for the determination of a wealth of chemical information. However, this 1D experiment is unable to probe higher-order effects of interest in modern chemical science. In order to probe things like ligand binding and exchange or spatial relationships in molecules, 2D NMR spectroscopy has been developed. The general scheme involves an expansion of steps from the 1D experiment. The approach is to wait for a period of time known as the preparation phase (d_1), then use an initial pulse of radiation to perturb the nuclei (p_1), allow the system to undergo an evolution phase for a time t_1 (not the same as T_1) and then apply another pulse of radiation (p_2). After the second pulse an amount of time is allowed to pass known as the mixing time (T_{mix}). Following the mixing time, the signal is directly collected. This can be represented as:

$$d_1 - p_1 - t_1 - p_2 - T_{mix} - FID(Detection) \qquad (11)$$

In a given experiment, T_{mix} is held constant, and t_1 is incremented. Thus a FID is collected for each value of t_1. By Fourier transformation of each individual FID, and then the collected t_1 values, a 2D plot of the data can be generated. A common use of this is to

measure a 2D spectrum looking at the Nuclear Overhauser Effect (NOE). This NMR experiment is referred to as 2D NOESY (Nuclear Overhauser Effect SpectroscopY). The NOE manifests as an interaction between nuclei that lie close to each other in space. This interaction can also be used to probe phenomena such as ligand exchange or binding.

1.3 Electron Paramagnetic Resonance (EPR) Spectroscopy

The following section discusses fundamental aspects of the analogous magnetic spectroscopy experiment for species containing an unpaired electron. The general principles remain similar, although the experiment is different for fundamental physical reasons. The primary fundamental theory behind EPR is described to provide a framework for discussion of the spectral features and their relation to chemical structure and insight. A brief description of spin trapping is given to provide a general overview of strategies to detect and obtain EPR spectra of radical species with short lifetimes.

1.3.1 The EPR Experiment

In chemical species containing at least one unpaired electron, an analogous experiment to NMR is possible. The type of spectroscopic interrogation of the unpaired electron spin is known as electron paramagnetic resonance or electron spin resonance. The interaction of the magnetic field with the magnetic moment of the electron lifts the degeneracy of the two spin states. Thus, transitions are possible when the correct combination of magnetic field and irradiation occurs. This can be given by:

$$\Delta E = h\nu = g_e \mu_B B_0 \quad (12)$$

Here g_e is the electronic g-factor, a constant of proportionality, μ_B is the physical constant known as the Bohr magneton, and B_0 is the applied magnetic field strength. In the EPR experiment, it is commonly executed as a continuous wave (CW) experiment. In CW-

EPR, the sample is irradiated under a constant frequency, and the magnetic field is swept through a range of values. Changes in the absorption of the applied radiation are measured as the resonant absorption on a spectroscopically detected line or lines. Due to the much larger magnetic moment of an electron compared to nuclei, the frequency/field combination is much higher than that used in NMR. In a typical EPR experiment, the applied radiation is around 9.7 GHz, and thus the applied magnetic field is around 0.3 Tesla (T). The electronic g-factor for a free electron is given as 2.0023193043618(5) as the currently accepted value. The Bohr magneton has a currently accepted value $927.400999(6) \times 10^{-26}$ J T^{-1}. Organic radicals typically have electronic g-factors near the free electron, but for transition metal complexes the g-factor is highly variable.

1.3.2 Spectral Parameters: Electronic g-Factor and Hyperfine Coupling

The most important spectral parameters for EPR spectroscopy are the electronic g-factor and the hyperfine coupling constants. The electronic g-factor, as described above, is directly related to the structure of the complex that contains the unpaired electron. The magnitude of the g-factor is primarily dependent on the spin-orbit coupling the electron experiences. This is dependent on the atom on which the electron localizes, and is ultimately characteristic of the complex involved.

The hyperfine interaction manifests due to the interaction of the magnetic moment of the free electron with non-zero spin nuclei it is located on. In effect, this causes a further splitting of each of the energy levels of the electron into several energy levels. In general, the splitting of the electron can be represented in the diagram below (Figure 1.3). In this you see the initial splitting of the spin states by the application of the magnetic field, then the further splitting into sublevels by the interaction with a nearby nuclear

spin, in this case of I = ½. In general the splitting of a single electron gives rise to 2NI+1 sublevels, where I is the nuclear spin and N is the number of equivalent nuclei:

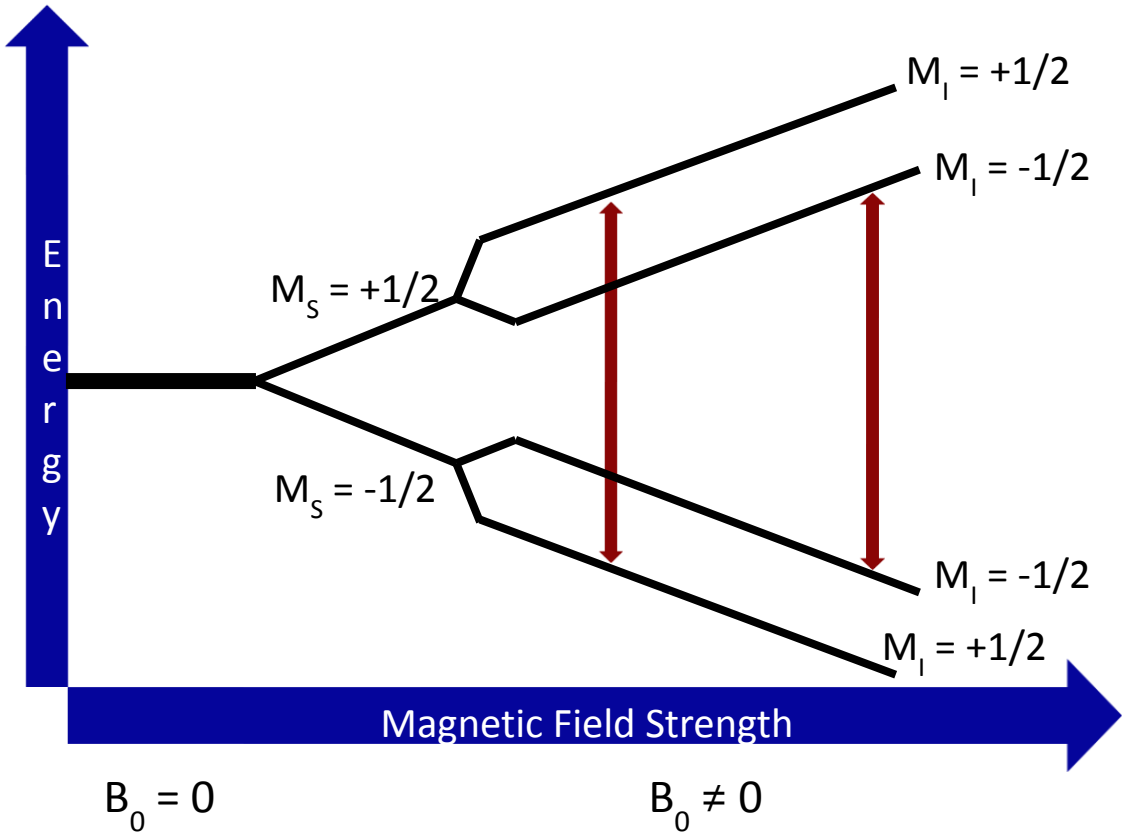

Figure 1.3 Energy level diagram of EPR spectroscopy. The application of the magnetic field first splits the lines into two energy levels corresponding to the two spin states of the electron. Upon interaction with a single I = ½ nucleus, each level is split into sublevels. The allowed transitions are shown between the sublevels, which result in two lines in the EPR spectrum upon meeting the resonance condition.

The hyperfine coupling gives direct structural information about the nuclei and their location of the unpaired electron in the molecule. The hyperfine couplings are directly measured off the spectrum and are typically given in units of gauss (G) or milliTesla (mT). The SI unit of magnetic field strength is tesla (T), and 10,000 G = 1 T. However, hyperfine couplings are quite small, on the order of 10 G in most cases, so it is impractical to give them in units of T, which is why gauss or mT are used instead.

1.3.3 Spin-Trapping Experiment

Transition metals and many types of organic radicals form temporally-stable complexes in that can be detected using EPR. However, many types of radicals are transient on the timescale of the EPR experiment and so cannot be directly detected. Therefore, the approach implemented if solution-phase measurements are desired is to spin-trap them. In this technique, the radical of interest is allowed to react with an organic molecule that can generate a so-called spin adduct that has a long enough lifetime in solution for spectral detection:

$$R^{\bullet} + ST \rightarrow R - SA^{\bullet}$$

In this reaction, the species containing the free radical (R•) reacts with the spin trap (ST) and forms the spin adduct (SA). A covalent bond forms between the free radical species and the spin trap, giving rise to a covalently-bonded complex with a sufficient lifetime for spectroscopic detection. The most common of these are the nitrone spin traps such as DMPO and PBN. These spin adducts localize the free electron onto a more electronegative atom such as nitrogen or oxygen and generally possess a large amount of steric bulk which gives them substantial lifetimes in solution.

1.4 State-of-the-Art on Silica Nanomaterial Toxicity

Mesoporous silica has seen great strides in recent years as a possible drug delivery vehicle due to increased cellular uptake of nanoscale materials.[8] However, an associated concern that has risen concomitantly is the concern of physiological toxicity. One of the primary themes that has emerged is that physical structure plays a decisive role in mesoporous silica toxicity with specific emphasis placed on the external surface area.[9] Crystallinity of silica also plays a key role in toxicity. When compared to

crystalline materials such as quartz, mesoporous silica, with its amorphous structure exhibits greatly attenuated toxicity against *in vitro* cell lines.[10] *In vitro* studies involving various cell lines demonstrate a very low (below detection limit) amount of silica hydrolysis. Recent work in nanotoxicity has revealed a profound effect of the release of chemically modified species from nanoparticles.[11] Not surprisingly, this matches up well with the low levels of toxicity of mesoporous silica, even in comparison with other amorphous silicas, such as fumed silica.[12]

Haynes and co-workers further clarified the immune response of mesoporous silica using a highly innovative amperometric assay to visualize release events of mast cell granules following uptake of silica and titania (TiO_2).[9] The outcome of this work demonstrated that even though mesoporous silica exhibits increased cellular uptake, lower toxicity seems to result from less reactive surfaces for particle-cell interactions.[9] Other work has focused on hemolytic activity of mesoporous silica and confocal imaging of *in situ* particles to assess distribution in human liver cells.[13,14] This is important in terms of the viability as a drug delivery vehicle as previous work in this area has demonstrated that mesoporous silica can be shunted from the systemic circulation, accumulating in the liver and spleen.[15] Any positive effects of a drug delivery-type application would be negated while negative effects of bioaccumulation in these organs would naturally increase.

Silica toxicity is directly correlated to the surface silanol functionality (Si-OH). These moieties participate in hydrogen-bonding interactions and have well-documented acid-base properties arising from the acidity of the silanol proton ($pK_a \approx 3.0$). At physiological pH (≈ 7.4), silanol groups are uniformly deprotonated across the surface as

silicate anions ($Si\text{-}O^-$). This uniformly negative charge at the surface can interact with positively-charged tetraalkylammonium $(N\text{-}R_4)^+$ phospholipids in cellular membranes. These interactions can entropically disrupt the membranes leading to cellular lysis and expulsion of intracellular fluid and contents into the surrounding tissue. Work from just the last few years has elucidated the correlation between surface silanol density and toxicity. This was used to explain the decreased toxicity of MCM-41 type silica in comparison to other similar mesoporous silica materials, like SBA-15.[16] Due to the different ways the silicon is hydrolyzed and ultimately condenses around the surfactant constructs, the intrinsic amounts of free silanols on the surfaces of MCM-41 and SBA-15 are quite different. This difference leads to differences in observed toxicity, even between these different forms of mesoporous silica. The toxicity attributed to surface silanols can be directly mitigated by functionalization of the surface, but the overall surface charge must also be considered. Mesoporous silicas have lower surface silanol densities, and thus provoke a lower toxic response than nonporous silicas.[13] Zhang et al. used Raman spectroscopy to identify three-membered siloxane rings in fumed silica samples that are not observed in mesoporous silica.[17] Homolytic cleavage of these strained siloxane rings can ultimately give rise to different types of radicals including hydroxyl radicals via the proposed scheme shown in Figure 1.4.[12, 18]

As expected, *in vivo* studies are much less prevalent, even in the recent literature. One surprising finding is that even though mesoporous silicas show very little tissue toxicity, they do appear to invoke a systemic response. Hudson and associates revealed that death of mice subjects exposed to mesoporous silica was possibly due to thrombosis, the formation of blood clots within the circulatory system.[19] This is not apparent from the

multitude of *in vitro* studies. This is further enhanced by work carried out by Yu et al. which demonstrated that mesoporous silica accumulated in lung tissue to a greater degree than nonporous silica of a very similar size.[20] One caveat of this is that previously established work has shown lower accumulation by phagocytic mechanisms, implying that truly nanoscale materials may have decreased clearance *in vivo*.[21]

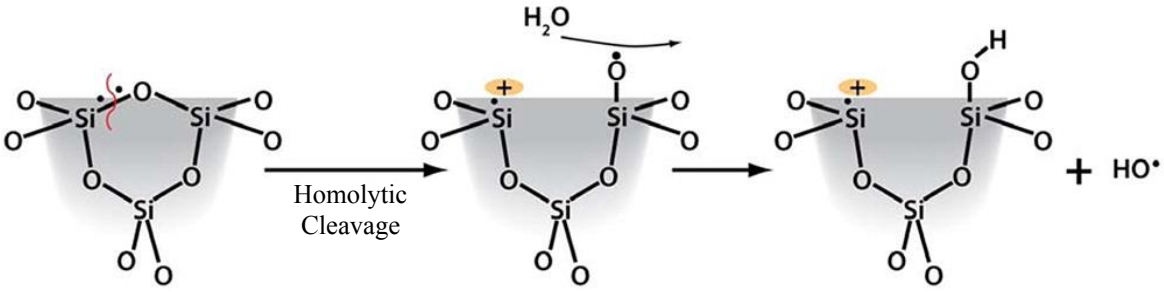

Figure 1.4 Proposed reaction of six-membered strained siloxane rings to form hydroxyl radicals. Reprinted with permission from Reference 11. Copyright 2012, American Chemical Society.

A major theme that has emerged is that toxicity is associated with formation of reactive oxygen species (ROS), such as •OH radicals. ROS have been linked to oxidative stress *in vivo* and studies suggest this may be a paradigm for nanoparticle toxicity. The method by which ROS causes damage leading to programmed cell death (apoptosis) or membrane disruption (necrosis) is not new. These destructive processes are the end product of cascade events triggered and proliferated by ROS. The formation of ROS in silica has been attributed to Fenton-like chemistry from the presence of trace iron. *In vivo*, the cellular concentration of free iron is kept very low due to tight binding to the transferrin protein. In fact, transferrin binds Fe^{3+} with overall formation constant $\beta = 1.1 \times 10^{31}\ M^{-2}$, but this low level of iron may still result in generation of toxic ROS species.[22] Work by Ahmad and coworkers reveals that nanoparticle-derived ROS can overcome the natural cellular defense mechanism, glutathione-mediated redox chemistry.[23] Classically, species

like hydroxyl radicals can proliferate in free-radical reactions leading to oxidation of lipids, DNA damage, and production of even more damaging species such as highly reactive organic peroxynitrite ($R\text{-}ONOO^-$).[18] The reactions that produce such species have been previously described.[24] Recent developments detect ROS in amorphous silica, in the absence of iron, and ROS production has been linked to highly strained three-membered siloxane rings which can undergo cleavage leading to radical generation at the particle surface.[12]

Free radicals have been implicated as the possible ultimate toxicant in these sorts of complex systems. Reactions at the surface of the silica nanoparticles may generate dangerous ROS, which can cause cellular havoc in biological systems. The mechanism of damage is well-described and can lead to cell death, programmed or otherwise. Work on nonporous silicas seems to suggest that the production of these species arises from a Fenton-like chemistry associated with trace amounts of heavy metal ions.[25] This was believed to have been the case with mesoporous silica, but has since been disproved. Instead, what appears to be the primary mechanism by which these ROS species are formed from mesoporous silica is from differential chemistry ultimately stemming from the surface silanols.[12]

The ultimate question that arises is how this apparent toxicity can be mitigated. The overarching answer seems to be surface differentiation. Strategies vary from functionalization by alkylamine or other organic functional moieties to gross PEG-ylation by larger polymeric molecules. The literature has established a marked decrease in toxicity with amine functionalization of the surface.[26] This seems to be a convergent effect between the addition of the functional moiety with an overall change in effective

surface charge in aqueous media. Yet some new work in the field has demonstrated that the linkage is perhaps not as direct as once thought.[27] Polymeric functionalization of the surface is clearly complicated by any adjoining functionalities. In this case, a PEG-quaternary ammonium $(R\text{-}N\text{-}Me_3)^+$ cation (whose charge is pH-independent) showed a significantly different response from a PEG-tertiary amine $(R\text{-}N\text{-}R_2)$.[27] One interpretation of this is that the surface chemistry plays perhaps the most critical role in determining toxic response. Reducing the free silanols, whether through surface functionalization or physical modification of the surface, are simply different means to the same end. The chemical nature of the surface ultimately controls interactions, reactions, and biological fate.

1.5 Thesis Overview

The work contained in this thesis describes fundamental and applied spectroscopic studies of silica in aqueous and biological environments. Spectroscopy was used to interrogate native and functionalized materials to obtain an enhanced understanding of how these materials behave in aqueous solution and how they interact with biological systems. Chapter 1 describes the fundamental physical and chemical properties of mesoporous silica nanoparticles. Chapter 1 also provides necessary background and theory on the magnetic resonance spectroscopy (NMR and EPR) used to probe the nanomaterials in various ways. Finally, Chapter 1 gives a brief overview of the current state on silica nanomaterial toxicity.

Chapter 2 describes the experimental methodology used to synthesize and functionalize the silica nanoparticles used in this study. Three different types of materials including MCM-41 and WO-type mesoporous silicas, and a nonporous silica material were used in the studies reported here. Chapter 3 describes the traditional physical and chemical characterization methods used to study and understand fundamental materials properties such as surface area. A general overview of each technique is given, as well as the fundamental theory behind how each methodology facilitates measurement and understanding of material properties.

Chapter 4 describes the first set of studies, which is based on the application of NMR spectroscopy to probe ligands covalently bonded to the nanoparticle surface. These ligands are bonded in a supramolecular fashion, and their stability and dynamics were studied using solution-phase NMR. A variety of different solution-phase ^{1}H NMR methods were employed to provide a complete picture of the aqueous stability and dynamics of these surface ligands. Overall, a model of chemical dynamics on the surface of the nanoparticle was developed, which arises from molecule-dependent chemistry.

Chapter 5 is primarily concerned with understanding toxicological responses of engineered silica nanoparticles and relating this to surface phenomena. The primary method used was EPR spectroscopy to detect and confirm free radical species produced from the silica nanoparticle surface. The EPR was complemented with *in vitro* measurements to obtain a meaningful correlation between observed toxicity and measured ROS.

Chapter 6 is an expansion and extension of Chapter 5, and fundamentally discusses and describes changes that take place at the nanomaterial surface upon exposure

to biological growth media. Protein adsorption was measured and quantified using variety of optical spectroscopic methods including infrared and circular dichroism spectroscopy. This was complemented with thermogravimetric measurements to quantify the adsorption onto the nanoparticle surfaces. Overall this data enables a quantitative understanding of the silica nanoparticle surface upon exposure to biological environments.

Chapter 7 is an extension and application of the initial work described in Chapter 6. Smaller silica (~20 nm) was used to understand if there is a size-dependent effect. The same suite of solution-phase NMR methods was used to probe the structure and dynamics of ligands on the nanoparticle surface. Systematic studies of glycine adsorption were also carried out to provide molecular-level understanding of the interaction of silica nanoparticles with small organic molecules such as the amino acid glycine.

Chapter 8 provides an overall summary of the studies described in the thesis. In addition, they are put into the broader context and their impact on the field is estimated. The thesis concludes with a few suggestions for expanding the work contained herein to other systems or to obtain new knowledge that would build on the studies described in this work.

CHAPTER 2
SYNTHESIS AND SURFACE FUNCTIONALIZATION OF SILICA NANOPARTICLES

2.1 Synthesis of MCM-41-type Mesoporous Silica

The silica of MCM-41-type is characterized by amorphous silica condensed around hexagonally-ordered pore-voids. MCM-41 type silica was prepared following a modified procedure from the literature.[28] In this synthesis, cetyltrimethylammonium bromide (CTAB) was used as the surfactant and combined with NaOH in aqueous solution. This solution was allowed to stir overnight at RT before being heated to 80 °C. TEOS was again used as the silicon source and was added rapidly. After stirring for two hours at the same temperature, the reaction mixture was cooled to room temperature. The products were centrifuged, the solid re-suspended in water, and washed repeatedly to remove reactants. The solid product was then dried at 80 °C and calcined at 550 °C in a stream of air for six hours to give the porous material, which was then utilized in the experiments.

2.2 Synthesis of WO-type Mesoporous Silica

A different type of silica is wormhole (WO) silica. This is a porous silica material with pores that are less ordered than that of a material such as MCM-41. In this material, the pores are randomly interconnected and interrupt each other throughout the material. Mesoporous silica nanoparticles with a particle size of approximately 50 nm were synthesized according to the procedure described previously.[29] In the synthesis of wormhole-type mesoporous silica, cetyltrimethylammonium chloride (CTAC), ethanol, and water were combined and stirred at room temperature for approximately 10 min.

Triethanolamine (TEA) was added and the solution was allowed to stir for approximately one hour before being heated to 60 °C. Tetraethylorthosilicate (TEOS) was then added to the rapidly stirring solution at a rate of about 2 mL/min and the solution was stirred at 60 °C for 2.5 hours. The material was then isolated by centrifugation and washed with water and ethanol in triplicate. The obtained solid was dried overnight to give the silica.

2.3 Synthesis of Nonporous (Stöber) Silica

Stöber-type silica (NPS) was prepared following a modified procedure from the literature.[6] In this synthesis no surfactant was used, and 120 mL absolute ethanol was mixed with 6.0 mL of 28% aqueous ammonia and stirred for 5 minutes. TEOS was again used as the silicon source and 4.0 mL was added at room temperature. The reaction mixture was stirred at room temperature for 24 hours and then centrifuged to obtain the products, which were washed in triplicate with water and dried at 60 °C overnight to give the Stöber silica material.

2.4 Covalent Surface Modification via Post-Synthesis Grafting

2.4.1 Amine Surface Functionalization

Functionalization with amine groups was carried out by refluxing a mixture 4 g of aminopropyltriethoxysilane (APTES, Sigma) with 1.00 g of MSNs in 60 mL of toluene for 48 h. Then, the reaction mixture was centrifuged, washed with dichloromethane three times and dried overnight at 80^{o} C.

2.4.2 Carboxylic Acid Surface Functionalization

The carboxylic acid group was attached to the surface by reacting 500 mg MSNs with 4.0 g tri(ethoxysilyl)-propionitrile (Sigma) overnight under reflux in 40 mL toluene. The toluene was removed, and the material was washed with water in several rounds of

centrifugation. The particles were dried overnight at 80 °C before hydrolysis under reflux conditions in 9 M HCl for 12 hours to convert the nitrile to a carboxyl group (carboxyethylsilane, CES).

2.4.3 Polyethylene Glycol Surface Functionalization

In order to functionalize the nanoparticle surface with polyethylene glycol (PEG), first PEG-APTES was synthesized by adapting a literature procedure.[30] The PEG terminal-hydroxyl moiety was oxidized using Jones reagent to the carboxylic acid. The carboxy-functionalized PEG was condensed with APTES to afford the amide using a Dean-Stark apparatus to remove the water formed. The solvent used for the condensation reaction was 50 mL toluene. Residual solvent was removed using rotary evaporation to give a yellow residue. This material was then verified to be the PEG-APTES molecule via ^{1}H NMR. The conversion to the amide was confirmed via ^{13}C NMR by observation of a characteristic peak at δ = 169.6 ppm. To functionalize the surface, 200 mg of silica nanoparticles were dehydrated under reflux in 30 mL toluene for 24 hours. Then, 200 mg of PEG-APTES (0.26 mmol) was suspended in 10 mL THF, and added to the nanoparticle suspension. The reaction was further maintained under reflux for 48 hours. The solution was cooled to room temperature, the solvent was removed by rotary evaporation, and the materials were washed with 50:50 (v/v) water/ethanol in triplicate, centrifuging at 11,300 *g* for 20 min to sediment the nanomaterials. The materials were dried overnight at 70 °C.

CHAPTER 3
PHYSICAL CHARACTERIZATION OF SILICA NANOPARTICLES

3.1 Electron Microscopy

Electron microscopy is the premier methodology for obtaining information on the primary particle size, shape, and morphology of silica nanoparticles. The method employed is transmission electron microscopy (TEM), which uses an electron beam *in vacuo* to spatially resolve the physical structure of the silica nanoparticles. From the image collected, the size can be directly calculated for a sample of particles giving a number-average size and its relevant standard deviation. The shape of the particles can also be easily visualized from the TEM image. The general morphology can be seen as well under excellent imaging conditions. It is thus possible to directly visualize the pore structure of a mesoporous material using electron microscopy, which would otherwise be impossible using optical microscopy due to the diffraction limit. In the case of truly nanodimensional silica particles, electron microscopy is the method of choice for measuring size, shape and morphology.

3.2 Powder X-ray Diffraction

The silica nanoparticles commonly in use have an amorphous structure, so they do not have any features when probed by typical powder X-ray diffraction. However, in materials such as MCM-41, the pores are ordered enough to give rise to characteristic peaks in an X-ray diffraction pattern. Monochromatic X-ray radiation at 1.54 Å (Cu Kα line) is used to probe the structure of the material. The X-ray beam is focused onto the sample and the scattered (diffracted) beam is detected after the interaction occurs. Deflections occur in accordance to Bragg's Law, which is given by:

$$n\lambda = 2d \sin\theta \qquad (13)$$

Here in n is an integer, λ is the X-ray wavelength, d is the characteristic spacing between the lattice planes in the material, and θ is the scattering angle. The peaks, which appear at certain values of θ, can thus be indexed to certain crystal planes in the material.

3.3 Nitrogen Adsorption Isotherm

One of the characteristic properties of mesoporous silica nanoparticles is their inherently high surface area, typically on the order of 1000 m^2g^{-1}. Due to the structure of the material, almost the entirety of the surface area is contained within the porosity, i.e. almost none (<2%) is on the external surface of the particle. The pores also give rise to a characteristic pore volume and have a pore diameter, which strongly depends on the conditions under which the material was synthesized. All of these properties can be conveniently measured by using a gas adsorption isotherm. In this experiment, the sample is held at an isothermal point (typically 77 K, boiling point of $N_{2(l)}$) and a gas of interest (generally pure gaseous nitrogen) is added to the sample. The amount of adsorbed gas is carefully measured and this is plotted as a function of the saturation partial pressure ($x = P/P_0$). Based on whether a partial isotherm in a certain regime or a full isotherm is implemented, the surface area, pore volume, and pore diameter can be measured following fitting/calculations on the measured data. The surface area is measured by only using x = 0.05-0.35 where the adsorption isotherm is linear and fitted to the BET (Brunauer-Emmett-Teller) equation:

$$\frac{1}{v(x-1)} = \frac{C-1}{v_m C} * x + \frac{1}{v_m C} \quad (14)$$

$$C = e^{\Delta H_{ads} - \Delta H_{con}/RT} \quad (15)$$

In the BET equation, v is volume of adsorbed gas, C is the BET constant, x is the saturation partial pressure defined above, and v_m is the volume corresponding to single

monolayer of adsorbate on the material surface. The C constant depends on the absolute temperature, as well as the enthalpy change of the first adsorption layer (ΔH_{ads}) and the enthalpy change associated with the phase change from gas to liquid for subsequent layers (ΔH_{con}).[31]

The determination of the pore volume and diameter involve application of the BJH (Barrett-Joyner-Halenda) methodology. This requires a full isotherm across the range of the saturation partial pressure. The first branch of the isotherm is the adsorption branch, and then the adsorbed gas is removed by applying a vacuum. The total number of points is typically 50, 25 points each for adsorption and desorption. Either branch of the isotherm may theoretically be used in the calculation, but it is typical for mesoporous silica to use the desorption branch. The pore volume is calculated near unity for the pressure term (i.e. $P/P_0 \approx 1$). In this limit, it is assumed that the pores are all filled with liquid adsorbate. Then, the volume of adsorbed nitrogen (V_{ads}) gas can be used to calculate a liquid volume of nitrogen in the pores (V_{liq}):

$$V_{liq} = \frac{P_a V_{ads} V_m}{RT} \quad (16)$$

In this calculation, P_a is the actual gas pressure and V_m is the molar volume of the adsorbate, R and T are the usual gas constant and absolute temperature. In terms of the pore diameter, a distribution of sizes is calculated, for which the numerical average is reported to be the sample pore diameter. This calculation is employed using a modified form of the Kelvin equation and depends on the pore morphology. For cylindrical pores, such as in MCM-41 silica, the calculation is straightforward and can be given as:

$$r_K = \frac{-2\gamma V_M}{RTln(P/P_0)} \quad (17)$$

Here, r_K is the Kelvin radius of the pore, γ is the surface tension of the adsorbate at the temperature of the experiment, and the other parameters are described as above. In this analysis of the isotherm, the Kelvin radius is the radius of a pore before condensation of the gas to liquid takes place. Since a monolayer of nitrogen will already be adsorbed at this point, the Kelvin radius is less than the true pore radius. For nitrogen, the thickness of a statistical monolayer (t) is known to be 3.54 Å. This thickness is then added to give the true pore radius. Written in a different form, the desired quantity, the pore radius (r_p), can be given as:

$$r_p = r_K + t \quad (18)$$

In the BJH approach, stepwise desorption or adsorption is considered in regards to the effect on the pore thickness. By derivation, it is possible to generate a mathematical expression for the calculation of the pore diameter as originally described by Barrett, Joyner, and Halenda.[32] In its full mathematical form, the analytical expression is:

$$V_{pn} = \left(\frac{r_{pn}}{r_{Kn} + {}^{\Delta tn}/_{2}}\right)^2 \left(\Delta V_n - \Delta_{tn} \sum_{j=1}^{n-1} A_{Cj}\right) \quad (19)$$

Herein, A_c is the area exposed by the desorption step, Δt is the change in the statistical thickness due to the change in pressure, r_{pn} is the radius of the pore at step n, and V_{pn} is the volume of the pore filled at step n. This calculation is done at each step to give a pore size distribution.

3.4 Zeta (ζ) Potential Measurements

In solution, the surfaces of nanoparticles are not isolated and are modified by ions and molecules in solution. A way to probe this is by taking a zeta potential measurement. For example, in solution, silica nanoparticles typically have a very negative charge at the surface. This is due to the deprotonation of the surface silanols at all pHs above ~3.

Therefore, a total net negative charge is in place on the surface of the material. This is an unstable configuration, and so positively-charged ions such as sodium cations associate with the surface through electrostatic interactions. This forms a layer of sodium cations on the surface that is very static in that it does not easily exchange, known as the Stern layer. Then, a layer of cations and anions associates with this layer that can undergo change. The zeta potential is then measured at this outer layer, known as the diffuse layer. The experiment is carried out by applying a small potential across the sample, which is the particles dispersed in a conductive liquid. As charged entities migrate in an applied electric field, they will move in accordance with the surface charge. The particles are tracked during this by means of a laser. The scattered radiation from the particles is altered in phase by interaction with the particles and is strongly dependent on their velocity. The fluctuations in the phase are extracted to give the electrophoretic mobility. The electrophoretic mobility is directly related to the zeta potential (ζ) by:

$$\zeta = \frac{\eta \mu_E}{\varepsilon} \quad (20)$$

Here η is the sample viscosity and ε is the relative permittivity. Once the mobility is measured, it can then be directly used to calculate the zeta potential at the surface. The magnitude and sign of the zeta potential is directly related to the charge at the surface.

3.5 Thermogravimetric Analysis

Silica nanoparticles are commonly functionalized with an array of organic moieties for various applications. It is of general interest to understand how much of a given organic moiety is grafted onto the silica nanoparticle surface. To approximate this, thermogravimetry is used. In this experiment, the sample is heated, generally in a linear fashion up to a specified temperature. During the heating process, any organic

compounds become volatile at a characteristic temperature as they thermally degrade. Through the use of an extremely sensitive microbalance, mass changes are detected as a function of the temperature. A flow of inert gas such as nitrogen sweeps away molecules liberated from the surface during the heating process. The overall mass loss during the run can then be used to directly calculate the organic loading of the functional moiety.

3.6 Attenuated Total Reflectance-Fourier Transform Infrared Spectroscopy (ATR-FTIR)

Infrared spectroscopy is a commonly employed technique, which probes the fundamental vibration of molecules upon the interaction of light with matter. A general infrared spectrometer has a light source capable of generating broadband infrared radiation, which interacts with the sample. In the ATR configuration, the beam does not directly pass through the sample, but is instead directed to a solid-state element of an optically useful material such as germanium or zinc selenide (ZnSe) commonly referred to as the ATR crystal. The beam is directed into the crystal such that it exceeds the critical angle of the interface between the material and the air. The beam of radiation undergoes total internal reflection (TIR) and passes through the crystal and out the other side. When the beam reaches the interface it generates a decaying evanescent wave at the surface. This can be seen in Figure 3.1 below for the schematic of the experimental setup.

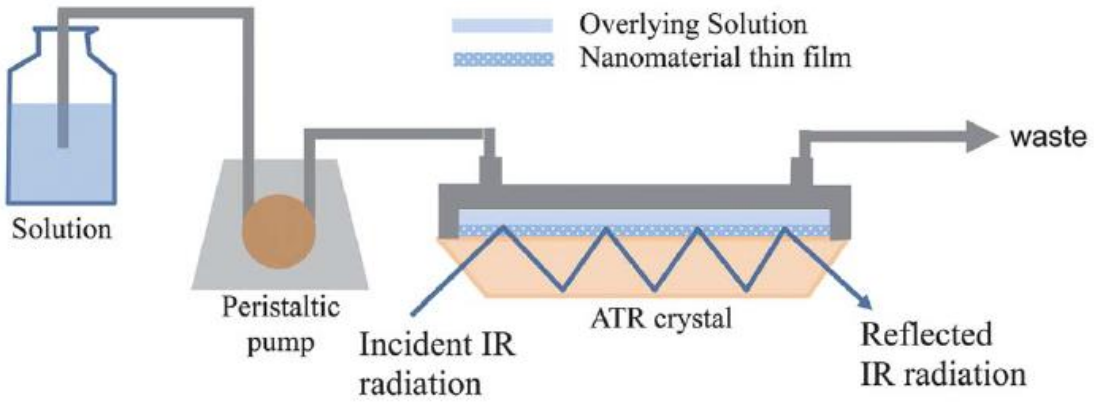

Figure 3.1 ATR-FTIR configuration for solution-phase adsorption measurements. Reproduced with permission from Reference 146. Copyright 2014, Royal Society of Chemistry.

This wave decays exponentially from the surface and so is able to probe short-range distances (~1 μm) from the interface of the crystal with any solution or material on the surface. Nanomaterials can be deposited onto the crystal in a thin film, and then solutions are flowed over the surface. Any spectral changes taking place over time can then be monitored to provide insight into processes such as adsorption that occur at the liquid-solid interface.

3.7 Solid-State NMR Spectroscopy

Modern NMR spectroscopy is typically used to study molecules dissolved in solution. Due to rapid molecule motion on the timescale of the NMR experiment, narrow linewidths are observed. In a solid sample, molecular motion is negligible. Therefore, attempting to obtain an NMR spectrum of a solid in a similar fashion to that employed for liquids results in a very broad spectrum with individual components that cannot be spectrally resolved. However, it is possible to remove a large amount, if not all, of the intrinsic anisotropy by spinning the sample at the magic angle (Magic Angle Spinning, MAS). The magic angle is found to be $\Theta_M = 54.74°$ with respect to the static magnetic

field. This angle is selected as it reduces the dipolar coupling Spin Hamiltonian term to zero, ex:

$$\mathcal{H}_D^{(1)} = -\frac{\mu_0 \gamma_P \gamma_S}{4\pi r_{IS}^3} \frac{(3\cos^2 \Theta - 1)}{2} \quad (21)$$

The sample is spun at a very high rotational rate, generally 10-50 kHz and a spectrum of the nucleus of interest is collected in a very similar fashion to that of solution-phase NMR. It is also possible to use the static nature of the solid to carry out a cross polarization (CP) experiment in which a more abundant nucleus (such as ^{1}H) is initially irradiated, and then the magnetization on this nucleus is transferred through a series of pulses to a less abundant nucleus (such as ^{13}C). By doing so, experimental time can be greatly reduced as the spectral intensity can be enhanced by up to several orders of magnitude.

CHAPTER 4
SOLUTION-PHASE CHARACTERIZATION OF FUNCTIONALIZED MESOPOROUS SILICA USING 1H NMR

4.1 Abstract

Mesoporous silica materials are undergoing rapid development for numerous environmental and biomedical applications. These materials are commonly functionalized with small organic molecules through a reaction between an organosiloxane and the surface silanols. Despite widespread use and implementation of these materials, ligands on their surfaces are challenging to characterize, particularly in aqueous environments. Employing traditional physicochemical characterization methods such as adsorption isotherms, X-ray diffraction, and electron microscopy; as well as solution-phase 1H NMR methods including 1D NMR, Diffusion Ordered Spectroscopy (DOSY) and 2D Nuclear Overhauser Effect Spectroscopy (NOESY), the labile nature of several different surface ligands on mesoporous silica nanoparticles is revealed. The data presented indicate a dynamic model of organosilane release from the surface, and adsorption of the released molecules is ultimately dependent on the nature of the binding of the functional group to the particle surface. A new paradigm for understanding chemical changes that take place at the liquid-solid interface is described, which incorporates a model of chemical dynamics in aqueous solution. Covalently-functionalized nanomaterials are widely used and the characterization of the ligands on their surfaces is of paramount importance, particularly when they are implemented in biomedical and environmental applications.

4.2 Introduction

Mesoporous silica is a porous amorphous silicate material with pores between 2-50 nm in diameter.[33] The structure consists of amorphous silica condensed around pore-voids, in which the silicon atoms are surrounded by tetrahedrally-bonded oxygen atoms.[1] Mesoporous silica nanoparticles (MSNs) have a sub-100 nm particle size and are undergoing rapid development for applications such as drug delivery, contaminant remediation, and heterogeneous catalysis, among others.[34-37] These materials benefit from unique and advantageous physicochemical properties such as extremely high surface areas (~1000 m^2/g), tunable surface chemistries, and low observed toxicity.[38-40] Overall this has led to great advances of these materials, especially for biomedical applications such as drug delivery.[41-43]

Despite these many advantageous properties, there are some drawbacks including inherent particle heterogeneity resulting from the nature of the synthetic process.[44] Due to the difficulties associated with synthetic variability, extensive batch-wise characterization is required to verify the chemical composition and specific properties. Confirmation of the surface functionalization is typically achieved using FTIR spectroscopy. While this will show characteristic group frequencies of the functional group, it does not generally reveal the chemical nature of the interaction with the surface. Thermogravimetric analysis is the quantitative method of choice when ascertaining how much functional group has been loaded onto the particle surface by measuring mass loss as the sample is heated in a stream of air or nitrogen. Yet this method is only suggestive, unless coupled with a spectroscopic technique such as FTIR spectroscopy to determine what is being released from the surface during the heating process.

Another method for characterizing functionalized MSNs is solid-state NMR, which is commonly used to investigate nanomaterials and functionalized nanomaterials in particular. Application of solid-state NMR involves implementing cross polarization magic angle spinning (CP-MAS) and/or high resolution magic angle spinning (HR-MAS) experiments. ^{29}Si NMR can reveal the local electronic environment and thus the local structure of the silicon tetrahedra, and using ^{13}C CP-MAS NMR, spectra of the nanomaterial-bonded functional groups can be obtained.[45] By implementing solid-state NMR methods it is possible to obtain narrow lineshapes that can approach the resolution of solution-phase spectra.[46-48] These methods enable chemical characterization of the framework material and any ligands bonded to the surface. However, an important caveat with these methods is that they are generally carried out on the dried powders. This is useful in some respects but when considering the desired applications, i.e. drug delivery and environmental remediation, molecular-level information for these materials in an aqueous environment is needed. Recent work has probed the structure of functionalized nanomaterials using solid-state NMR enhanced by dynamic nuclear polarization (DNP), revealing unique insight into the structure of surface-condensed organosiloxanes.[49] However, it is important to consider that complex chemical changes can occur in aqueous environments that do not occur in a dried state.[50] This is why solution-phase characterization methods are critical to understanding structural and dynamic characteristics of functionalized nanomaterials.

Solution NMR methods are utilized in a wide variety of applications, and have recently been applied to colloidal nanomaterials to probe both the structure and dynamics of these materials in solution.[51-52] These methods are attractive due to the ability to

provide molecular-level information about systems that are intrinsically complex. Solution NMR methods can be used to characterize and quantify ligand binding and release, ligand exchange, and structural motifs in bound ligands.[53-54] In this report, we describe the application of a solution-phase NMR toolbox, as first described by Hens and Martins, to the characterization of MSNs functionalized with small organic groups of different types.[55] Generally, these organic functional groups have been viewed as covalently bound and so have been assumed to be effectively static on the nanoparticle surface.[56] Employing advanced methods, such as diffusion ordered spectroscopy (DOSY) and nuclear Overhauser effect spectroscopy (NOESY) as part of an NMR toolbox approach; we provide new insight into the nature of these ligands. Results are indicative of complex, labile ligand systems capable of dynamic chemical change, dependent on the nature of the ligand and its intrinsic siloxane bond-forming moieties. The data gives rise to a new model for understanding binding and release of supramolecular-bound ligands in an aqueous environment, and suggests the possibility of full chemical release from the surface. In some cases, these ligands can adsorb onto the surface in a complex chemical binding event, giving rise to possible free-solution kinetic binding events in a likely chemical exchange regime.

4.3 Experimental Methods

4.3.1 Silica Nanoparticle Synthesis and Functionalization

Mesoporous silica nanoparticles of MCM-41 and WO morphology utilized for the experiments in this Chapter were synthesized using methods described in Chapter 2 above, Sections 2.1 and 2.2, respectively. Functionalization with APTES and CES functional groups was carried out using the procedure described in Chapter 2, Sections 2.4.1 and 2.4.2, respectively.

4.3.2 Sample Preparation

Samples were prepared for solution ^{1}H NMR experiments by dispersing approximately 10 mg of MSNs in 600 μL of D_2O via sonication for 30 min. Sample pH was adjusted using HCl or NaOH in D_2O and corrected using a known isotopic correction calculation.[57] The pH was measured before and after the NMR experiment using a Corning 320 pH meter and the average of the two values was taken as the pH for the experiment. Generally the pH reading obtained before and after each NMR experiment differed by <0.1 pH units. The samples were sonicated for approximately 30 minutes immediately before the NMR measurements.

4.3.3 Solution NMR Experimental Setup

One-dimensional (1D) NMR experiments were conducted on either a Bruker DRX-400 or a Bruker Avance III spectrometer operating at 400 MHz; all DOSY experiments were conducted on the Bruker Avance III 400 MHz spectrometer. Two-dimensional (2D) NOESY experiments were conducted on a Bruker Avance 500 MHz instrument. All ^{1}H chemical shifts were referenced to the residual solvent proton signal (for HDO this is a broad singlet peak centered at 4.69 ppm). All one-dimensional ^{1}H NMR experiments were performed using a single-pulse sequence (Bruker zg pulse sequence). Pulse widths were optimized as necessary. The relevant experimental parameters were as follows: TD = 64k, NS= 16-128, and D1=1-10s. TD, NS and D1 refer to the time-domain data points, number of scans, and relaxation delay, respectively. The data were processed using Topspin 2.1 software with a 64k zero-filling and a 0.3 Hz exponential line broadening parameter. Quantitative measurements were carried out using an appropriately selected internal standard (acetone, acetonitrile) added at a similar

concentration to the species of interest. The longitudinal relaxation (T_1) for the molecules of interest were determined using the inversion recovery method (t1ir1d or t1ir pulse sequences) and the relaxation delay was set to be $5*T_1$ of the slowest relaxing group of protons. Following processing steps including phasing and baseline correction, peaks of interest were integrated to enable quantitative calculations.

4.3.4 Diffusion Ordered Spectroscopy (DOSY) Parameters

DOSY experiments were conducted using an automatic tuning and matching BBFO probe equipped with a z-gradient coil. Samples were thermally equilibrated at 25 °C for 15 min before data collection. All diffusion measurements were made using the stimulated echo pulse sequence with bipolar gradient pulses (stebpgp1s pulse sequence). The diffusion delay (Δ) varied from 20 to 40 ms, and the gradient pulse duration (δ) from 1.5 to 5 ms and were optimized in order to obtain 1-5% residual signal at 95% of the maximum gradient strength. The recycle delay varied between 5-10 s. Rectangular shapes were used for the gradients and a linear gradient ramp with 16 increments between 2% and 95% was applied. The gradient strength (56.0 Gauss/cm at a current of 10 A) was calibrated by measuring the self-diffusion of the residual HDO signal in a pure D_2O (99.98 % D) sample at 298K (1.90×10^{-9} m^2/s). Diffusion coefficients were calculated by integrating the peaks of interest and direct curve-fitting to the Stejskal–Tanner equation:

$$I = I_0 * \exp[-\gamma^2 G^2 \delta^2 \left(\Delta - \frac{\delta}{3}\right) D] \quad (22)$$

where I, I_0, γ, and G are the observed intensity, signal intensity in the absence of the gradient, the proton magnetogyric ratio and the gradient strength, respectively. The T_1/T_2 analysis program in Topspin 2.1 was used to carry out the processing and curve-fitting for all peaks/nuclei.

4.3.5 Nuclear Overhauser Effect Spectroscopy (NOESY) Parameters

2D nuclear Overhauser effect spectroscopy (NOESY) experiments were performed on a Bruker Avance 500 spectrometer that was equipped with a 5 mm BBFO z-gradient probe (noesyph pulse sequence). The experimental parameters are as follows: SW2 = SW1~3500 Hz, TD2 = 2048, TD1 = 150, NS = 16, DS = 32, D1 = 4s. SW1 and SW2 refer to spectral widths in the first and second dimension, respectively; DS refers to the number of dummy scans. ^{1}H spectral widths and $\pi/2$ pulse widths were optimized for each sample. The range of mixing times used was estimated by using the one-dimensional version of the inversion recovery pulse sequence (t1ir1d). Samples were prepared in D_2O in a manner similar to the 1D experiments. 2D NOESY spectra were collected using a ^{1}H spectral width of 7.00 ppm. Typically 150 t_1 increments, consisting of 16 scans of 2048 sampled data points each, were recorded with a 4 s relaxation delay. ^{1}H spectral widths and 90^o pulse widths are optimized for each sample. A recycle delay (d1) of 4.0 s was used in all the 2D experiments. A range of mixing times for NOESY experiments was determined using an approximated T_1 (spin-lattice) relaxation time. Mixing times of 200, 500, 1000, 1200 and 1500 ms were utilized. All NMR data were processed with TOPSPIN 1.3 or 2.1 programs. The 2D NMR data were processed with zero-filling to 2,048 points and 1,024 points in t_2 and t_1 dimensions, respectively. The on-diagonal peaks were phased to be negative, following standard conventions for small organic molecules.

4.4 Results and Discussion

4.4.1 Material Images and Characterization

The silica nanoparticles were analyzed using transmission electron microscopy imaging to determine the size and morphology of the silica nanoparticles. The images of the materials and size histograms are shown below (Figures 4.1-4.4).

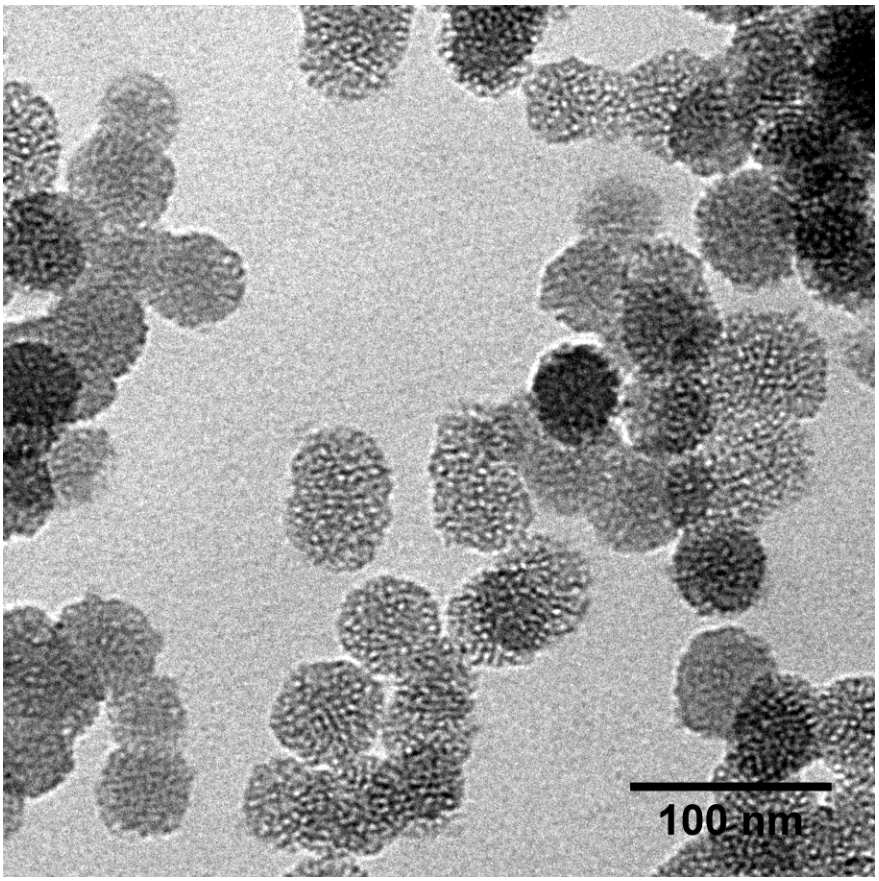

Figure 4.1 TEM image of wormhole-type (WO) mesoporous silica used in this study and functionalized with APDMMS or APTES.

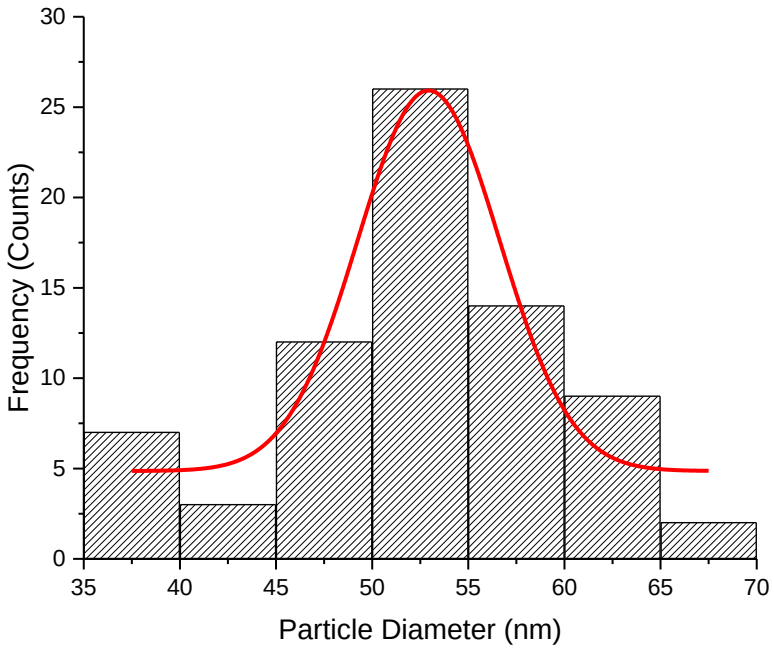

Figure 4.2 Histogram for WO mesoporous silica with a Gaussian fit. The particle diameter is 53 ± 7 nm based on the Gaussian fit to the data.

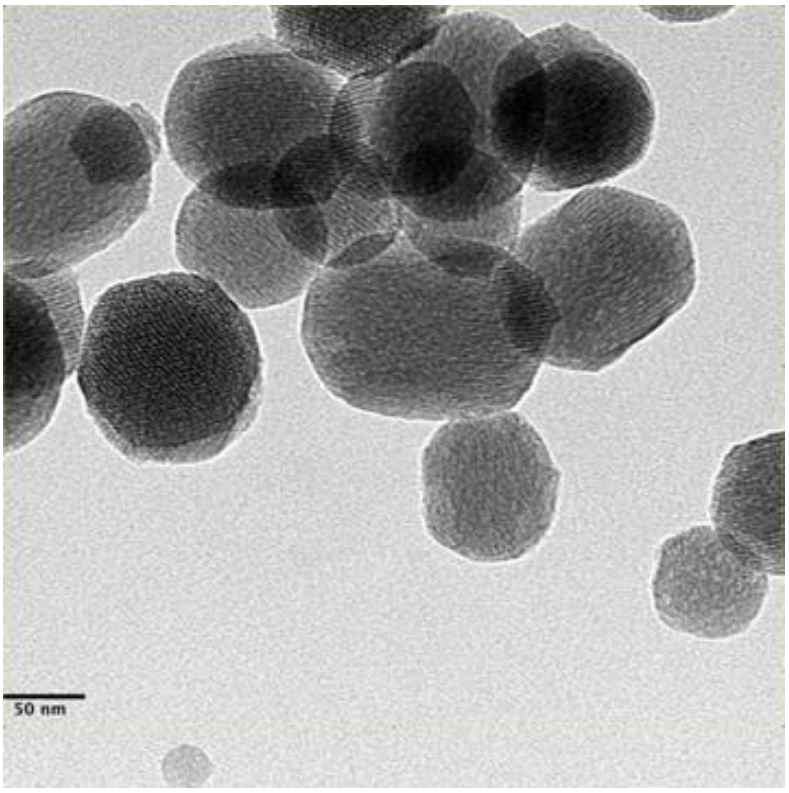

Figure 4.3 TEM image of MCM-41 type mesoporous silica that was subsequently functionalized with CES.

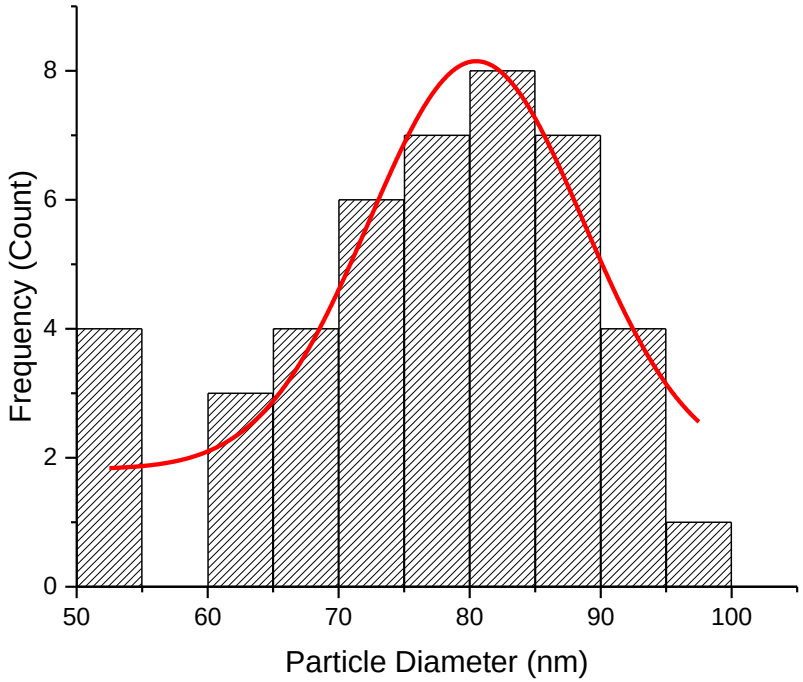

Figure 4.4 Histogram for MCM-41 mesoporous silica with a Gaussian fit. The particle diameter is 80 ± 16 nm based on the Gaussian fit.

All materials were characterized using nitrogen adsorption-desorption isotherms. The surface area was calculated using the Brunauer-Emmett-Teller (BET) methodology using a seven-point isotherm. The pore diameter and pore volume were calculated using the Barrett-Joyner-Halenda (BJH) methodology using the desorption branch of a 50 point adsorption-desorption isotherm. The samples were characterized both pre- and post-functionalization of the silica nanoparticles (Table 4.1). This data shows characteristic decreases in the surface area and pore volume upon the functionalization of the material. The pore diameter, as measured, does not appear to change. It is hypothesized that the reason this does not change is due to the fact that the average pore diameter is reported from the calculation. Therefore, even though the distribution is probably broader, the average value remains relatively unchanged.

Table 0.1 Nitrogen Adsorption-Desorption Isotherm Data.

Sample	Pre/Post Functionalization	Surface Area (m^2/g)	Pore Volume (cm^3/g)	Pore Diameter (nm)
MSN@APDMMS	Pre	1090 (± 44)	0.47 (± 0.03)	3.160 (± 0.007)
MSN@APDMMS	Post	440 (± 18)	0.29 (± 0.02)	3.100 (± 0.006)
MSN@APTES	Pre	1090 (± 44)	0.47 (± 0.03)	3.160 (± 0.007)
MSN@APTES	Post	260 (± 10)	0.30 (± 0.02)	8.39 (± 0.02)
MSN@CES	Pre	1260 (± 51)	0.70 (± 0.04)	3.070 (± 0.007)

It is also common to employ X-ray diffraction to measure the structure of the pores inside the material. The silica itself is amorphous and therefore is not related to the observed X-ray diffraction patterns in the material (Figures 4.5 and 4.6). The pore-voids themselves, however, do give rise to characteristic diffraction peaks around $2\Theta = 2.2$ as the main peak of interest in mesoporous silica. The WO-type material does not show this ordering as it is an intrinsically less ordered material due to the random organization of the pores inside the silica.

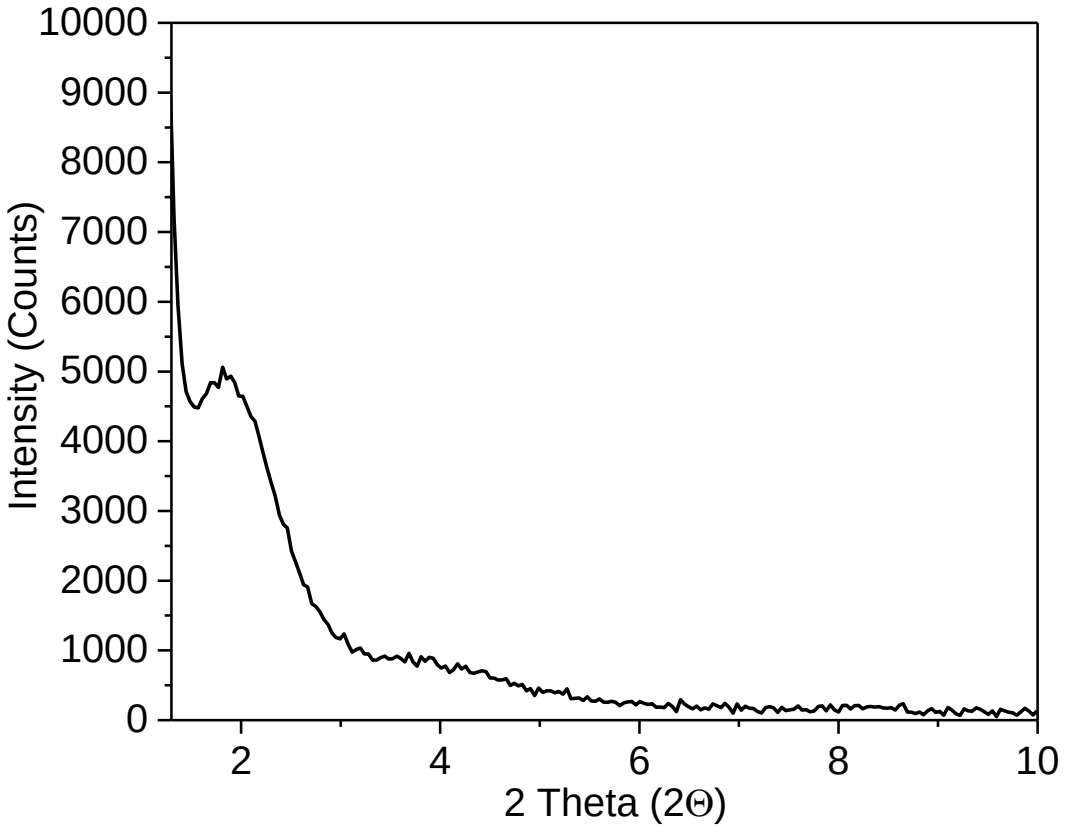

Figure 4.5 Diffraction pattern for WO type silica used in this study. Due to the non-ordered nature of the pores within the material, only the greatly broadened diffraction peak centered around 2Θ = 2.2 can be seen. This is consistent for this type of less-ordered mesoporous silica.

Depending on the type of silica, other peaks such as those around 4.4 and 5.5 2Θ for the MCM-41 type material. The diffraction peaks observed at 2.2, 4.4, and 5.2 2Θ can be indexed to the (100), (110), and (200) crystal planes, respectively.

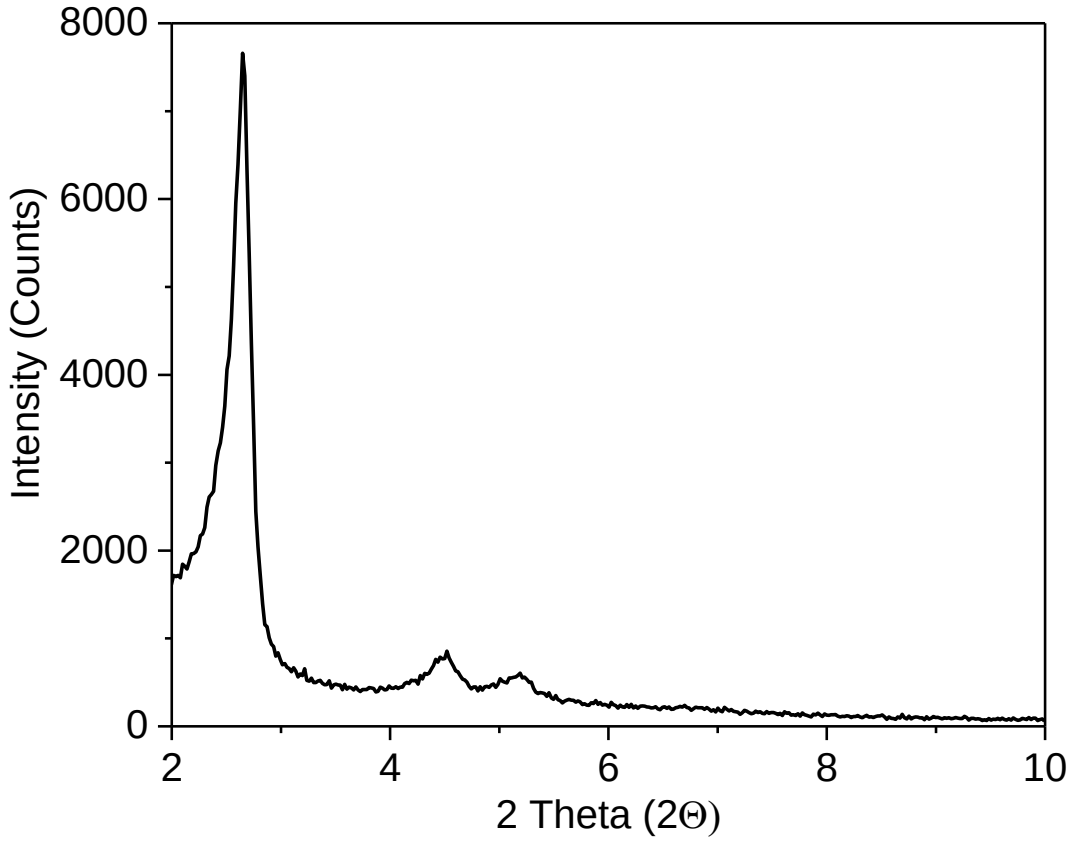

Figure 4.6 Diffraction pattern for MCM-41 type silica used in this study.

4.4.2 Solution-Phase 1D ^{1}H NMR

Signals of the mesoporous solid nanoparticles functionalized with APDMMS, APTES or CES were detected using 1D solution-phase proton NMR. ^{1}H NMR spectra and associated molecular structures are shown in Figures 4.7 and 4.8. In particular, it is important to note the loss of the methoxy group (for APDMMS) and the loss of up to three ethoxy groups, for APTES and CES, during the coupling of the molecules to the surface.

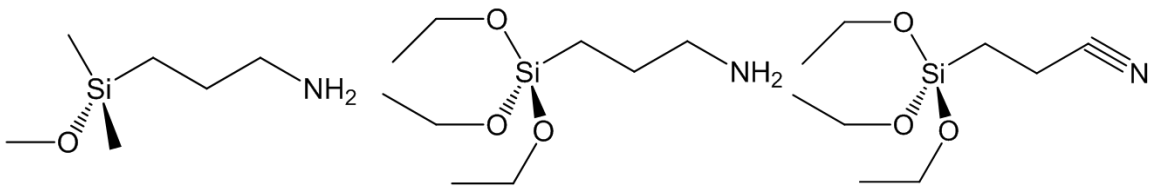

APDMMS APTES CETS

Figure 4.7 Organosilicon molecules used in surface functionalization. These are the structures of the free molecules prior to bonding to the surface. L to R: aminopropyldimethylmethoxysilane (APDMMS), aminopropyltriethoxysilane (APTES), (2-cyanoethyl)-triethoxysilane) (CETS).

An additional aspect to consider is how the nitrile is converted to the free carboxylic acid for the putative CES molecule via hydrolysis. Two equivalents of water are required to hydrolyze the nitrile to the CES molecule, which proceeds through an amide intermediate. All peaks have been assigned and correlated with the structures of the functional group molecules.

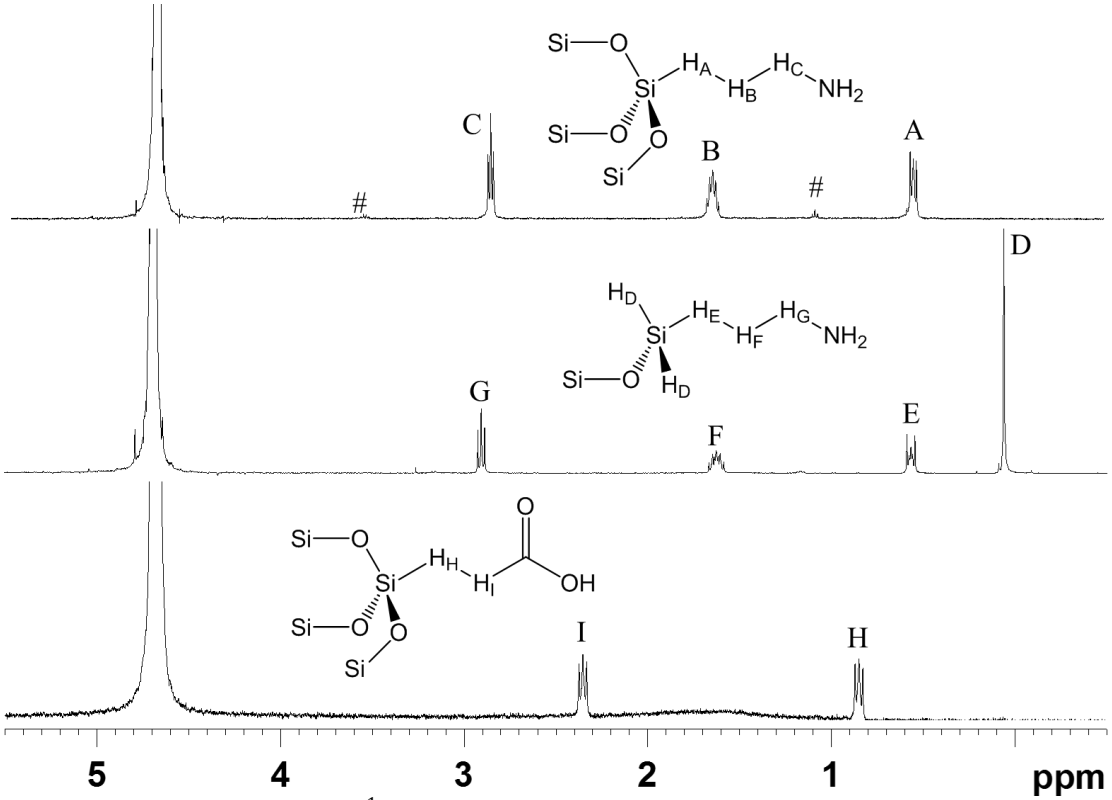

Figure 4.8 Solution-phase 1D ^{1}H NMR spectra of functionalized MSNs, with functional group structures included and peaks assigned. Putative surface silicon atoms are shown in the structures. Samples are MSNs functionalized with: WO@APTES (Top), WO@APDMMS (Middle) and MCM-41@CES (Lower). The samples were at pH values of: 11.6 (APDMMS), 4.3 (CES), and 10.6 (APTES). Residual ethoxy group (-OCH_2CH_3) protons in the APTES sample are denoted by (#). [APTES and APDMMS data from Y. Tataurova.]

Proton NMR spectra of the free molecules were also collected to serve as a reference (not shown). Note the residual signals of the ethoxy group protons at ~1.0 and ~3.6 ppm for the APTES-functionalized sample. These peaks were not observed in the CES sample due to the vigorous hydrolysis procedure used to prepare it from the nitrile. The APTES sample did not undergo a hydrolytic procedure, so it is plausible that some of the ethoxy groups remain on the molecule bound to the surface. In the CES sample, a broad peak centered at 1.6 ppm can be seen. This is most likely due to surface silanol (Si-OH) protons on the nanoparticle surface, which are exchanging with protons in the bulk solvent.

4.4.3 Diffusion Measurements

Diffusion ordered spectroscopy (DOSY) is a pseudo-2D experiment, which is an application of the pulsed field gradient (PFG) experiment. DOSY has previously been used for characterizing ligands bound to functionalized nanocrystals and has also been used to characterize alkylammonium-silica mixtures to provide insights into zeolite crystallization.[55,58-62] In order to apply this methodology, the functionalized materials were suspended in solvent and then the experiment is carried out. Initially the diffusion time (Δ) and pulsed gradient length (δ) must be optimized by initial 1D experiment. Then the 2D experiment is carried out with the optimized parameters, as the gradient strength is systematically incremented. The peaks of interest are integrated and the intensity is plotted as a function of the gradient strength. The data is directly fitted to the Tanner-Stejskal equation to extract the molecular diffusion coefficient for each peak. The individual values are averaged to give an average value for the molecule. An example data set and its fit are shown below in Figure 4.9 for the MCM-41@CES system. In this case, the fit is excellent, showing that the calculated diffusion coefficients are accurate for the molecular systems studied herein.

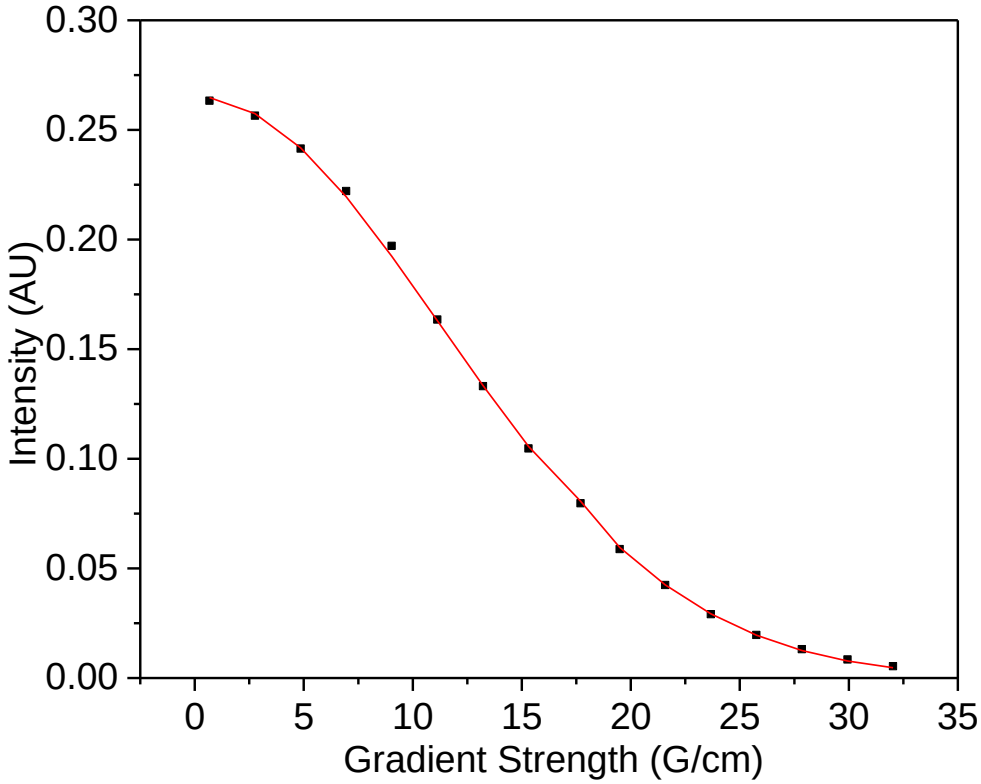

Figure 4.9 DOSY data for the peak at ~0.85 ppm in the MCM-41@CES molecule; the methylene protons located nearest to the central silicon. The experimental integrated intensity for the peak is shown as a function of the gradient strength. The red line represents the calculated curve fit based on direct fitting to the Tanner-Stejskal equation.

Table 4.2 lists the measured diffusion coefficients for each of the three samples given as the molecular diffusion coefficient averaged from the individual peaks across the entire molecule. Diffusion coefficients of the free molecules were also obtained and are reported as well. As a means of comparison, the self-diffusion coefficient for water (HDO) is reported. Note the smaller diffusion coefficients for the free molecules (APTES/CES) relative to the bound, indicative of possible dimerization in solution.

Table 0.2 Molecular Translational Diffusion Coefficients from DOSY NMR, in m^2/s.

Sample	Average (± SD)	Water	Sample	Average (± SD)	Water
APDMMS	6.25 (± 0.01) x 10^{-10}	2.06 x 10^{-9}	CES	2.05 (± 0.02) x 10^{-10}	1.16 x 10^{-9}
MSN@ APDMMS	6.5 (± 0.2) x 10^{-10}	2.10 x 10^{-9}	MSN @CES	6.39 (± 0.04) x 10^{-10}	2.05 x 10^{-9}
APTES	3.04 (± 0.06) x 10^{-10}	1.78 x 10^{-9}	MSN@CES + Free CES	5.22 (± 0.02) x 10^{-10}	2.04 x 10^{-9}
MSN@ APTES	6 (± 1) x 10^{-10}	2.11 x 10^{-9}			

Evaluating the calculated diffusion coefficients by using the Stokes-Einstein relation (Eq. 23), a hydrodynamic diameter can be approximated. In many cases, the hydrodynamic diameter is much more desirable than a physical size as it takes into account the interaction of the solvent with the particle or molecule. Engineered nanomaterials such as mesoporous silica nanoparticles are most likely to be found in an aqueous environment rather than in a dried state. In Eq. 23 d_H is the hydrodynamic diameter, k_B is Boltzmann's constant, T is absolute temperature, η is sample viscosity, and D is the molecular translational diffusion coefficient given in m^2/s.

$$d_H = \frac{k_B T}{3\pi\eta D} \quad (23)$$

For these measurements, the viscosity of the nanoparticle dispersion was determined using an Ostwald viscometer with pure H_2O as the reference. The determined viscosity was used to calculate the hydrodynamic diameters. Calculation of the hydrodynamic diameter from the diffusion coefficients yields values of 0.54 (APDMMS), 0.59

(APTES), and 0.55 (CES) nm. These values correlate well with small organic molecules and demonstrate the inverse relationship between diffusion coefficient and hydrodynamic diameter. If these functional groups were bound to the surface, they would then be forced to diffuse along with the particle. Theory predicts, then, that the diffusion coefficients of the protons in the functional groups bound to the MSN surface would be roughly 7.7 x 10^{-12} m^2/s. This calculation is based on approximating the hydrodynamic diameter of these materials as 50 nm, using 25 °C as the absolute temperature and using the nanoparticle dispersion viscosity as measured at 25 °C.

These results indicate that either the ligand molecules have come off the surface, or that the observed diffusion coefficients are the weighted average of the free and bound ligands under a fast exchange regime, and a large proportion of the detected molecules are in the "free" form. A 2D plot of the DOSY data (^{1}H chemical shift vs. log[diffusion coefficient]) for the APDDMS functionalized material is shown in Figure 4.10.

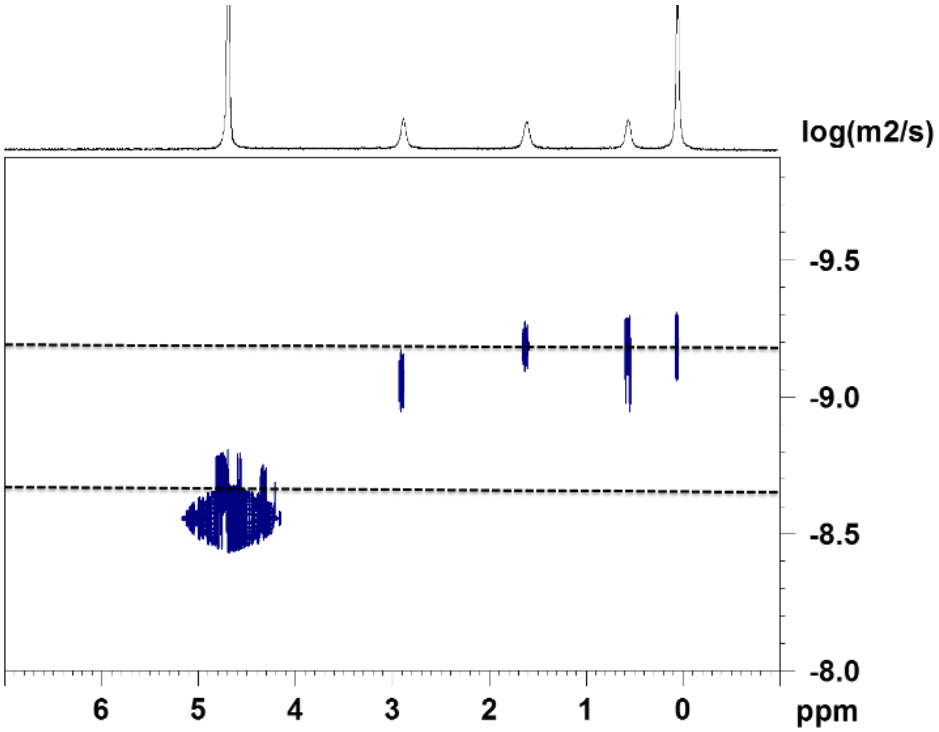

Figure 4.10 2D DOSY plot of APDDMS functionalized mesoporous silica. The residual water peak can be seen at around 4.7 ppm while the four signals corresponding to APDDMS can be seen further upfield in the spectrum. Dashed lines indicate the averaged molecular diffusion coefficient for ADPMMS and the diffusion coefficient for water, respectively, as reported in Table 4.2. The ordinate is the logarithm, base ten of the diffusion coefficient.

This type of processing of the data has the potential to identify hidden molecular components under favorable solution conditions. As can be seen, only one set of diffusion coefficients is observed which corresponds to the free molecule. Similar results were also observed for the other two systems supporting similar conclusions.

In the case of chemical exchange occurring during DOSY measurements, the diffusion delay (Δ) can be used to place a lower limit on desorption of molecular species. Work by Hassinen et al. reveals that for a bimolecular exchange system, the lower limit is the inverse of the diffusion delay.[63] Using the smallest diffusion delay utilized in these experiments, a desorption constant of at least 50 s^{-1} can be estimated. The desorption rate probably exceeds this limit by a large margin due to the small nature of the ligand and the

free accessibility of silanol moieties and/or exchange sites on the surface of the nanoparticles, for the APDMMS system.

4.4.4 Nuclear Overhauser Effect Spectroscopy

2D NOESY NMR utilizes the nuclear Overhauser effect, which is a through-space correlation, as opposed to the through-bond correlations like that in J-coupling. The nuclear Overhauser effect (NOE) occurs between protons that exhibit dipolar coupling and in a classic small-molecule regime the NOE intensity is governed by the internuclear distance (~$1/r^6$). The sign of the NOE depends on the rotational correlation time τ_c, which for a rigid spherical molecule is given by:

$$\tau_c = \frac{4\pi\eta r^3}{3k_B T} \quad (24)$$

Here r is the molecular radius and the other parameters are identical to those in Equation 23. If $\tau_c\omega_0 << 1$, where ω_0 is the NMR spectrometer frequency, the sample is in the extreme narrowing region and exhibits small molecule behavior and weak positive NOEs. If $\tau_c\omega_0 >> 1$, then the sample is in the spin-diffusion limit and strong negative NOEs are observed. For the spectrometer used in these experiments, ω_0 is 500 MHz. Calculating the rotational correlation times for both the spherical nanoparticles and the free small molecules gives values of around 200 μs and 410 ps, respectively. For molecules bound to the nanoparticle surface, $\tau_c\omega_0$ is ~10^5 whereas for free small organic molecules it is ~0.2. This indicates that a small positive NOE is expected for free molecules and a large negative NOE is expected for bound molecules. This is relative to the diagonal peaks in the NOESY spectrum, following conventions, such that cross peaks with the same sign are observed with a negative NOE and for a positive NOE, cross peaks have the opposite sign, relative to the peaks along the diagonal.[55]

In order to understand further the structure of the functional groups on the nanoparticle surface, 2D NOESY spectra were collected for MSN@APDMMS, MSN@APTES, and MSN@CES (Figures 4.11-4.13). These spectra are phase-corrected such that the diagonal peaks are negative (red). MSN@APDMMS showed NOE cross peaks with the same sign as the diagonal, whereas MSN@APTES and MSN@CES revealed NOE cross peaks with opposite signs with respect to the diagonal.

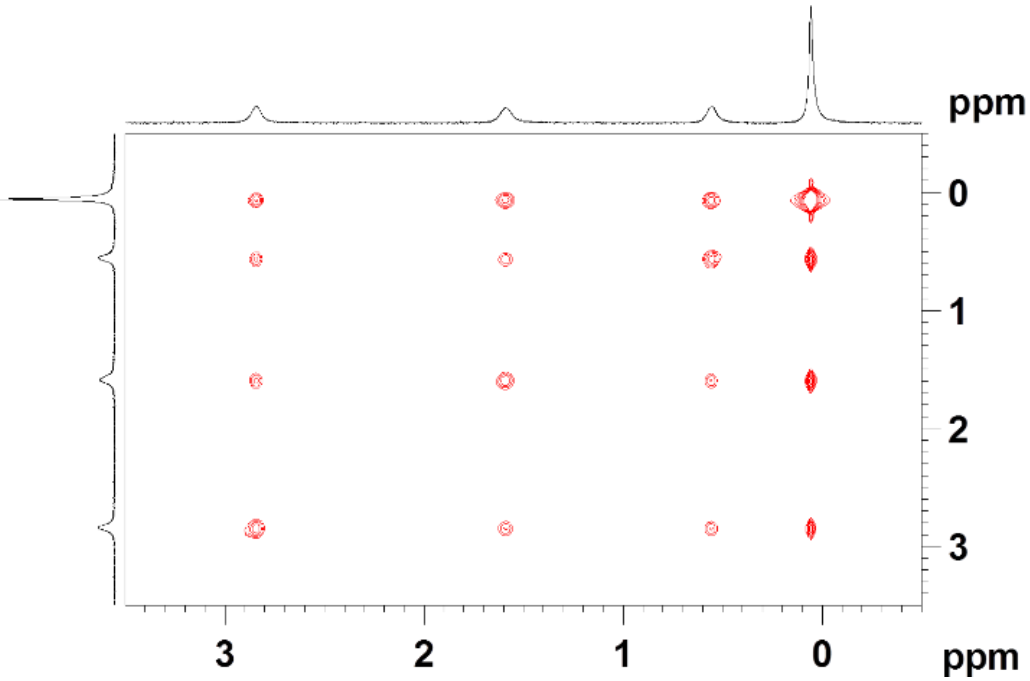

Figure 4.11 2D NOESY spectrum of APDMMS functionalized mesoporous silica (τ_{mix} = 0.2 s). All peaks in this spectrum have the same sign (negative), indicating APDMMS molecules bound to the surface. Sample pH = 11.6. [Data from Y. Tautarova.]

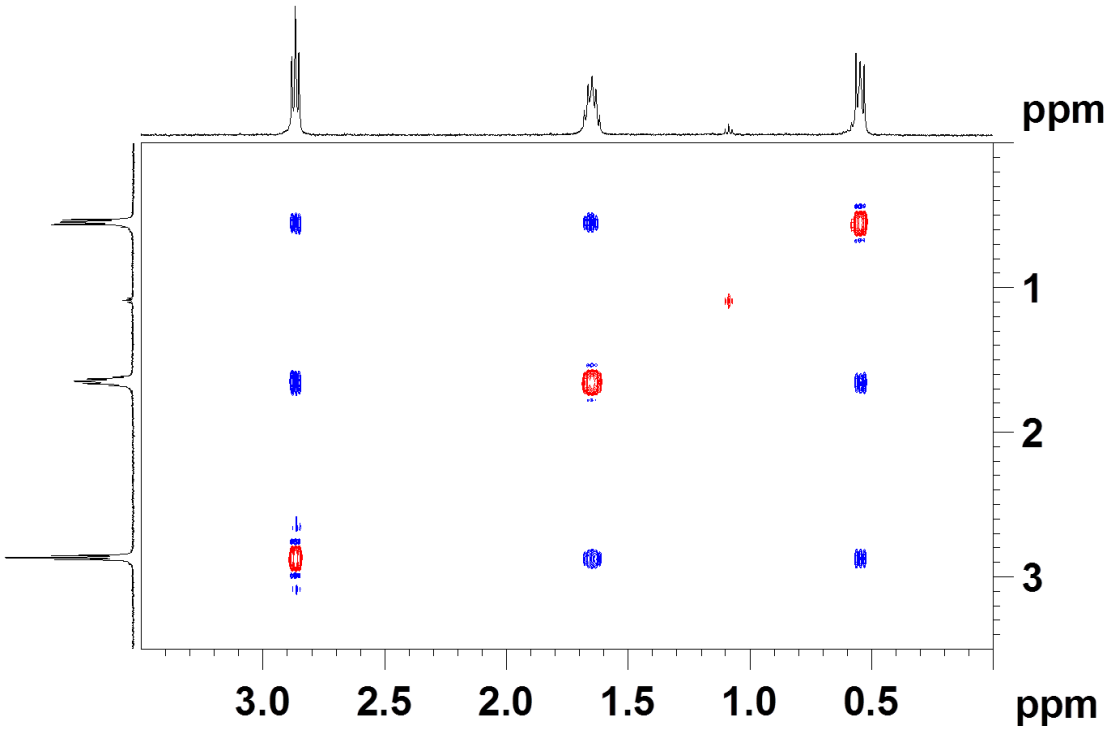

Figure 4.12 2D NOESY spectrum of APTES functionalized mesoporous silica (τ_{mix} = 1.5 s). The cross peaks observed in the spectrum have the opposite sign (positive), indicating presence of the free molecule. Sample pH = 10.6. [Data from Y. Tautarova.]

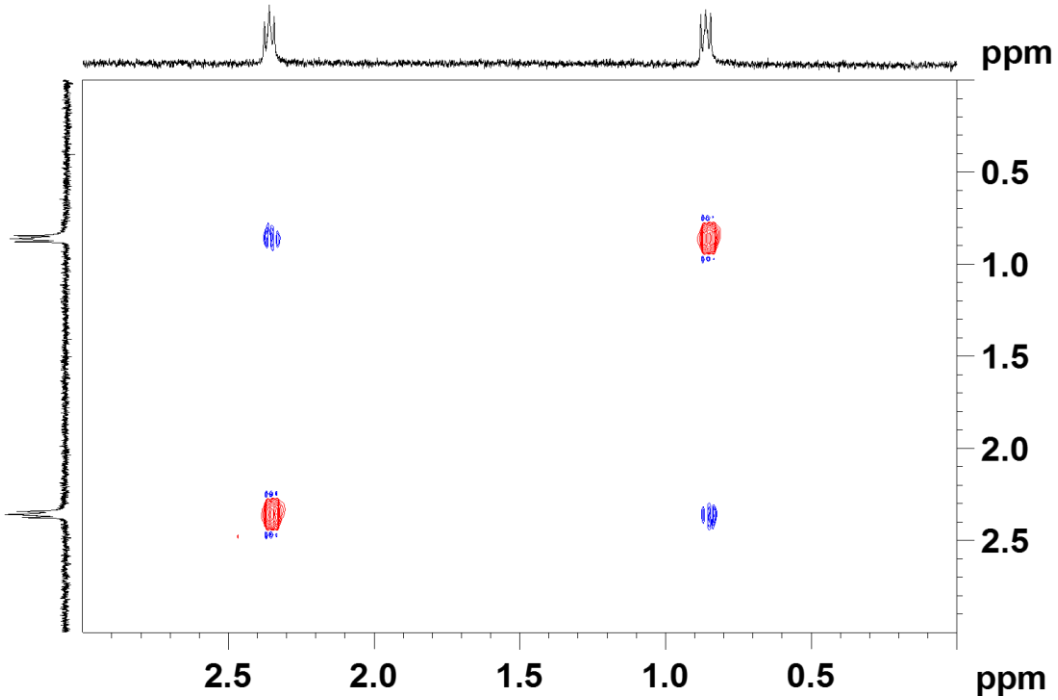

Figure 4.13 2D NOESY spectrum of CES functionalized mesoporous silica (τ_{mix} = 1.2 s). The two peaks observed from the methylene protons have the opposite sign (positive) as the diagonal, indicating free molecules detected in solution. Sample pH = 4.3.

Additionally, MSN@APTES and MSN@CES showed very weak or no NOEs at mixing times up to 1.5 s, whereas MSN@APDMMS showed very strong NOEs-even at a short mixing time of 0.2 s. In accordance with NOE theory and standard display conventions, the NOE cross peaks of small molecules in the extreme narrowing limit ($\tau_c\omega_0<<1$) are expected to be in opposite sign to the diagonal peaks, whereas large molecules in the spin-diffusion limit ($\tau_c\omega_0<<1$) show NOE cross peaks of the same sign with respect to the diagonal peaks.[64-65]

The NOE characteristics of a small molecule tightly bound to a large macromolecule irrespective of the nature of binding (covalent or non-covalent) are similar to that of large molecules, since the effective isotropic tumbling correlation time of the small molecule is the same as that of large molecules. NMR is frequently used to probe the structure and dynamics of very large molecules such as protein-protein

complexes. Even for these large macromolecular complexes, NOESY signals can be seen.[66] It can be inferred from these kinds of studies that even though functionalized nanoparticles are large compared to protein-protein complexes, the inherent mobility of surface-bound ligands can give a rationale for expecting NOESY results that, when evaluated carefully, show spin-diffusion like characteristics for large molecules.

The observation of strong NOEs with the same sign as the diagonal peaks for MSN@APDMMS is clearly consistent with a strong binding of APDMMS to the nanoparticle surface. In addition, chemical exchange between free and bound forms contributing to the NOE cannot be ruled out, as NOESY cannot distinguish between dipolar and chemical exchange mechanisms. Chemical exchange is the most likely cause for the observed NOESY results. Furthermore, the observation of medium NOEs at longer mixing times for MSN@CES and MSN@APTES with the opposite sign relative to the diagonal peaks suggests that CES and APTES may be detached from the MSN framework and tumble freely in solution or bind very weakly with the equilibrium heavily shifted toward the "free" state.

Though it appears that the NOESY and diffusion data are contradictory, they do both support the binding of organic functionalities on the nanoparticles and an exchange between their free and bound forms. The difference primarily arises in defining the extent to which the binding occurs. For the APDMMS system, the NOESY data suggests strong binding and an equilibrium highly shifted to favor the bound state. The diffusion coefficients of MSN@APDMMS and APDMMS, on the other hand, are almost the same and within the experimental error, suggesting a free state for APDMMS in MSN@APDMMS. For the APTES system, an increase in diffusion coefficient is

observed for MSN@APTES, the opposite of what is expected assuming a much larger hydrodynamic radius. This is possible, if APTES is in a polymeric form when it is free, and in the presence of MSN (MSN@APTES), APTES is almost in the "free" state, but in a monomeric form. The NOESY data is also consistent with this interpretation, since NOEs support an extreme narrowing condition for MSN@APTES. For the CES system, the diffusion coefficients of CES and MSN@CES imply that the free molecule is a larger chemical species. This is consistent with possible dimerization of the molecules, which is well-noted in the literature to occur with carboxylic acids.[67-68]

Similar results have also been reported previously in the literature. Work done by Hassinen et al. on CdSe quantum dots (QDs) in which octylamine ligands bound to the surface revealed somewhat similar results.[63] The octylamine ligands appeared to be bound based on the NOESY results, yet the DOSY data gave a larger diffusion coefficient than would be expected for fully bound molecules. This is similar to the results presented here, except that in our case the molecules seem to exhibit either pure or close-to-pure free behavior for all three cases based on the diffusion data. Other work by Gomes et al. on a similar CdSe QD system revealed complete displacement of oleic acid ligands by alkylphosphonic acids.[69] These chemical systems are quite different from the systems studied here, as the reported results herein seem highly indicative of complex chemical equilibria between the free and bound states of organosilane moieties as a result of physisorption, chemisorption, or some combination of both.

4.4.5 Ligand Quantitation and Comparison

In order to further characterize these chemical systems quantitative NMR (qNMR) was used to determine quantitatively the amount of ligands observed in solution.

The results of the qNMR experiments were then compared to the standard method, thermogravimetric analysis. The comparison between these two methods can be seen in Table 4.3. Both the APTES and CES samples give a very small amount of ligand detected in solution by qNMR, whereas effectively all of the APDMMS is observed by qNMR.

Table 0.3 Comparison of Functional Group Quantification Using TGA and qNMR.

Sample	qNMR (mmol/g)	TGA (mmol/g)	Detected by NMR
MSN@APDMMS	1.20	1.15	~100%
MSN@APTES	0.00499	0.607	~1%
MSN@CES	0.0733	1.53	~5%

These results suggest two different types of supramolecular binding of ligands to the surface. The APTES and CES ligands appear to be bound to the surface via a tridentate mode of bonding. Examining the ligand structures, it becomes apparent that tridentate binding to the surface can result from the formation of up to three siloxane bonds between the ligand and the surface. In order to release the molecule into free solution, all of these bonds must be broken. The APDMMS molecule, on the other hand, seems to be completely released from the surface. APDMMS can only form one siloxane bond due to the di-methylated status of the central silicon atom; thus only this single siloxane bond needs to be hydrolyzed to release the free molecule into solution.

4.4.6 Model of Supramolecular Ligand Release and Binding

Overall, the data presented here enable a new paradigm for understanding the labile nature of ligands bound to mesoporous silica surfaces in solution. The data is

indicative of hydrolysis of the single siloxane bond between APDMMS and the mesoporous silica surface, facilitating its release into solution (Figure 4.14).

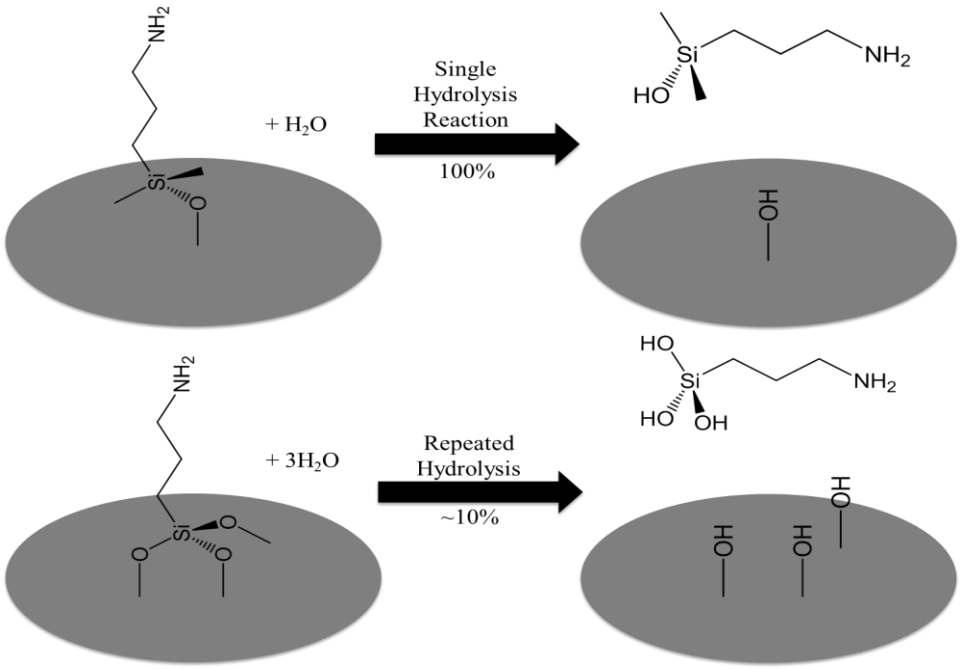

Figure 4.14 Overall reaction schemes for the hydrolysis of organosiloxanes from the MSN surface, depicted for the two amines used in the study. The upper panel shows the reactions for which only a single siloxane bond can form between the surface and the organosilane (as for APDMMS). The lower panel describes hydrolytic reactions that release molecules capable of forming multiple siloxane bonds with the surface (such as APTES and CES).

Upon release into solution, these molecules can sorb onto the surface in a dynamic equilibrium. It seems likely these molecules are in different spheres around the nanoparticle and are capable of undergoing dynamic chemical exchange. A multi-shell model (Figure 4.15) was developed in which APDMMS and similar ligands can exchange between the shells through several mechanistic processes including lateral diffusion and inner sphere-outer sphere exchange. The DOSY results then arise from the ligands in the inner and outer shells that can easily exchange with molecules in the bulk

solvent. The bound molecules in the inner sphere are what then give rise to the strongly bound result seen in the NOESY spectrum.

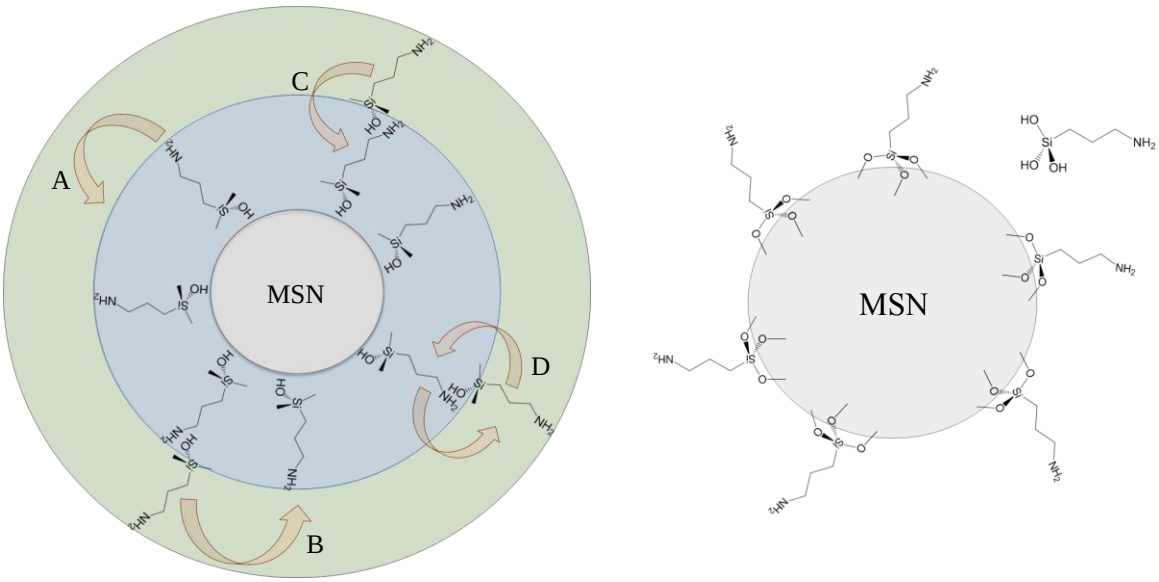

Figure 4.15 Proposed model of supramolecular ligand dynamics. Two cases present themselves based on the data. The left diagram describes molecules (like APDMMS) that are capable of forming a single siloxane bond with the surface. The molecules are rapidly hydrolyzed from the surface and then partition into shells of binding to the surface. The inner shell (blue) contains strongly bound ligands while the outer shell (green) contains weakly bound ligands. Ligands can freely exchange through several processes described in the main text. The right diagram describes molecules (like CES and APTES) in which partial hydrolysis leads only to a small amount of ligand released from the surface; this does not involve chemical ligand exchange dynamics. The MSN core is the same diameter in both diagrams.

The mechanisms by which the molecules may exchange include lateral diffusion across the surface either in the inner sphere (A) or the outer sphere (B), ligand displacement wherein an inner sphere ligand is displaced by a nearby outer sphere ligand (C), or inner sphere-outer sphere exchange in which nearby ligands cross-exchange with each other across the inner sphere-outer sphere boundary (D). We suggest that the observed data most likely results from a combination of these ligand exchange processes. Previous work in the literature shows similar chemical exchange mechanisms for thiol

ligands on gold nanoparticles.[70] The Au-S bond formed from thiol-gold NP interactions is fairly strong relative to strength of the sorption indicated for the mesoporous materials investigated here. It can therefore be expected that the mechanisms of exchange are quite different in this case as no true covalent bond can be expected to form between hydrolyzed molecules and the surface, as it does for gold-thiol systems.

The APTES and CES molecules, however, appear from the NMR data presented here to be strongly bound to the surface, with only a small amount (~5%) hydrolyzed into solution. These molecules, in contrast to APDMMS, seem to be free in solution, with little to no exchange post-hydrolysis with bound molecules. Two effects seem to be responsible for the observed data. First, the amount of released ligand in the APTES and CES cases is very small. Even if dynamic equilibrium is occurring, the amount of free molecule that would be detected during NMR experiments is very small. Further, the amount of free exchange sites (surface silanols without a covalently-bound molecule) on the surface are rather small, approximately on the order of the amount released (~10%). This provides few, if any, sites for adsorption to occur. Thus, even if there is exchange happening in these two cases, the NMR experiment may be unable to detect it. Therefore, it can be expected that the signal-limited spectra may not show the true behavior if in fact the molecules are exchanging, but are simply not above the detection limit. This is particularly true for the NOESY experiments as there is a major loss of signal in 2D experiments. The DOSY experiments, however, are only a pseudo-2D experiment and do not suffer from this limitation.

The second issue is that, based on SPARTAN calculations for these molecules, the molecular geometry and the overall molecular dipole moment around the central

silicon atom seems to dictate the ability of free ligands to adsorb to the surface. In the APDMMS case, the two methyl groups attached to the silicon are diverted away from the O-H of the APDMMS silanol moiety, allowing enough steric headspace for it to bind to the surface through a combination of hydrogen bonding and polarity interactions. The APTES and CES molecules, however, have all three silanol O-H moieties effectively in a plane with the silicon atom. This generates enough steric hindrance that the molecules may not be able to effectively bind. Perhaps, more realistically, they do in fact bind to the surface but due to the steric hindrance they bind very weakly and are easily displaced by solvent molecules.

As a means of evaluating the ligand dynamics, an equimolar amount of free ligand was added to the CES-functionalized material and the diffusion coefficients were measured using DOSY NMR. The result of this experiment, also given in Table 4.2, gives diffusion coefficients that are smaller than that of just the functionalized material. This difference of 20% is significant; considering experimental errors due to fluctuations in temperature and signal-to-noise limitations give errors around ten percent, as well-described in the literature.[71] These results suggest that the protons, and thus the molecule itself, are moving less rapidly in this sample. The implication of this result is that the molecule may be in a dynamic exchange regime similar to the APDMMS system, but it is not very tightly bound. Otherwise, the NOESY spectra should have revealed spin-diffusion effects arising from bound molecules. Alternatively, the amount of bound molecule could be very low at any time and so only the truly free molecules are observed by NOESY, or the exchange is so rapid that the weighted-average result indicates only molecules that are in a free state. Both of these are viable options for why the APTES and

CES samples appear only to be free in solution. As stated previously, the molecules in solution may dimerize which would result in a smaller diffusion coefficient due to their increased size.

The results presented here are surprising in that the organosiloxanes commonly employed as ligands have generally not been viewed as labile. One thing that remains unclear is precisely how the ligands are released from the surface. It seems likely that since these functional groups have acid-base properties the moieties will self-catalyze release from the surface through acid- or base-catalyzed hydrolysis of the siloxane bond(s). Future efforts should address the effect of pH on these materials because a strongly pH-dependent effect is expected if this hypothesis is correct. Another aspect that needs to be addressed is the precise mechanism by which the APDMMS molecules exchange with the surface. We have envisioned a multi-shell model with molecules rapidly equilibrating throughout these shells. However, the exact mechanistic details, particularly conformational changes in the ligands would be very useful for understanding how these molecules adsorb onto the surface of the nanoparticles. Thermodynamic parameters would be of particular interest in assessing, ideally, both exact structure as well as dynamics of these molecules, which seem to be adsorbed onto the nanoparticle surface and seem capable of undergoing dynamic exchange in aqueous solution at the solid-liquid interface.

4.4.7 Conclusions

This study represents the first case of applying solution-phase NMR toolbox methods to covalently-functionalized mesoporous silica nanoparticles. The results indicate a dynamic system as opposed to the long-held concept of static surface

chemistry, and that the mode of bonding to the surface determines the extent to which the ligands are labile. These results suggest that in any application of these materials, the surface chemistry may present dynamic exchange equilibria dependent on the nature of the functional group and its solution environment. This can be considered either a positive or a negative characteristic depending on the desired application; but it must be considered for implementation of these materials into drug delivery, environmental remediation, and catalytic applications of these materials in aqueous, solvated environments.

CHAPTER 5
ROS GENERATED FROM SILICA NANOPARTICLES AND ITS RELATION TO CELLULAR TOXICITY

5.1 Abstract

Evaluating toxicological responses of engineered nanomaterials such as silica nanoparticles is critical in assessing health risks and exposure limits. Biological assays can be used to evaluate cytotoxicity of individual materials, but specific nano-bio interactions—which govern its physiological response—cannot currently be predicted from materials characterization and physicochemical properties. Understanding the role of free radical generation from nanomaterial surfaces facilitates understanding of a potential toxicity mechanism and provides insight into how toxic effects can be assessed. Size-matched mesoporous and nonporous silica nanoparticles in aminopropyl-functionalized and native forms were investigated to analyze the effects of porosity and surface functionalization on the observed cytotoxicity. In vitro cell viability data in a murine macrophage cell line (RAW 264.7) provides a model for what might be observed in terms of cellular toxicity upon an environmental or industrial exposure to silica nanoparticles. Electron paramagnetic resonance spectroscopy was implemented to study free radical species generated from the surface of these nanomaterials and the signal intensity was correlated with cellular toxicity. In addition, in vitro assay of intracellular reactive oxygen species (ROS) matched well with both the EPR and cell viability data. Overall, spectroscopic and in vitro studies correlate well and implicate production of ROS from a surface-catalyzed reaction as a predictor of cellular toxicity. The data demonstrate that mesoporous materials are intrinsically less toxic than nonporous materials, and that surface functionalization can mitigate toxicity in nonporous

materials by reducing free radical production. The broader implications are in terms of safety by design of nanomaterials, which can only be extracted by mechanistic studies such as the ones reported here.

5.2 Introduction

Evaluating the toxicity of nanomaterials, commonly referred to as nanotoxicity, is a rapidly growing field of research.[72-73] As engineered nanomaterials diversify in type and synthetic complexity, exposures to these materials will increase in both direct (biomedical) and indirect (environmental) pathways. Porous nanomaterials such as mesoporous silica are undergoing rapid development for a variety of applications such as drug delivery, catalysis, biomedical imaging, and environmental remediation.[74-77] There is a growing body of literature aimed at assessing risks of nanomaterials. However, correlations between specific nanomaterial properties and toxicity in biological systems remain lacking.

Current research focuses on *in vitro* methodologies to determine the biological impact of nanomaterials. In the case of silica nanomaterials, current studies focus on different types of silica, such as fumed silicas, porous silicas, and nonporous materials. Porous silica nanomaterials exhibit very low cytotoxicity against a variety of cell lines.[78] The synthesis of each material gives it a unique chemical surface that influences how it interacts with biological systems. These nano-bio interactions ultimately control the reactions, interactions, and fate of these materials. Despite the lack of systematic studies, several themes have emerged that appear to be central paradigms for understanding and predicting silica nanoparticle toxicity. Two of these factors are the surface silanol density and the production of reactive oxygen species (ROS).[9, 79-80]

The primary structure of silica nanoparticles consists of tetrahedrally-bonded Si-O moieties that are amorphously condensed into a network. Porous materials possess pore-voids around which the tetrahedra are condensed, but in the nonporous variant there are only amorphous silica tetrahedra present. On the surface of the material there are free silanol moieties (Si-OH), which are analogous to alcohol functionalities. Work in the field has shown that these surface silanols are important factors that control interactions with biological systems.[81] Surface silanols are negatively charged at physiological pH (as silicate anion $Si\text{-}O^-$), and thus can interact with biological components such as cell membranes via electrostatic interactions.[82] Furthermore, the silanol oxygen is nucleophilic, which means it is mechanistically viable to attack electrophilic carbonyl groups, which are present in protein molecules. Due to the nature of the hydrolysis and condensation of the precursor molecules, each type of material has different densities of surface silanols, as well as different types in terms of their coordination at the surface.[83] While surface silanols are important in understanding toxicity, their reaction with biological macromolecules can screen them from interacting with other molecules in biological compartments.

Generation of ROS from the silica surface has long been held to be a dominating factor in toxicity. For some time, it was believed that ROS were produced via Fenton-like chemistry.[84] More recent work implicates ROS production at the nanoparticle surface as a factor. In the case of fumed silica, Zhang et al. showed that the cleavage of strained siloxane rings were responsible for the production of ROS from the silica nanoparticle surface.[79] It has been shown that nanoparticle-derived ROS can overcome the natural cellular defense mechanism, glutathione-mediated redox chemistry. Production of species

such as hydroxyl radical results in destructive chemical modification of lipids and DNA, as well as conversion to organic peroxynitrite ($R\text{-}ONOO^-$) via reaction with nitric oxide, as previously described.[24]

Increased intracellular ROS leads to oxidative stress in the cell. Oxidative stress has deleterious effects if sustained for extended periods of time or at high levels for acute periods. Damage to the cellular machinery can result in apoptosis, or programmed cell death. This has been observed to happen upon exposure to nanomaterials. This has been investigated, and oxidative stress has been measured through a variety of methodologies. Some work has suggested there is a band gap-redox potential relation that correlates with oxidative stress upon exposure to metal oxide nanoparticles.[85] Some work has shown that some nanoparticles like ceria (CeO_2) actually protect against oxidative stress, and that materials such as titania (TiO_2) do not seem to have any oxidative effect in certain cell lines.[86] As mentioned above, the cellular defense against oxidative stress is redox chemistry mediated by glutathione, which the cell keeps reserves of and regenerates as necessary. When cells are exposed to nanoparticles that induce oxidative stress, these glutathione reserves can be depleted, as has been measured. Once the reserves are depleted, the ROS generated can damage cellular components ultimately leading to cell death.[87]

In terms of sustainable nanotechnology, a natural extension of these insights is that chemical modification of the surface may be able to mitigate the toxicity of silica nanomaterials by reducing ROS formed. This has been verified experimentally, and overall functionalization of the surface does seem to decrease cellular toxicity in *in vitro* models.[88-89] Surface functional groups added to the surface vary widely, from small

alkylamine groups to large non-ionic molecules such as polyethylene glycol (PEG). It has been postulated, but not clearly demonstrated, that this decrease in cytotoxicity arises from a decrease in total surface silanol density, as well as modification of the overall particle surface charge. However, investigation into the mechanism by which surface modification mitigates toxicity is still ongoing, as it is not fully understood.[90]

The study presented here explores the fundamental relationship between surface properties and the toxicological response of engineered silica nanoparticles, and how this insight can be used to inform and guide "safety by design" approaches for nanomaterials. Particles used were size-matched at approximately 50 nm in diameter. In terms of biological applications (such as drug delivery/biomedical imaging), the size of less than 100 nm is critical to prevent rapid clearance from the systemic circulation by the reticuloendothelial system.[91] Wormhole-type mesoporous silica and nonporous silica were synthesized to examine the effects of porosity on cytotoxicity and free radical production. The materials were further functionalized with a small organic amine, which is commonly used to increase the overall surface charge as well as enable further chemical modification. Thus, the synergistic effects of porosity and surface functionality could be evaluated for amorphous silica nanoparticles, with the goal of correlating the physicochemical properties to observed, *in vitro* cellular toxicity.

5.3 Experimental Methods

5.3.1 Silica Nanoparticle Synthesis and Functionalization

Mesoporous silica nanoparticles of WO morphology and nonporous silica utilized for the experiments in this Chapter were synthesized using methods described in Chapter 2 above, Sections 2.2 and 2.3, respectively. The nanoparticles were functionalized with APTES using the methodology described in Chapter 2, Section 2.4.1.

5.3.1 Electron Paramagnetic Resonance (EPR) Spectroscopy

EPR was employed to measure reactive oxygen species released from the nanoparticle surface, adapting a previously published method.[79] Samples were prepared at 5% weight dispersion in 500 µL final volumes. A solution containing hydrogen peroxide at 200 mM final concentration and the spin-trap 5,5-dimethyl-1-pyrroline N-oxide (DMPO) at a final concentration of 25 mM was added to the powdered materials, mixed, and then equilibrated at room temperature for 15 min prior to measurement on a Bruker EMX CW EPR spectrometer operating at a Larmor frequency of 9.76 GHz (X-band). A flat TE_{102} quartz (Suprasil) cell was used to hold the samples and four scans were co-added to give the final spectra. Quantification was facilitated by using 3-carboxy-PROXYL as an external standard. Double integration of the standard and sample spectra gave areas that were used to calculate the concentration of each radical species.

5.3.2 Cell Culture and Viability Assay

Murine leukemia macrophage cells (RAW264.7) were maintained in RPMI-1640 medium (Gibco, Life Technologies) supplemented with 10% fetal bovine serum (Atlanta Biologics), 10 mM HEPES (Gibco), 1 mM sodium pyruvate (Gibco), 1 mM Glutamax (Gibco), and 50 µg/mL gentamycin sulfate (Cellgro). Cells were incubated at 37 °C and 5% CO_2.

RAW264.7 cells were seeded in 96-well plates at 1.0×10^4 cells per well and incubated for 24 hours at 37 °C and 5% CO_2. The medium was removed from the wells and replaced with 200 µL of particle suspension in fresh RPMI medium. Cells were exposed to particle treatments for 4, 24 or 48 hours after which the treatments were removed and fresh medium was added. MTS reagent (3-(4,5-dimethylthiazol-2-yl)-5-(3-

carboxymethoxyphenyl)-2-(4-sulfophenyl)-2H-tetrazolium) or CellTiter 96 Aq_{ueous} One Solution reagent (Promega) was then added to the medium in the wells and incubated at 37 °C for 1-4 hours depending on the rate of formazan production. Before spectrophotometry, the 96-well plates were centrifuged at 500 *x g* for 20 minutes; the supernatant of each well was removed and added to a new 96-well plate. This step was performed to avoid any unwanted scattering from the particles during the absorbance measurement. The absorbance of the supernatant was collected at 420 nm using a SpectraMax Plus 384 microplate reader (Molecular Devices). Percent relative cell viability was calculated by normalizing treated cells to an untreated control sample. Medium and MTS reagent without cells served as a method blank for all samples.

5.3.3 *In Vitro* ROS Assay in RAW 264.7 Cell Line

RAW264.7 cells were seeded in 60 mm culture dishes at a density of 2×10^5 cells per dish and incubated at 37 °C and 5% CO_2 for 24 hours. After the initial incubation, the medium was aspirated and replaced with fresh medium. Then, 200 µL of particle suspension in medium were added at a final concentration of 50 µg/mL. After 24 hours of treatment, the medium was aspirated and the cells were removed from the culture dish using trypsin. After five minutes fresh medium was added to the trypsinized cells; the cells were washed several times from the dishes and collected in centrifuge tubes. The cells were washed twice with PBS (Gibco) containing 5 mM sodium pyruvate (Gibco) and centrifuged at 230 g for 5 minutes in between washes. Then, each sample was resuspended in 1.00 mL of the PBS/pyruvate solution and stained with dihydroethidium (DHE) (Molecular Probes, Life Technologies) dissolved in dimethyl sulfoxide (Aldrich). The final concentration of DHE was 10 µM. To account for any background

fluorescence, a negative control sample consisted of untreated cells with the same volume of DMSO added as in the DHE stained samples. Antimycin A (Aldrich) was added to untreated cells at a final concentration of 10 μM to serve as a positive control followed by immediate staining with DHE using the exact same conditions as in the nanoparticle treated samples. All samples were incubated for 40 minutes after the addition of DHE (or DMSO for the negative control) at 37 °C after which they were placed on ice and analyzed for DHE fluorescence using a FACScan flow cytometer (Becton Dickinson Immunocytometry Systems) using 488 nm excitation and measuring the emission at 585 nm. The mean fluorescence intensity of three samples was used to compare the relative generation of intracellular superoxide.

5.4 Results and Discussion

5.4.1 Material Design and Physical Characterization

The materials used in this study were wormhole-type (WO) mesoporous silica and nonporous silica nanoparticles, approximately 50 nm in diameter. The WO mesoporous silica material has a network of pores that is less ordered than that of other mesoporous silica materials, such as MCM-41 and SBA-15. The pores of WO-type silica form a network of voids that interconnect and interrupt each other throughout the material. The materials were characterized using traditional physical characterization methods. Electron microscopy images and physical characterization data can be seen in Figure 5.1 and Table 5.1, respectively.

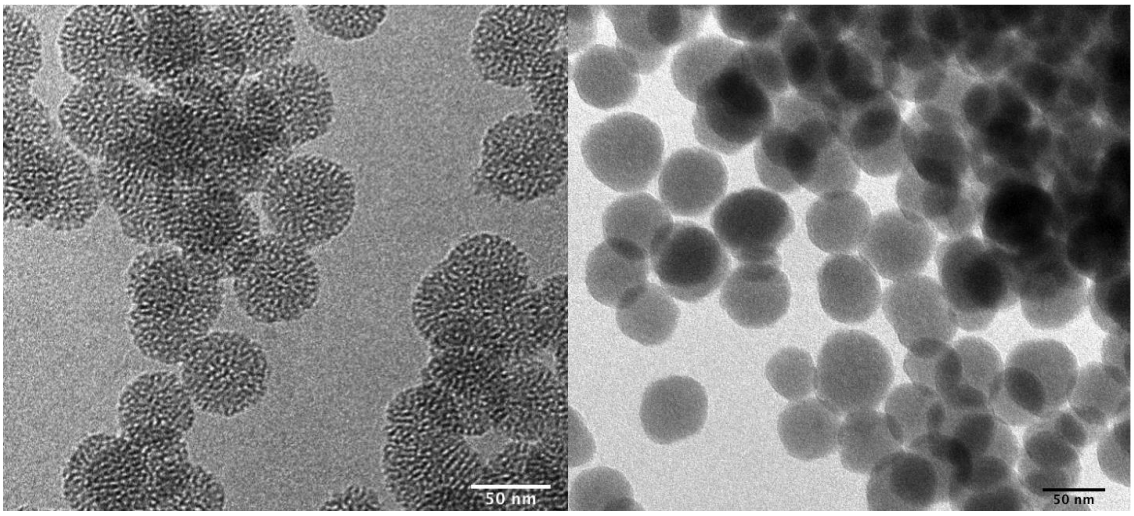

Figure 5.1 Transmission electron microscopy images of materials used in this study. Wormhole-type (WO) mesoporous silica (L) and nonporous (Stöber) silica (R). The scale bar in each image is 50 nm.

Table 0.1 Physical Characterization of Nanomaterials.

Sample	Diameter (nm)	Surface Area (m^2 /g)	Pore Volume (mL/g)	Pore Diameter (nm)	Functional Group Loading (mmol/g)	ζ Potential (mV) pH = 7.4, 10 mM Sodium Phosphate
Mesoporous Silica (MS)	49 (± 5) TEM	1100 (± 44)	0.56 (± 0.03)	3.100 (± 0.007)	4.283 (0.009)	-39 (± 2)
MS@APTES	-	700 (± 28)	0.152 (± 0.009)	3.100 (± 0.007)	N/A	1.9 (± 0.2)
Nonporous Silica (NPS)	47 (± 7) TEM	66 (± 3)	N/A	N/A	0.582 (0.001)	-49 (± 3)
NPS@APTES	-	42 (± 2)	N/A	N/A	N/A	9.6 (± 0.7)
Min-U-Sil (α-Quartz)	270 (± 21) DLS	7.7 (± 0.3)	N/A	N/A	N/A	-67 (± 3)

The surface area and pore volume decreases upon functionalization, as previously observed and reported in the literature.[92] The nonporous and mesoporous silica nanomaterials were size-matched so that variations in porosity and surface functionalization could be correlated with cytotoxicity.

5.4.2 *In Vitro* Cellular Toxicity

The toxicity of these materials was evaluated using a cell viability assay against a murine macrophage cell line (RAW 264.7). As immune cells, macrophages respond to the presence of nanomaterials in a biological system. Macrophages mitigate inflammation responses via cytokine induction and other pathways.[93] Additionally, previous work has demonstrated a clear ability of these cell types to uptake nanoparticles by phagocytosis increasing the local concentration inside the cellular compartment.[94] In order to assess the time- and concentration-dependent effects, an array of dosages were implemented ranging from 10-200 μg/mL. Cell viability was monitored as a function of time at intervals of 4, 24, and 48 hours. The results at 48 hours can be seen in Figure 5.2.

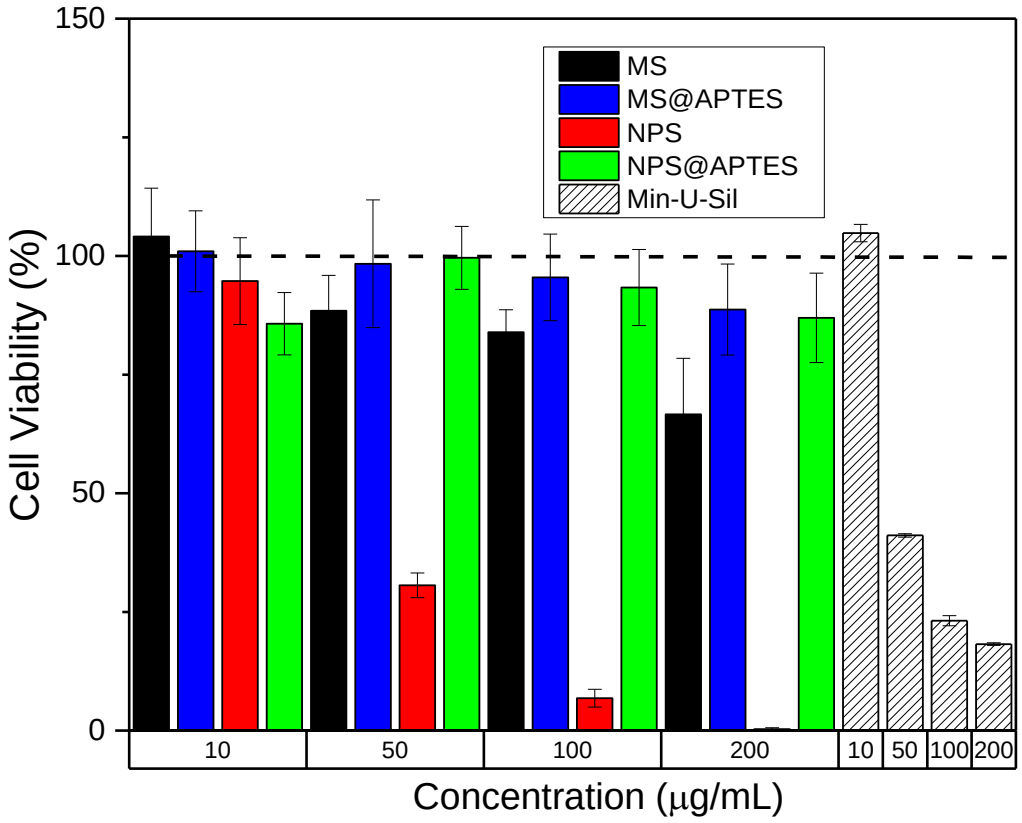

Figure 5.2 Cell toxicity data in RAW 264.7 cells, 48 h post-exposure. Min-U-Sil data, also at 48 h, is shown as the positive control for comparison. [Data from A. S. Morris.]

In terms of concentration effects, there is a marked effect of concentration on

viability for the bare nonporous silica. At the highest concentration tested (200 μg/mL) effectively all cells for that dosage were no longer viable at 48 hours post-exposure. There is also some slight concentration-dependent effect on cell viability from the bare mesoporous silica, but not nearly as apparent as that for the nonporous material. The two functionalized materials showed very little observed toxicity at the concentrations tested. This is consistent with previous studies which implicate that surface functionalization lowers toxicity by modification of surface charge and reduction in the number of free surface silanols.[95] The only clear time-dependent effect was again observed in the nonporous silica, which showed a clear trend over time in terms of cell viability.

Previous work in the field has looked at effects of porosity in the interaction of silica nanoparticles with RAW 264.7 macrophage cells. Yu, et al., for example, observed similar trends, with the functionalized porous and nonporous materials showing mitigated toxicological responses across the dosage range evaluated.[96] Using propidium iodide staining, it was observed that nonporous silica nanoparticles instigated an approximately four-fold larger disruption to the macrophage cell membrane than the mesoporous nanoparticles. A caveat is that the materials used in the previous study were slightly larger than 100 nm, and so their size regime effects cannot be directly compared to our data. Still, Maurer-Jones, et al. have shown elevated hemolytic activity for smaller nonporous particles (~25 nm) across a similar concentration range.[9] The particles in our study, which are of intermediate size, then fit directly into this previous work but with an added dimension of the effects of functionalization on the observed toxicity.

5.4.3 EPR Spectroscopy and Quantification of Free Radical Species

As a means of assessing ROS produced from the surface, electron paramagnetic resonance (EPR) spectroscopy was employed. EPR has been used previously to assess radical formation in many different systems of interest, including *in vivo* studies. Here, it has been used to detect and quantify hydroxyl radical ($HO^{\bullet}$) produced from the homolytic cleavage of hydrogen peroxide:

$$H_2O_2 \rightarrow 2\ {}^{\bullet}OH$$

This has been previously carried out in a study by Zhang et al. in which they looked at the processing pathway dependence of the material on its toxicological effects.[79] Zhang's work focused primarily on fumed silica, whereas our study focuses instead on colloidal silica prepared via hydrothermal synthesis. In Zhang's work, the observed toxicity was attributed to the formation and cleavage of strained siloxane rings on the surface, leading to ROS formation. Due to the hydrothermal nature of the synthesis of the materials used in this study, any strained rings would have been broken during the synthetic process and subsequent washing steps. However, it is still reasonable to expect that ROS may form from surface-catalyzed homolytic cleavage of hydrogen peroxide.

In these EPR studies, H_2O_2 was implemented to mimic a cellular reserve of molecules that may undergo chemical modification by interaction with the nanoparticle surface. Furthermore, work in the field has elucidated the effect nanoparticle exposures can have on oxidative stress in biological systems. Natural redox-active protection mechanisms can quickly be overcome by an influx of ROS species via uncontrolled chemical reactions in intracellular or extracellular compartments. Due to the reactive nature of the hydroxyl radical, direct detection, even using highly sensitive EPR spectroscopy, is not feasible.

However, a common method to observe and quantify free radical species that evade direct detection is enabled by using a spin-trap. These are commonly utilized and have great application to studying complex biological systems. The spin traps most commonly used are nitrone spin traps like 2,2,6,6-tetramethyl-1-piperidinyloxy (TEMPO) which form a spin adduct with the hydroxyl or other radical species:

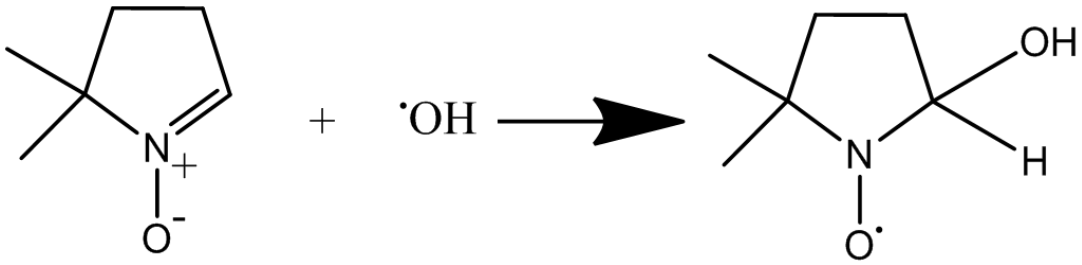

Figure 5.3 Reaction between DMPO molecule and free hydroxyl to give DMPO-HO• spin adduct which is detectable by EPR spectroscopy. The unpaired electron primarily localizes on the oxygen atom.

The half-life of these spin adducts is quite long, on the order of tens of minutes to hours.[97] Therefore, detection and quantification of the radical signals is possible by implementing a spin trap. EPR spectra for the detected hydroxyl radical spin adduct for the materials can be seen in Figures 5.4 and 5.5. As a standard convention, these are reported as the derivative of the signal with respect to the magnetic field strength (in Gauss). The DMPO-HO• spin adduct gives a characteristic 1:2:2:1 spectrum centered at approximately 3490 Gauss in the X-band (ν_L = 9.79 GHz) region. This four line spectrum arises from splitting of the peaks via coupling of the unpaired electron to the nearby nitrogen as well as the hydrogen at the beta position, with measured hyperfine coupling constants of a_N = 14.9 G and a_H = 14.9 G, matching those reported in the literature.[98]

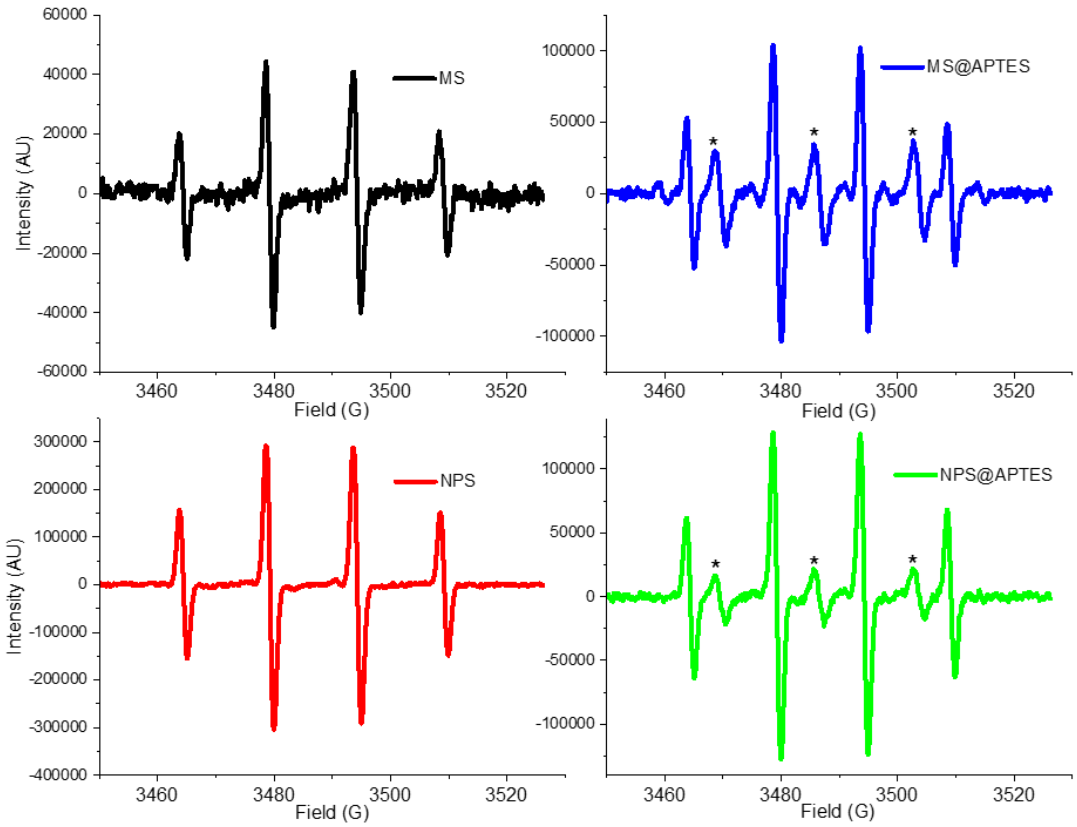

Figure 5.4 EPR spectra of the materials to quantify hydroxyl radical ($HO^{\bullet}$) produced by surface-catalyzed decomposition of H_2O_2. The DMPO-$HO^{\bullet}$ spin adduct is characterized by the four line spectrum shown of intensity 1:2:2:1, and the asterisk (*) indicates aminoxyl radical generated by oxidation of the amine functionality.

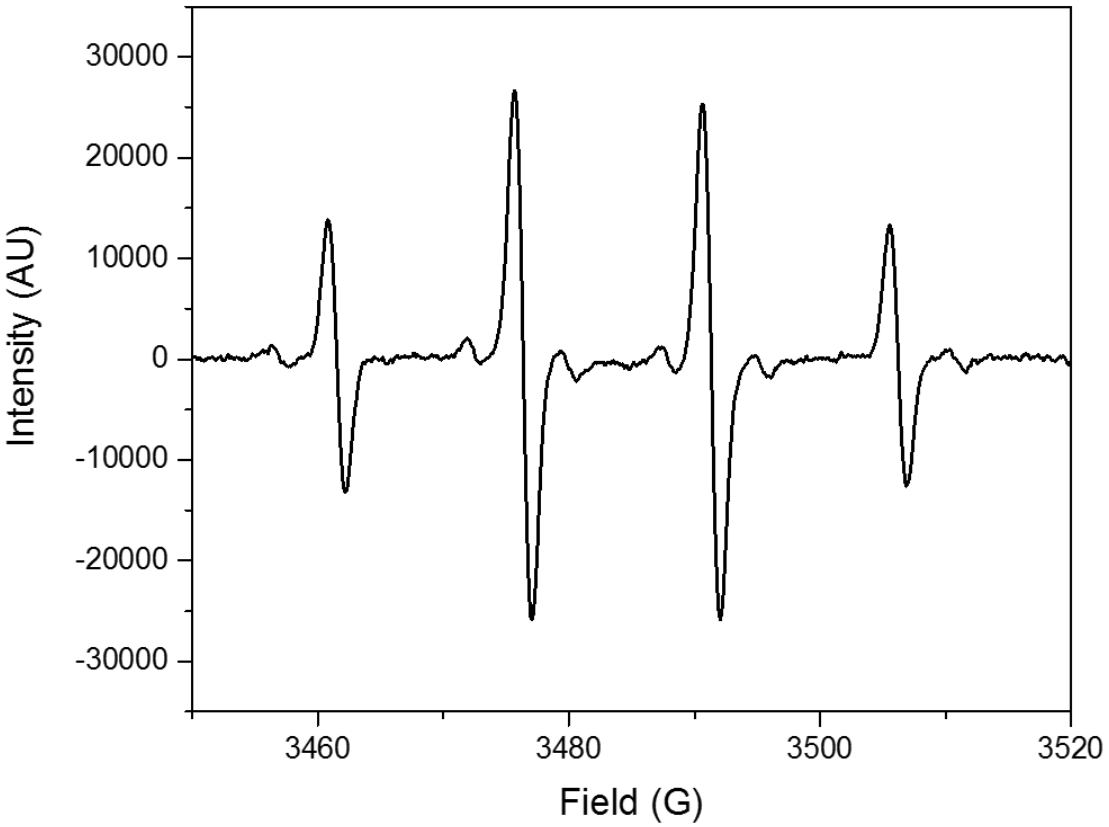

Figure 5.5 EPR spectrum of Min-U-Sil in water with added peroxide.

It is of particular interest that additional peaks are present in the amine-functionalized samples. The peaks in between the four signals corresponding to the DMPO spin adduct have been assigned to aminoxyl (IUPAC recommended name for $[R_2N–O^{\cdot}] \leftrightarrow [R_2N^{\cdot+}–O^{-}]$) radical. This is not surprising, as it is easy to imagine that due to the high peroxide concentration the amine has become oxidized to form an aminoxyl radical, which is more stable than free hydroxyl radical. The structure of the molecule would arise from oxidation of the APTES such that it has the structure similar to R-NHO$^{\bullet}$ with the unpaired electron on the oxygen being detected by the EPR measurement. This type of aminoxyl radical formation is noted in the literature to occur under oxidizing conditions.[99] From the EPR spectrum of the functionalized materials, hyperfine coupling

constants of a_N = 17.1 G are calculated for the 1:1:1 aminoxyl, which match well with other aminoxyl radicals (a_N = 16.9 G) observed in aqueous solution by others.[100] The aminoxyl radical has been simulated using the EasySpin simulation package and compared to the experimental data, which is shown in Figure 5.6.[101] This comparison shows agreement between the simulated and experimental aminoxyl EPR spectrum.

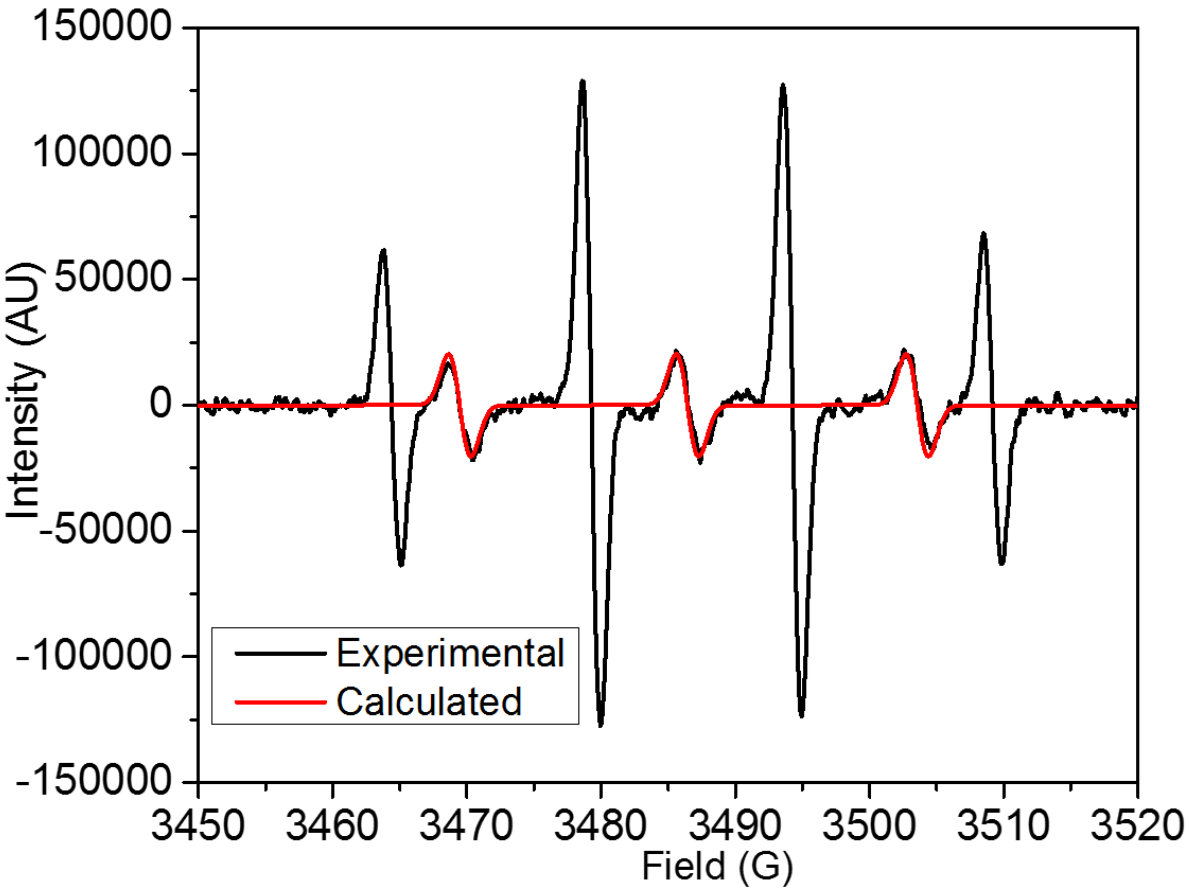

Figure 5.6 Comparison of experimental MS@APTES EPR spectrum with a calculated EPR spectrum for the proposed aminoxyl radical calculated using EasySpin (garlic). The spectral intensity of the calculated spectrum has been matched to that of the experimental spectrum.

Double integration followed by comparison with an external standard, in this case 2-carboxy-PROXYL, facilitates quantification of the hydroxyl species in solution. The signals were integrated twice to give first an absorption lineshape and then finally an integrated intensity, which was compared to a 2-carboxy-PROXYL solution of known

concentration to calculate the absolute radical concentration. A plot of the absolute radical concentration for both the hydroxyl and aminoxyl radical species for each material is given in Figure 5.7.

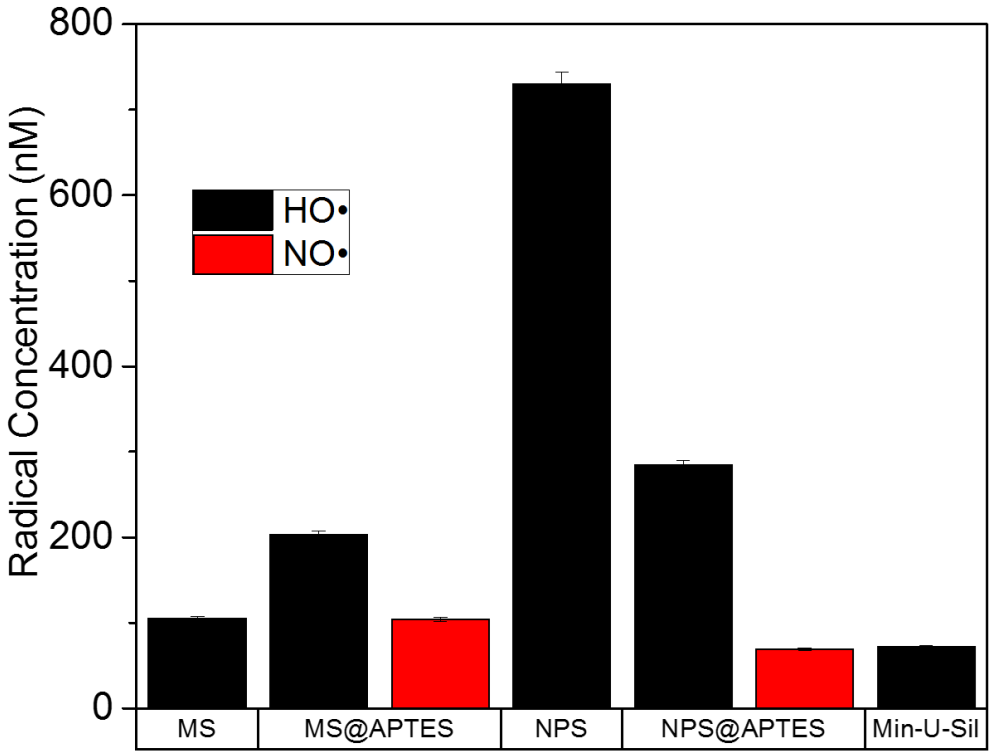

Figure 5.7 Absolute radical quantification from EPR spectroscopy conducted in water with DMPO spin trap and added H_2O_2. The type of radical is differentiated by color according to the legend.

Mostly notably the concentration of hydroxyl radical in the bare nonporous silica is the highest of all measured samples, and is significantly higher when compared to its mesoporous analogue. This is surprising when you consider the approximate 20-fold difference in their surface areas. One would expect much more radical to form on the mesoporous silica surface, yet the opposite is observed, with a seven-fold larger concentration from the nonporous compared to the porous material. Additionally, due to an approximate 60% pore void volume in the mesoporous material, there are many more particles per same unit of mass. In the case of the bare materials, a volumetric calculation

based on assumptions of silica density from the literature gives values of 1.9×10^{16} particles/g for the mesoporous material, and 6.9×10^{15} particles/g for the nonporous material.[102] This is approximately a factor of three difference in particles per gram, yet the nonporous material shows an almost seven-fold larger concentration of radicals based on the EPR measurement.

The surface area of the material is expected to dictate the total amount of radical produced, with materials having larger surface area capable of producing more free radicals than materials of lower surface area. It can therefore be assumed that materials such as mesoporous silica will generate more free radicals than nonporous materials on the same mass unit basis. In order to account for this trend, the absolute concentration has been converted to radical production in terms of the pmol radical per m^2 surface area. This radical production can be seen in Figure 5.8, showing the radical production as a function of radical type and material.

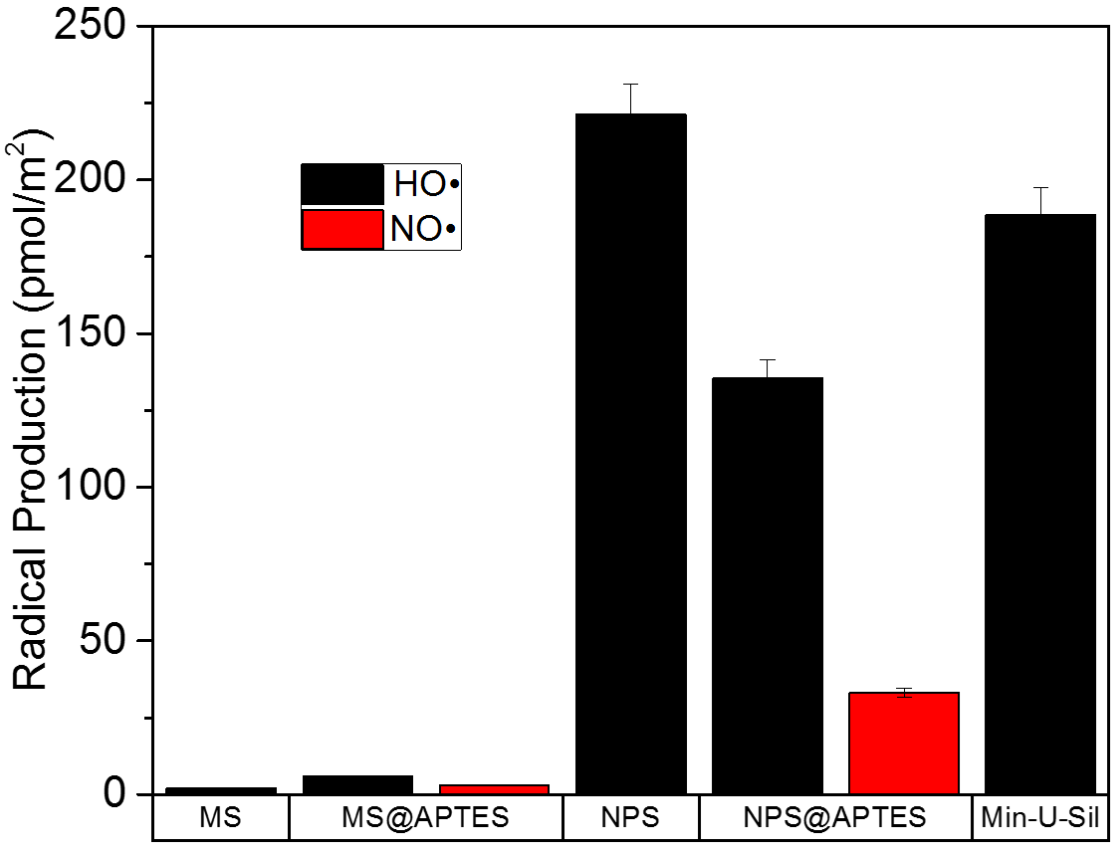

Figure 5.8 Radical production as a function of material and radical type. These values are obtained by normalizing for the different surface areas of each material as determined by BET adsorption isotherm.

Due the very high surface area of the mesoporous material, the radical production per unit area is very low. Comparing the bare materials, a two orders-of-magnitude difference between mesoporous and nonporous silica was observed. Also of note is that amine-functionalization decreases hydroxyl radical production in the nonporous silica. One result that remains puzzling is that functionalization of the mesoporous material results in an *increase* in total radical production. This is not expected, and is the opposite of the trend observed in the nonporous silica samples.

A final issue of note is that normalization of the radical concentration to radical production gives the positive control, Min-U-Sil, a large production of radical per surface area. Min-U-Sil, or α-quartz, is very toxic as a crystalline material which is thoroughly

noted in the toxicological literature, and why it was implemented in these studies as a positive control.[103] The EPR data demonstrate that a large amount of radicals can arise from a very small surface area of the material (~7 m^2/g) for quartz. This implies that perhaps it is its capability to produce large amounts of free radicals that results in such potent toxic effects in biological systems. A caveat is that the quartz used in these studies is approximately five times the size of the other materials, which were deliberately size-matched. Thus, the toxicological effect of the quartz cannot be isolated as separate from its larger physical size.

The experiments in aqueous solution provide great insight into the quantitative nature of free radical production at the nanoparticle surface. However, this is clearly in a simplified chemical environment when compared with the toxicity assay. As an extension of this, the EPR experiments were repeated, but this time the RPMI culture medium was used as the solution of interest. DMPO and H_2O_2 were added and the EPR spectra were collected. The same quantification and conversion to radical production values was applied to give the EPR spectra (Figure 5.9) and the calculated radical production (Figure 5.10). Overall the signals are much attenuated. This makes sense as from a collision theory perspective the produced radicals are much more likely to interact with one of the many other molecules (amino acids, vitamins, etc.) in the culture medium rather than with the spin trap. The general trend is overall the same, although the absolute intensity of the NPS@APTES sample is actually higher than in the EPR experiments conducted in water. This is puzzling and counter to the other results. However, a caveat with this data is that the absolute concentrations (~10 nM) are close to the detection limit so the quantification must be interpreted conservatively due to possible technical limitations.

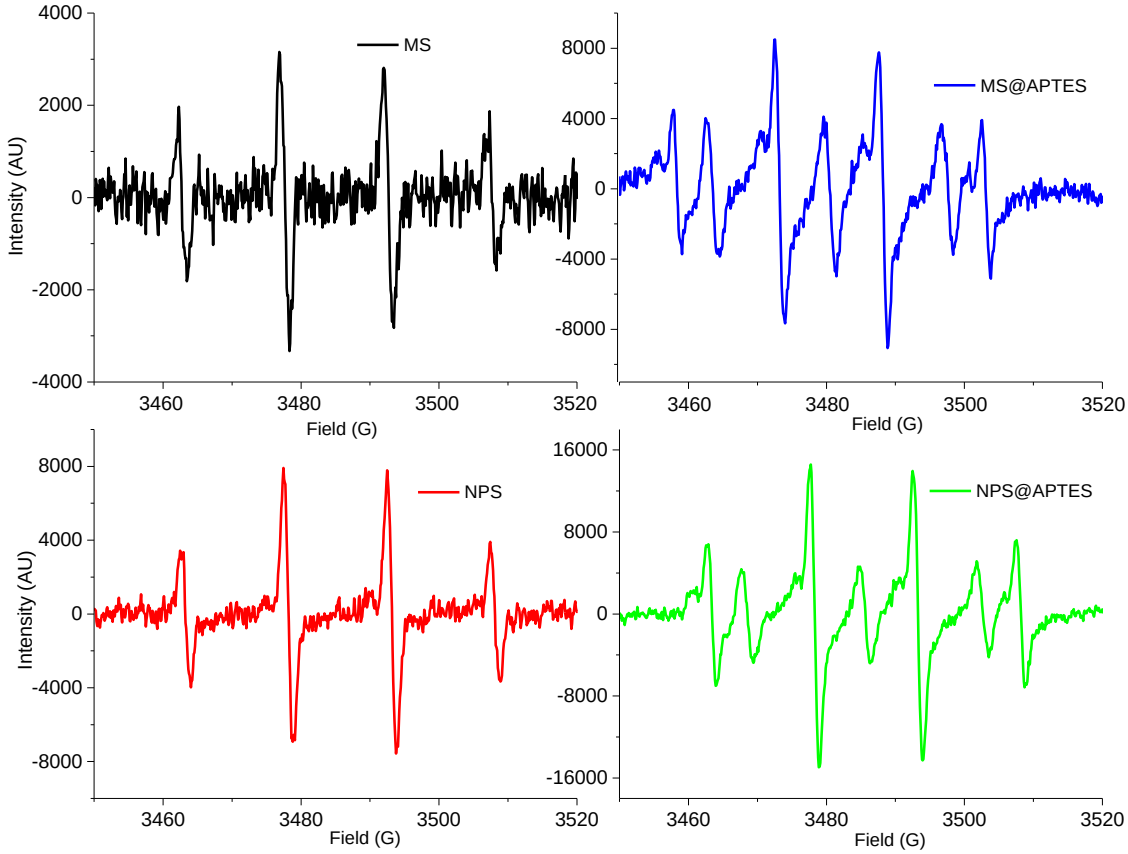

Figure 5.9 EPR spectra of the materials measured in RPMI culture medium. DMPO and H_2O_2 were added to the culture medium and the same methodology was implemented.

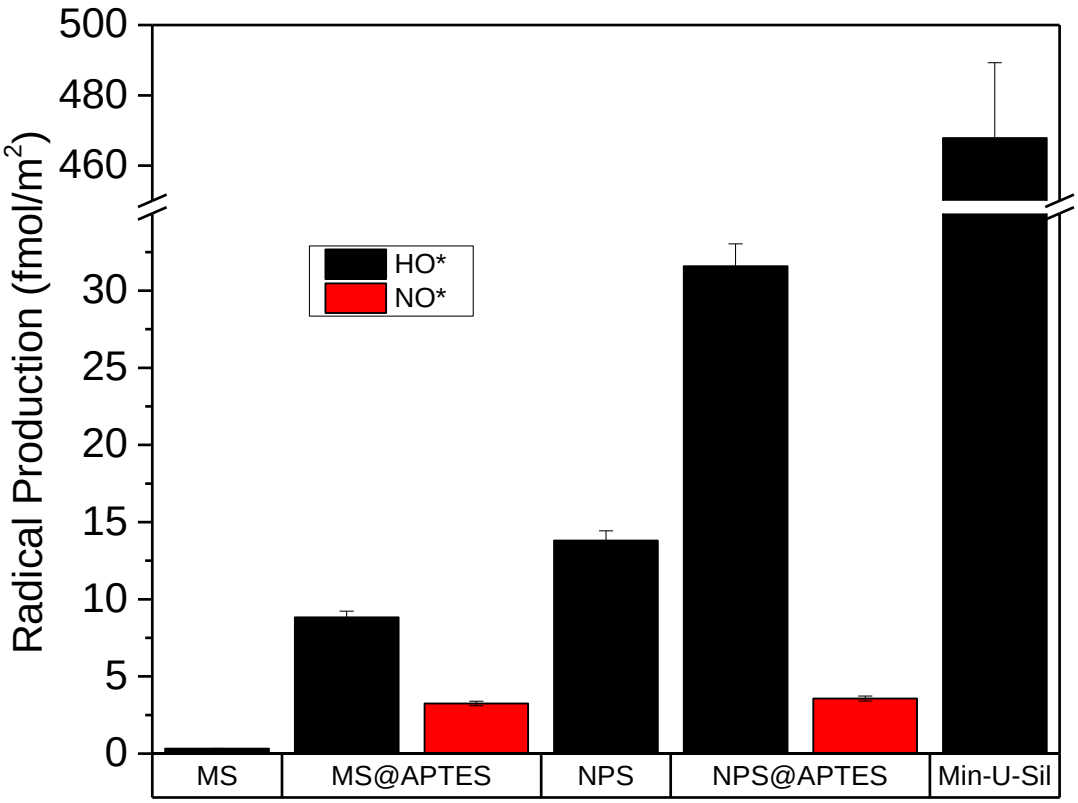

Figure 5.10 Calculated radical production for the EPR experiments conducted in the RPMI culture medium. Note the orders of magnitude decrease; the units of the ordinate are now fmol/m^2 as opposed to pmol/m^2.

5.4.4 *In Vitro* Assessment of ROS Species in RAW 264.7 Cell Line

The EPR spectroscopic measurements, while quantitative and informative, are somewhat limited by the fact that they are carried out in a simplified chemical environment. While it enables extraction and isolation of radical production as a surface catalyzed-process, a toxicological response occurs in the complex chemical environment of the cell. This is why an *in vitro* assay was carried out to quantify intracellular ROS species, using intracellular superoxide ($O_2^{\bullet -}$) concentration as an estimate of total intracellular ROS, and ultimately as a measure of oxidative stress. Cellular metabolic processes, generate ROS as a by-product of ATP production. In the terminal step of the

electron transport chain, cytochrome c oxidase reduces molecular oxygen to water. In a small proportion of these reactions, the oxygen is partially reduced to give the superoxide radical, which reacts to give other ROS species like hydroxyl radical and peroxynitrite ($ONOO^-$). Nature has evolved mechanisms to deal with this source of superoxide radical via the superoxide dismutase family of enzymes which are among the most efficient enzymes known, being diffusion-limited in their catalytic capacity.[104] Immune cells also implement oxidative bursts as a means of destroying foreign pathogens. The key is to extract the increase in intracellular ROS that arises from the nanoparticles rather than endogenous species. The results of this experiment are shown in Figure 5.11.

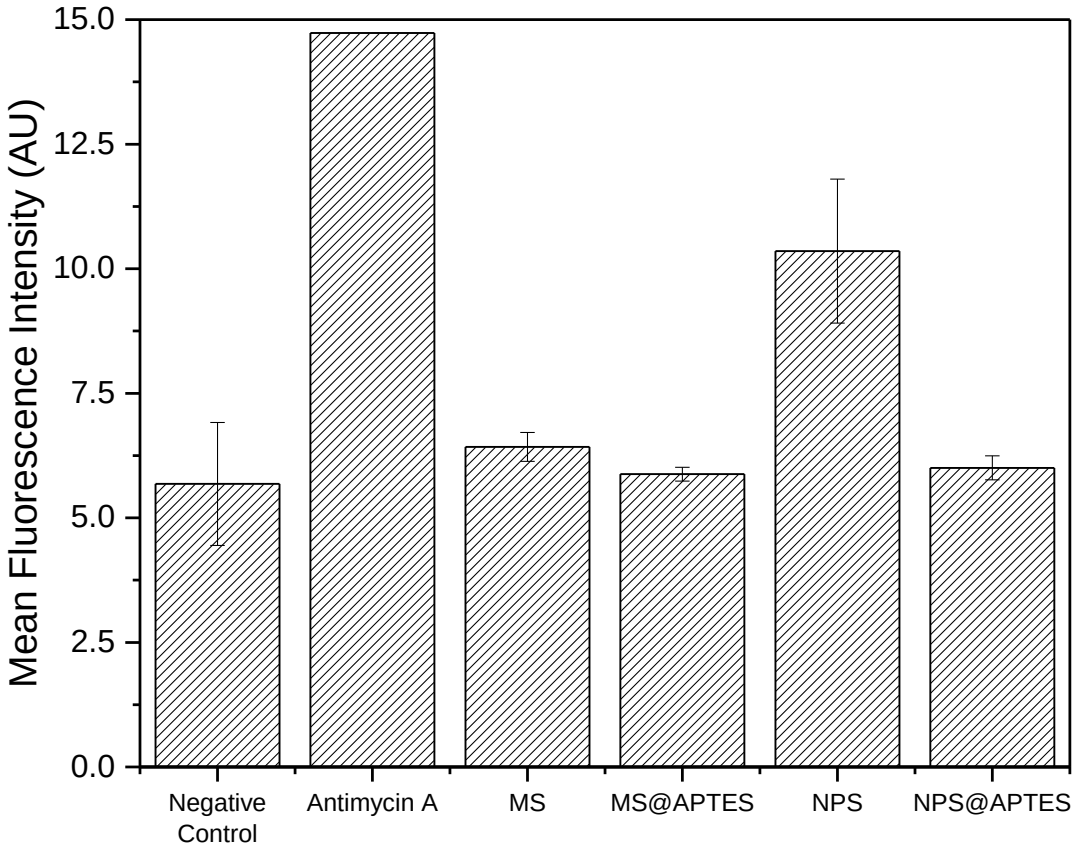

Figure 5.11 *In vitro* ROS assay for each material, negative control, and the antimycin A positive control. The mean fluorescence intensity is proportional to total intracellular ROS. [Data from A. S. Morris.]

The negative control in this case is cells in the absence of nanoparticles, which gives the baseline response of physiological superoxide concentration. Antimycin A served as a positive control, as it inhibits cytochrome c oxidase, uncoupling the electron transport chain and leading to a buildup of intracellular superoxide. The silica nanomaterials, as seen in the data, show very little increase in intracellular ROS, with the exception of the bare nonporous silica material. The nonporous silica nanoparticles seems to induce intracellular formation of ROS in the RAW 264.7 macrophage cells. The other materials show very little elevation in intracellular ROS, which correlates with the cell viability results.

By using particle cell uptake values reported in the literature, and using the calculated radical productions for each material obtained via the EPR measurements, the true intracellular concentration of hydroxyl radical from the mesoporous and nonporous silica nanomaterials can be approximated. Typical values for these size silica nanoparticles give uptake values of around 15,000 particles per cell for the RAW 264.7 cell line.[105] Using this uptake value, the calculated radical production (Figure 5.8), and the typical cellular volume (~ 2 pL), the intracellular concentration of [HO$^{\bullet}$] the bare mesoporous and nonporous materials can be calculated to be approximately 800 and 16000 pM, respectively. Since the concentration of hydrogen peroxide used in the EPR experiments is much higher than a true *in vivo* concentration, this can be used to correct the above concentrations to give realistically expected values (assuming no reaction with other molecules). The values obtained when this correction is employed are 4.2×10^{-16} and 7.9×10^{-15} M [HO•] for the mesoporous and nonporous material, respectively. Compared to the typical *in vivo* concentration (~1×10^{-15} M) this gives a calculated

[HO•]/*in vivo* [HO•] ratio of 0.42 for the mesoporous and 7.9 for the nonporous material.[106]

An elevation of eight times the normal concentration of hydroxyl radical can certainly cause oxidative damage and induce apoptosis. This is especially true if the radicals are generated rapidly, thereby overcoming natural ROS defense mechanisms such as glutathione-mediated redox chemistry.[95] Increased cellular concentrations of ROS results in increased oxidative stress for the cell.[107] We implicate increased intracellular ROS measured here as leading to oxidative stress in the cells. It is well-known from literature that increased oxidative species (i.e. ROS) results in oxidative modifications to biological macromolecules, such as lipid oxidation and protein degradation.[108] Cellular response to this is to initiate signaling cascades that result in apoptosis.[109] Therefore, increased ROS can result in observed cell death via a cascade of biological signaling pathways, which destroy cells damaged by excessive oxidative reactions.

5.4.5 Integration of Cell Viability, EPR Spectroscopy, and Intracellular ROS

Taken together, the data suggests that the elevated toxic response of the bare nonporous silica as understood from the cell viability assay is directly correlated to the high level of intracellular ROS produced upon exposure. This correlates well with the quantitative EPR results, while the other materials show very low cytotoxicity by cell viability as well as low intracellular ROS. In the case of the nonporous silica, the data are strongly suggestive that the observed toxicity can be directly correlated to the ROS produced. The data also strongly suggest that functionalization of nonporous silica reduces its toxicological response by reducing the number of free radicals formed at the surface of the material. This can be attributed to two factors. First, that the number of

surface silanols is reduced due to surface functionalization, through addition of the APTES moiety. The second factor is due to the presence of the functional group sterically blocking the approach of the hydrogen peroxide molecules to the surface-silicon atoms. In the functionalized material, the free molecular motion of the APTES molecule likely restricts the approach of the hydrogen peroxide oxygen, which is required for the surface-catalyzed reaction to occur. Certainly some peroxide molecules will be able to begin the homolytic reaction via the initial rate-determining step (RDS) of the bonding and/or coordination of the peroxide oxygen to the surface silicon. However, the overall rate of this step can be assumed to be much lower in the functionalized material as the APTES moiety hinders the approach of the peroxide molecules, since the APTES is relatively larger in size.

A blank EPR experiment carried out on just a solution of DMPO with added H_2O_2 (in the absence of the nanomaterials) gives a very small signal, which leads to the conclusion that the production of the radicals is surface-catalyzed. Furthermore, other experiments carried out on the nanomaterials in water without H_2O_2 demonstrates no measurable signal of hydroxyl radical. Thus, we suggest that the reaction to generate hydroxyl radical is surface-catalyzed, and that it proceeds without the siloxane ring-breaking mechanism suggested by Zhang, et al. (*vide supra*). There has been some other work in the field investigating free radical production in titania (TiO_2) from cleavage of hydrogen peroxide.[110] The nanoparticle surface thus enhances the rate of homolytic cleavage of the hydrogen peroxide molecule. A proposed mechanism for the homolytic reaction at the silica nanoparticle surface is given in Figure 5.12. The surface sites of the silica are free silanol (Si-OH) moieties. As mentioned previously, silanol moieties are

fairly acidic functional groups ($pK_a \approx 3.0$). At physiological pH (7.4) these groups are uniformly deprotonated to give the silicate anion, possessing negative charge.

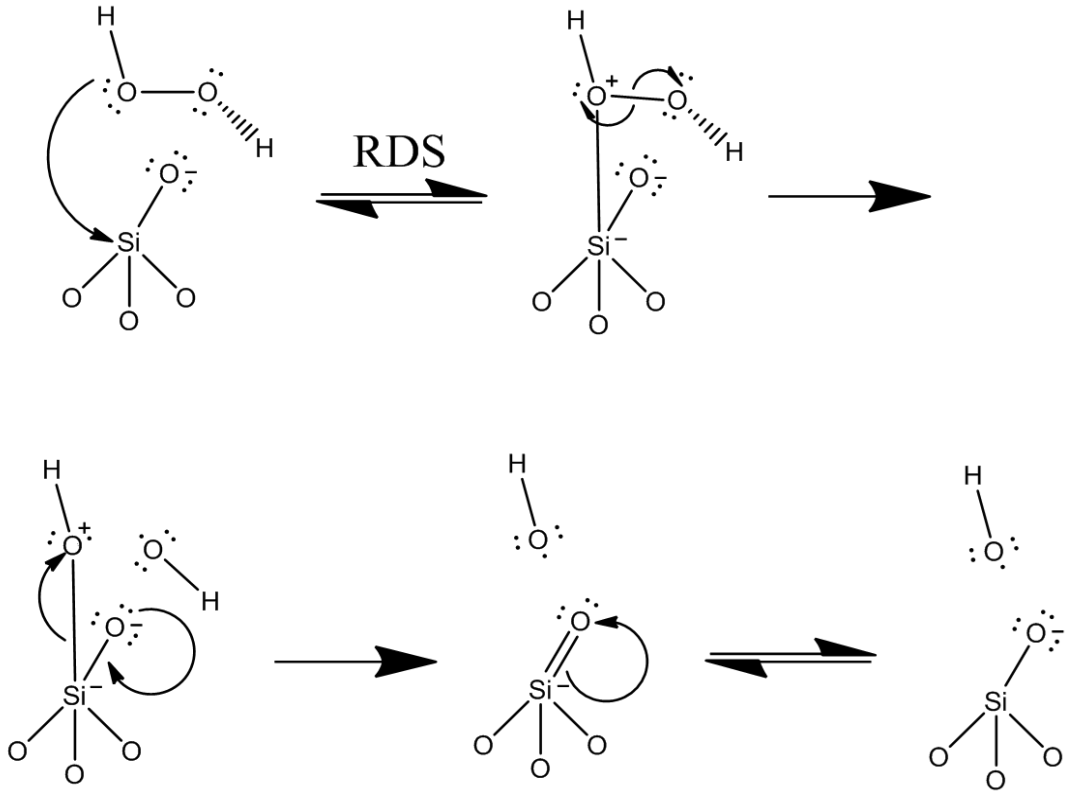

Figure 5.12 Proposed mechanism for homolytic cleavage of H_2O_2 via surface-catalyzed reaction with silica nanoparticle surface. Surface catalysis leads to formation of two hydroxyl radicals ($HO^{\bullet}$). The reaction is initiated by the partial positive charge on the central silicon atom due to the withdrawing effect of the attached oxygen atoms.

Modification of these groups via functionalization can change both the surface charge and the total acidity. In the case of the APTES functionalization utilized in this study, addition of the amine functionality serves to increase the surface charge through the ammonium cation formed at physiological pH; yet the functionalized material is also more basic in nature as some of the silanols have been removed via functionalization and the amine itself is fairly basic ($pK_a = 10.6$). This would produce a more basic solution when compared to the bare materials. It is a well-established phenomenon that hydrogen peroxide is more stable in acidic than basic solutions. Therefore, the EPR data here shows

the opposite trend from the expectation in that the bare nonporous material shows greater degree of the breakdown of H_2O_2 to products (i.e. hydroxyl radical) than the functionalized equivalent. The mechanism proposed here is that surface-coordination of the hydrogen peroxide lowers the activation energy and provides a more stable transition state, enhancing the rate for the homolytic reaction. If this hypothesis is correct, then the predominant mechanism for production of the hydroxyl radical is not in the bulk solvent (which would result from acid- or base-catalyzed homolysis) but is dominated by interactions between the hydrogen peroxide molecules and the silica surface.

In the mesoporous silica, the functionalized material seems to, at least from the EPR measurements, give rise to more free radicals in its functionalized form. This is perhaps due to different coordination of the hydrogen peroxide to the silica surface. It is possible that the amine functionality (which will be positively charged at most pH values) is better able to electrostatically interact with the hydrogen peroxide molecule in the pores of the mesoporous material. In contrast, in the nonporous material, only the external surface is available for bonding. The proposed model (Figure 5.12) idealizes bonding between the peroxide oxygen and the silica silicon atom as an initial step. Overall, more of these atoms are freely accessible in the nonporous silica as they are all at the external surface. Most of the surface area of the mesoporous material is located within the pores themselves.

The hydrodynamic diameter reported in literature for hydrogen peroxide is 0.5 nm which is small enough to fit into the pores of the mesoporous silica (d_{pore} ~3 nm).[111] However, flux through the pores is limited due to the nature of the porous material structure. Molecular flux (J) in one dimension is given by Fick's First Law:

$$J = -D * \frac{\partial C}{\partial x} \quad (25)$$

Here D is the molecular diffusion coefficient in units of m^2/s, C is the concentration and x is distance. This applies to bulk systems but in the case of the inner pores of the mesoporous silica one must employ an effective diffusion coefficient, D_{eff}, which accounts for the flux through the porous network. This can be reasonably approximated by:

$$D_{eff} = \frac{D_{bulk}\delta\varepsilon}{\tau} \quad (26)$$

For this D_{bulk} gives the bulk diffusion coefficient, δ is a constrictivity factor, ε is the porosity, and τ is a tortuosity factor.[112] The bulk diffusion coefficient can be calculated using the Stokes-Einstein relation to be ~9.7×10^{-8} m^2/s. The porosity is the fraction of the total spherical volume occupied by the pores, which for mesoporous silica systems is approximately 60% ($\tau \approx 0.60$). Constrictivity can be approximated as the ratio of the molecular hydrodynamic diameter to the pore diameter ($\delta = 0.16$). The tortuosity factor can be assumed to be 1 (as if it were a material with parallel pores like MCM-41) to give $D_{eff} \approx 9.39 \times 10^{-9}$ m^2/s, which is an order of magnitude smaller than the bulk diffusion coefficient. The tortuosity in this case is larger than one due to the random-walk path of the pores throughout the material due to the less ordered wormhole-type structure in the material used. Therefore the true D_{eff} must be even smaller than the above value.

The system then becomes diffusion-limited as the molecules are forced to undergo flux through the pores to react at the liquid-solid interface. The motion of the molecules is isotropic, so only a concentration gradient drives them through the porous network. This gives rise to decreased mass transport, and perhaps explains why the mesoporous material gives so much lower ROS than that of the nonporous material. The

approximated effective diffusion coefficient described above can account for the sevenfold difference in concentration between the bare porous and nonporous materials. Even though total surface area is larger, the effective surface area "seen" per unit time by the H_2O_2 molecules is much lower in the porous material. In addition, due to the physically constrained nature of the pore diameter, one can envision that the recombination rate of initially formed hydroxyl radicals is much higher than in free solution as their residence time in the total porous network must be much longer than the bulk analogue. The diffusion rate inside the pores ultimately controls the amount radical generated per unit time as almost all (>95%) of the surface area is contained within the porous network. The porosity then has a direct and dramatic effect on the total amount of ROS (hydroxyl radical) generated and thus measured by the EPR spectroscopy described above. This observation supports the working hypothesis of a surface-catalyzed reaction generating free hydroxyls in solution, which is again matched well by the measurement of *in vitro* ROS shown here.

As stated previously, the observation that functionalization of the mesoporous material seems to increase radical production is very puzzling. A possible explanation for the overall increase in radical production for the functionalized mesoporous silica is through a combination of diminished diffusion through the pore and the nature of the functionalized surface. The silica-water interface is an important and often studied area. These studies implicate a Stern layer that shows little change due to the highly hydrophilic surface. This exploration in interfacial water structure and dynamics leads to the presence of an increased viscosity near the interface that manifests as a viscosity gradient.[113] In effect this gives a layer of adsorbed water that only slowly exchanges with

bulk solvent. This could also limit diffusion of the hydrogen peroxide to the surface. If the surface is functionalized, however, one can imagine that the addition of the aminopropyl moieties can disrupt this Stern layer, enhancing flux across the surface. This would then result in an increase in the amount of hydrogen peroxide that is cleaved by interaction with the surface. Furthermore, inside the constrained pores of the mesoporous silica this effect would be further enhanced due to the diminished flux, as described above. Perhaps it is a combination of diminished diffusion and a fairly rigid Stern layer on the silica surface that accounts for these results. However, the source of this effect is unclear at the present time.

5.5 Conclusions

Combined, the data enable a strong correlation between ROS derived from surface-catalyzed reactions and observed cellular toxicity. Porosity has a major effect on the production of ROS from the surface and amine-functionalization in the nonporous material decreases the amount of free radical generated at the solid-liquid interface. We conclude that the mesoporous material shows less toxicity than the nonporous material due to decreased the amount of free radicals generated at the solid-liquid interface; and that this ultimately derives from the total porosity of the material influencing radical production and diffusion to the surface. We invoke a flux-based argument to account for the observed differences, as the surface appears to dictate the radical production. Surface amine-functionalization seems to mitigate radical production by steric hindrance (primarily in the nonporous material) and perhaps also by producing a more rapidly exchanging Stern layer at the interface (in the mesoporous material). Finally, we imply that safety by design can be implemented when the nanomaterials surface effects are considered in synthesis, chemical modification and application.

[The material contained in this chapter was reproduced from Ref. 169 with permission from the Royal Society of Chemistry.]

CHAPTER 6
NANO-BIO INTERACTIONS OF RPMI CULTURE MEDIUM WITH POROUS AND NONPOROUS SILICA OF VARIED SURFACE CHEMISTRY

6.1 Abstract

Understanding complex chemical changes that take place at nano-bio interfaces is of great concern for being able to sustainably implement nanomaterials in key applications such as drug delivery, imaging, and environmental remediation. Typical *in vitro* assays use cell viability as a proxy to understanding nanotoxicity, but often neglect how the nanomaterial surface can be altered by adsorption of solution-phase components in the medium. Protein coronas form on the nanomaterial surfaces when incubated in proteinaceous solutions. Herein, we apply a broad array of techniques to characterize and quantify protein corona formation on silica nanoparticle surfaces. The porosity and surface chemistry of the silica nanoparticles have been systematically varied. Using spectroscopic tools such as FTIR and circular dichroism, structural changes and kinetic processes involved in protein adsorption were evaluated. Additionally, by implementing thermogravimetric analysis, quantitative protein adsorption measurements allowed for the direct comparison between samples. Taken together, these measurements enabled the extraction of useful chemical information on protein binding onto nanoparticles in solution. Overall, we demonstrate that small alkylamines can increase protein adsorption and that even large polymeric molecules such as polyethylene glycol (PEG) cannot prevent protein adsorption in these systems. The implications of these results as they relate to further understanding nano-bio interactions are discussed.

6.2 Introduction

Due to the growth in nanotechnology, the interaction of nanomaterials with biological and environmental systems is an area of great interest. When nanomaterials are

exposed to biological environments, components within the biological matrix modify the nanomaterial surface. These specific interactions between nanomaterials and biological macromolecules have the potential to change how nanomaterials interact with biological systems, such as the immune system. As proteins readily adsorb to surfaces, much effort in the literature has been focused on specifically understanding protein adsorption onto nanomaterial surfaces. In fact, there is a great deal of evidence for the formation of a "protein corona" when a nanomaterial is exposed to a protein-containing solution.[114-116] The protein corona modifies the surface of nanomaterials and changes their modes of interaction with cellular components, as well as their biological and environmental fate.[117] In the complex chemical environment of serum, for example, multiple proteins compete for binding onto nanoparticles. This binding is primarily mediated by protein size and charge.[118-119] Recent work focuses on characterizing the protein corona and its influence on chemical properties.

Other studies have demonstrated that the protein corona forms extremely rapidly, in less than 30 seconds, but changes can take place over longer time scales in the number of adsorbed protein molecules.[120] Conformational changes occur as the protein molecules sample various conformational states, ultimately achieving the lowest energy conformation.[121] Computational studies seek to relate protein corona formation with changes in observed nanomaterial properties.[122] Other computational and experimental work implies that a series of conformational changes occurs as the protein molecules sample various conformational states.[123] In many cases, denaturation occurs as the proteins adsorb to the nanoparticle surface. The literature makes a distinction between "soft" adsorbed proteins, which can still undergo further conformational change, and

"hard" adsorbed proteins that have undergone irreversible conformational changes on the surface.[124] In many cases "hard" proteins are also irreversibly bound to the nanoparticle surface, giving rise to a permanent protein corona that modifies interactions with various other systems.[125]

A recent perspective on this topic by Murphy et al. describes the intrinsically multi-faceted and complex nature of nano-bio interactions.[126] Protein corona formation is now understood to occur at all liquid-solid interfaces in biological systems, but other work finds this not to be the case when the nanomaterial size is very close to that of the protein molecules themselves.[127] Current work is now strongly focused on specific, highly-controlled studies of the nano-bio interface to understand quantitatively what happens when nanomaterials come into contact with biological systems.[128-130] The ultimate goal is to be able to understand and predict changes that will take place when a nanomaterial is exposed to a biological medium such as serum.[131-132] Many chemical processes occur at the interface such as dissolution, aggregation, and generation of chemical species such as free radicals.[133-134] However, at this time, accurate prediction of chemical modifications and ultimately how they affect biological disposition are not yet possible.[126]

Silica nanoparticles are currently under development for a wide variety of applications including corrosion protection, catalysis, and biomedical imaging.[135-137] Silica nanoparticles have widespread applicability in various biomedical, catalytic, and environmental applications due to their attractive physicochemical properties.[138-141] A highly interesting application is as a drug delivery vehicle. This drug delivery vehicle is high feasible due to the properties previously mentioned, and recent literature highlights

outcomes based on these properties.[142] Measuring biocompatibility of silica nanoparticles is critical to evaluate their efficacy in key environmental and biomedical applications.[143] Not only that, but changes in the material structure and surface chemistry via protein corona formation must also be assessed. The amount of work on understanding protein corona formation on silica nanoparticles has grown substantially in recent years. The current understanding is complicated by variation based on size, shape, charge, surface chemistry and other relevant nanomaterial properties. However, some agreement has been reached in terms of the irreversible adsorption of proteins, and therefore the irreversible formation of protein coronas.[144] Furthermore, it has been observed that complex chemical equilibria result in "soft" and "hard" coronas as described above.[145] Recent work by Shahabi, et al. highlights the deeply complex effects of surface chemistry which dictates corona formation and ultimately cellular uptake.[146] Others have described the intrinsically complex phenomena that modify the surface in terms of biological and environmental ligands.[147] As predictive power is still relatively low in these systems, each nanomaterial must be investigated on an individual basis in order to build up a database of generalizable and useful chemical information about this intrinsically interfacial process.

In the complex environment of serum, the quantitative amount of each serological protein on the silica does not directly correlate with their relative abundance in the serum itself.[148] A variety of literature has demonstrated that the exposed solution (and the protein(s) it contains), as well as the nanomaterial size, are of importance in corona formation. In the adsorption of lysozyme onto silica nanoparticles, smaller particles (~20 nm) show only monolayer coverage, whereas larger particles (~100 nm) demonstrate

multilayer surface adsorption.[149] By far the largest component of serum, and in fact most biological media is serum albumin, commonly bovine serum albumin (BSA). As one imagines, many factors impact the structure and kinetics of BSA adsorption onto silica surfaces including pH, concentration, and surface chemistry.[150-152] Due to the complex nature of the adsorption process, however, the materials of interest must be evaluated rigorously and individually, which is the purpose of our study.

The porous and nonporous amorphous silica nanomaterials investigated in this study were systematically varied in their porosity and surface chemistry. These nanomaterials were then fully characterized using traditional physicochemical methods. As a means to more clearly understanding nano-bio interactions, the adsorption of protein molecules from a common cellular culture medium onto a series of size-matched amorphous silica nanoparticles was studied. RPMI (Roswell Park Memorial Institute) culture medium supplemented with fetal bovine serum (FBS) contains a myriad of chemical components that can interact with the nanoparticle surface. It is commonly used as a culture medium for the growth of cells for various assays and analyses. In our study RPMI supplemented with FBS was used in all studies and experiments. The effects of systematically varied porosity and surface chemistry on adsorption of protein from this culture medium were investigated. The materials were also characterized with conventional physical characterization methods. Infrared spectroscopy in the attenuated total reflectance configuration (ATR-FTIR) was used to study adsorption kinetics and thermodynamics. The infrared spectroscopic measurements were complemented with quantitative thermogravimetry, circular dichroism spectroscopy, and zeta potential measurements. This suite of techniques was implemented and integrated to facilitate a

more complete understanding of adsorption of proteins onto the silica nanoparticle surface from RPMI culture medium. The overarching goal of this study was to fully understand the adsorption of culture medium protein onto ~50 nm amorphous silica nanoparticles with systematically varied porosity and surface chemistry.

6.3 Experimental Methods

6.3.1 Silica Nanoparticle Synthesis and Functionalization

Mesoporous silica nanoparticles of WO morphology and nonporous silica utilized for the experiments in this Chapter were synthesized using methods described in Chapter 2 above, Sections 2.2 and 2.3, respectively. The nanoparticles were functionalized with APTES and PEG using the methodology described in Chapter 2, Sections 2.4.1 and 2.4.3, respectively.

6.3.2 Zeta Potential Measurements in Different Media

Zeta potential measurements were conducted on a Malvern ZS Zetasizer DLS/Zeta Potential instrument. A small amount of the material on the order of a few milligrams was incubated in the medium of interest at 4 °C for 48 hours to allow changes in surface chemistry to take place. After this time, the materials were dispersed in the medium of interest by sonication for 30 min immediately prior to measurement. All samples were equilibrated at 25 °C for five minutes before measurements. Measurements were conducted in triplicate, taking the standard deviation as the error.

6.3.3 Quantitative Protein Adsorption by Thermogravimetric Analysis

Protein adsorption was quantified using TGA as well. Samples (~25 mg) were exposed to RMPI culture medium containing FBS for several days at 4 °C to allow adsorption to proceed to completion. The samples were then centrifuged using a tabletop

centrifuge (11000 x*g*) for 30 min to separate them from the solution-phase. The supernatant was removed and the samples were washed three times with water, centrifuging each time, to remove any weakly bound adsorbates. The samples were subjected to thermogravimetry using a 5 °C/min linear heating rate up to 800 °C with pure nitrogen as the purge/flow gas, taking the mass loss from 100-550 °C as the loss of proteinaceous material adsorbed onto the nanomaterial. This was determined experimentally by initial TGA of pure BSA subjected to the same methodology. The proteinaceous samples contain a high amount (up to ~60%) of adsorbed water. The contribution of the adsorbed water was subtracted from the total mass to give an effective "dry" weight for analysis. This was applied to all samples. In the functionalized samples, the mass fraction of each functional group was subtracted to give a weight that only contains a contribution from the adsorbed protein. This was employed for all functionalized samples.

6.3.4 ATR/FTIR Spectroscopy of Protein Adsorption on Nanoparticle Surfaces

Adsorption of growth medium components was assessed using FTIR spectroscopy in the ATR configuration. Silica nanoparticles were deposited (5 mg each) onto a clean ZnSe ATR crystal after dispersion by sonication in 1.00 mL deionized water. Samples were allowed to dry overnight under nitrogen flow and then water was introduced and flowed over the sample for 15 min prior to data collection. A Nicolet FTIR instrument equipped with a liquid nitrogen-cooled MCT detector was used for all data collection. A total of 128 scans were averaged for each spectrum. A water/film spectrum was collected to serve as a blank for spectral correction. RPMI culture medium with 10% (v/v) FBS was then introduced to the sample and spectra were recorded immediately. Data collection

continued for approximately 4 hours at 5 minute intervals to monitor adsorption. After this time the sample was changed to pure water and data collection was immediately restarted for 12 further hours using the same delay to monitor possible desorption of components from the materials. The volumetric flow rate was 800 µL/min for all solutions applied to all samples, and 128 scans were averaged for each spectrum. All experiments were conducted at ambient room temperature. Peak heights were corrected for background drift using a 200 cm^{-1} region from 1800-2000 cm^{-1} where no vibrational peaks appear in the spectra, and plotted as a function of time for kinetic analysis.

6.3.5 Circular Dichroism Spectroscopy

Approximately 2 mg of nanomaterial was incubated in 1.5 mL of RPMI culture medium containing 10% (v/v) FBS at 4 °C for 48 hours to achieve maximum adsorption. After this time, the materials were centrifuged in a tabletop centrifuge at 10,000 RPM for 20 min to sediment the nanomaterials. The RPMI supernatant was removed and replaced with 10 mM sodium phosphate, pH = 7.4 (chloride-free buffer). The materials were washed with the phosphate buffer solution five times, then resuspended in 1.500 mL of phosphate buffer and held at 4 °C for analysis. This was done to give final protein concentrations around 0.2 mg/mL, which is ideal for CD spectroscopy.[153] A Jasco J-815 Circular Dichroism Spectrometer was used to collect CD spectra from 190 to 260 nm, 0.5 nm/step. Immediately before collecting the spectra, each sample was sonicated for 15 minutes then transferred into a 1.00 mm path length quartz cuvette. Five scans were co-added to give a sample spectrum. The instrument was purged with nitrogen gas, and all spectra were collected at 25 °C. Analysis was carried out using the CONTIN algorithm via the online Dichroweb server administered by University of London.[154-155]

6.4 Results and Discussion

6.4.1 Nanomaterial Characterization and Surface Charge

The size of the silica nanoparticles was ~50 nm for the materials used in this study. The porous silica nanoparticles were of the wormhole-type (WO), consisting of an interconnected network of pores that are less ordered than materials such as MCM-41 or SBA-15. The nonporous silica is a solid colloidal material synthesized via base-catalyzed hydrolysis of the silicon source. The surface chemistry was varied via the covalent bonding of aminopropyltriethoxysilane (APTES) or polyethylene glycol (PEG) to the nanoparticle surface. The APTES moiety provides an amino functionality for surface modification and also tends to increase the surface charge. PEG is non-ionic and therefore tends to move the surface towards zero net surface charge. Both moieties increase biocompatibility, and the PEG, in particular, is becoming a popular approach for improving biocompatibility.[156] Six different nanomaterials were evaluated including bare mesoporous and nonporous silica (MS and NPS), and mesoporous and nonporous silica functionalized with APTES or PEG (MS@APTES, MS@PEG, NPS@APTES, NPS@PEG). A representation of the materials is shown in Figure 6.1.

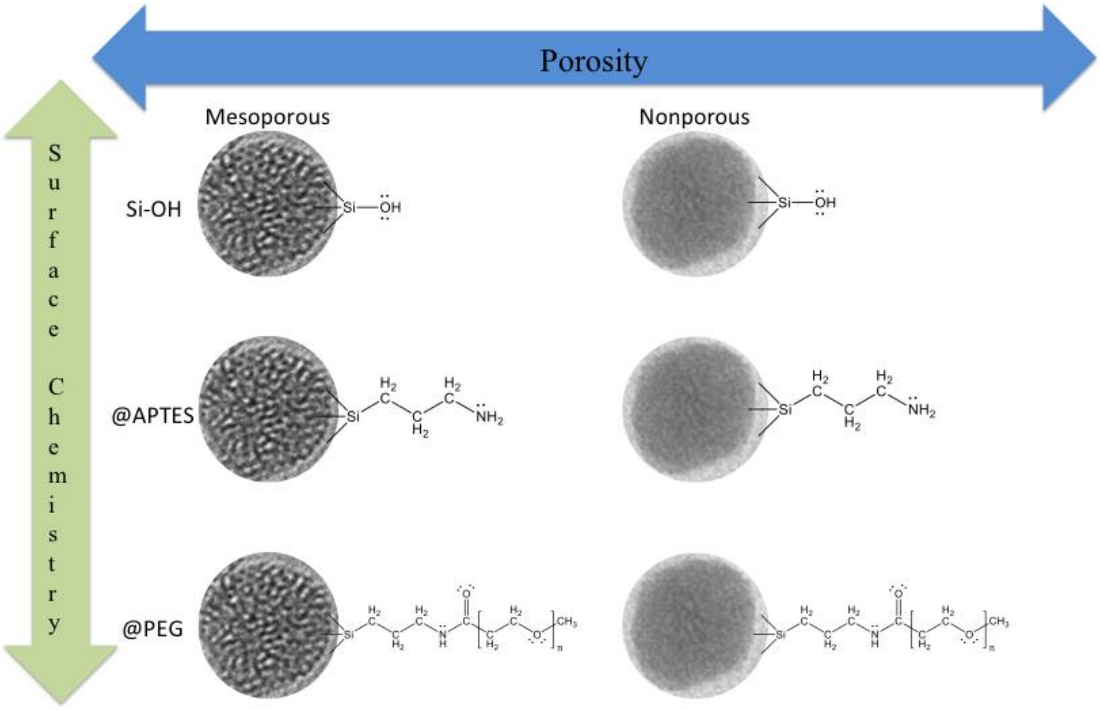

Figure 6.1 Schematic representation of the materials used in this study. The porosity and the surface chemistry variations can be seen in these materials.

Traditional physical characterization methods were employed including transmission electron microscopy, gas adsorption isotherms, and thermogravimetric analysis. The physical characterization data can be seen in Table 6.1 for the materials. Accompanying transmission electron microscopy images can be seen in Figure 6.2.

Table 6.1 Physical Characterization Data for Silica Nanomaterials.

Sample	Size (nm)	Surface Area (m^2/g)	Pore Volume (mL/g)	Pore Diameter (nm)	Functional Group Loading (mmol/g)
Mesoporous Silica (MS)	49 (± 5)	1100 (± 44)	0.562	3.1	N/A
MS@APTES	-	700 (± 28)	0.152	3.1	4.28
MS@PEG	-	250 (± 10)	-	-	0.314
Nonporous Silica (NPS)	47 (± 7)	66 (± 3)	N/A	N/A	N/A
NPS@APTES	-	42 (± 2)	N/A	N/A	0.582
NPS@PEG	-	52 (± 2)	N/A	N/A	0.146

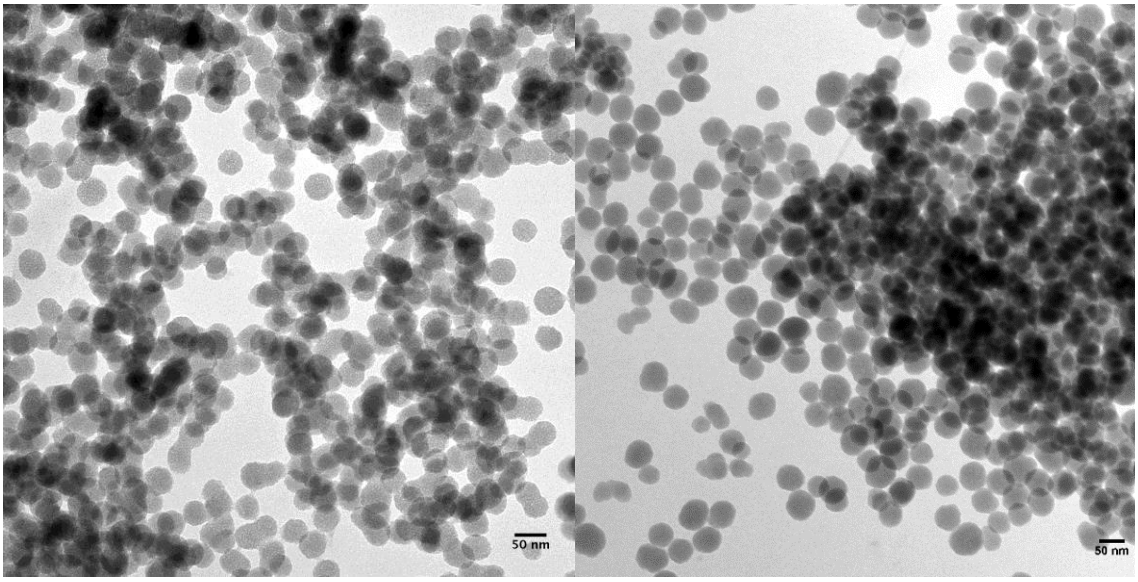

Figure 6.2 Transmission electron microscopy images of the as-synthesized nanomaterials, the mesoporous on the left, and the nonporous on the right. Scale bar is 50 nm in both images.

To confirm the presence and identity of the functional groups on the surface, solid-state NMR was employed. Cross-polarization NMR was used to confirm the identity of the functional group, and the ^{13}C spectra are shown below in Figures 6.3-6.6 for the four functionalized materials. Overall the spectra match well with expected peak positions for

the functional groups. The nonporous silica, however, shows additional peaks from the three expected in its ^{13}C spectrum. These have been assigned to a carbonyl containing impurity, either ethyl acetate or acetamide. The other materials all show the expected peaks at characteristic chemical shift values for each of the materials.

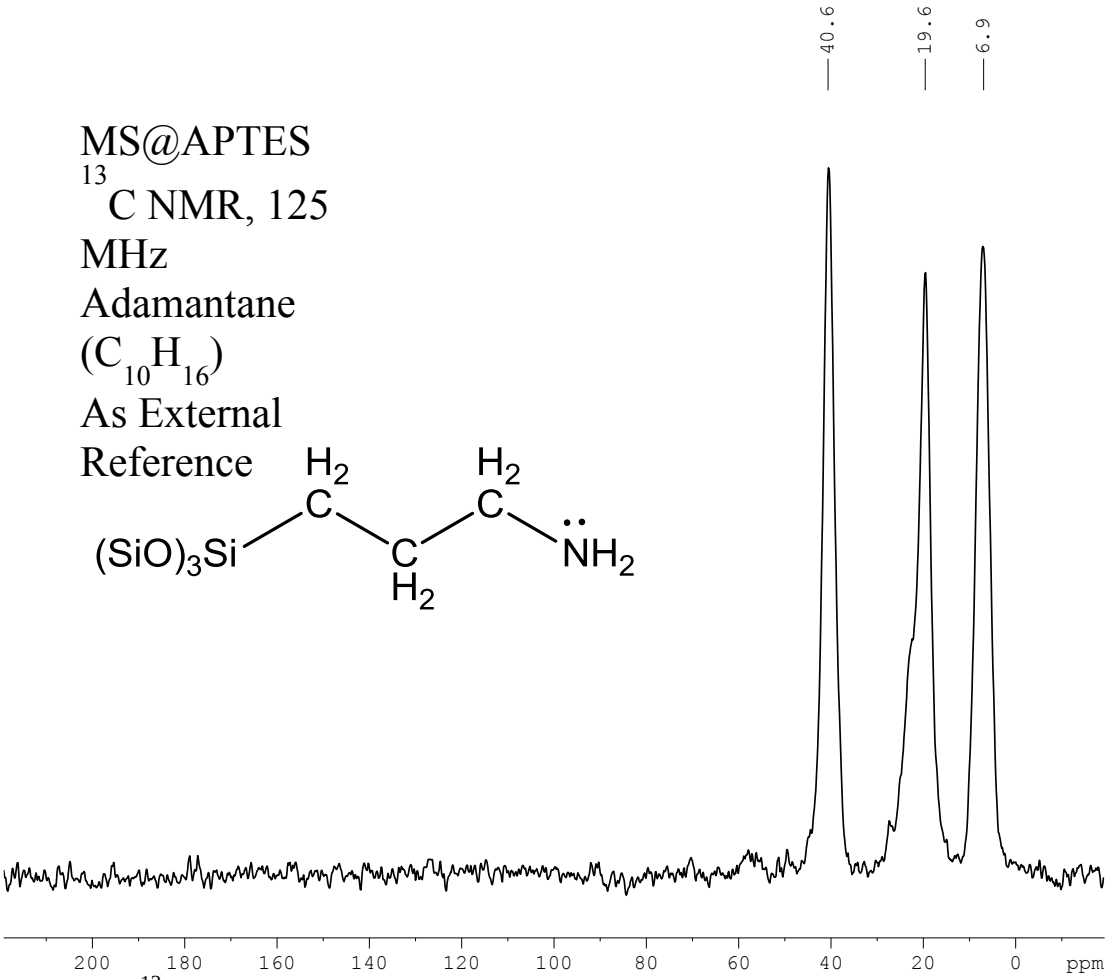

Figure 6.3 ^{13}C CP Solid-State NMR Spectrum of MS@APTES. Structure of surface-bonded APTES moiety is shown. The peaks at 6.9, 19.6, and 40.6 ppm correspond to the Si**C**$H_2CH_2CH_2NH_2$, $SiCH_2$**C**$H_2CH_2NH_2$, and $SiCH_2CH_2$**C**H_2NH_2 carbon atoms, respectively.

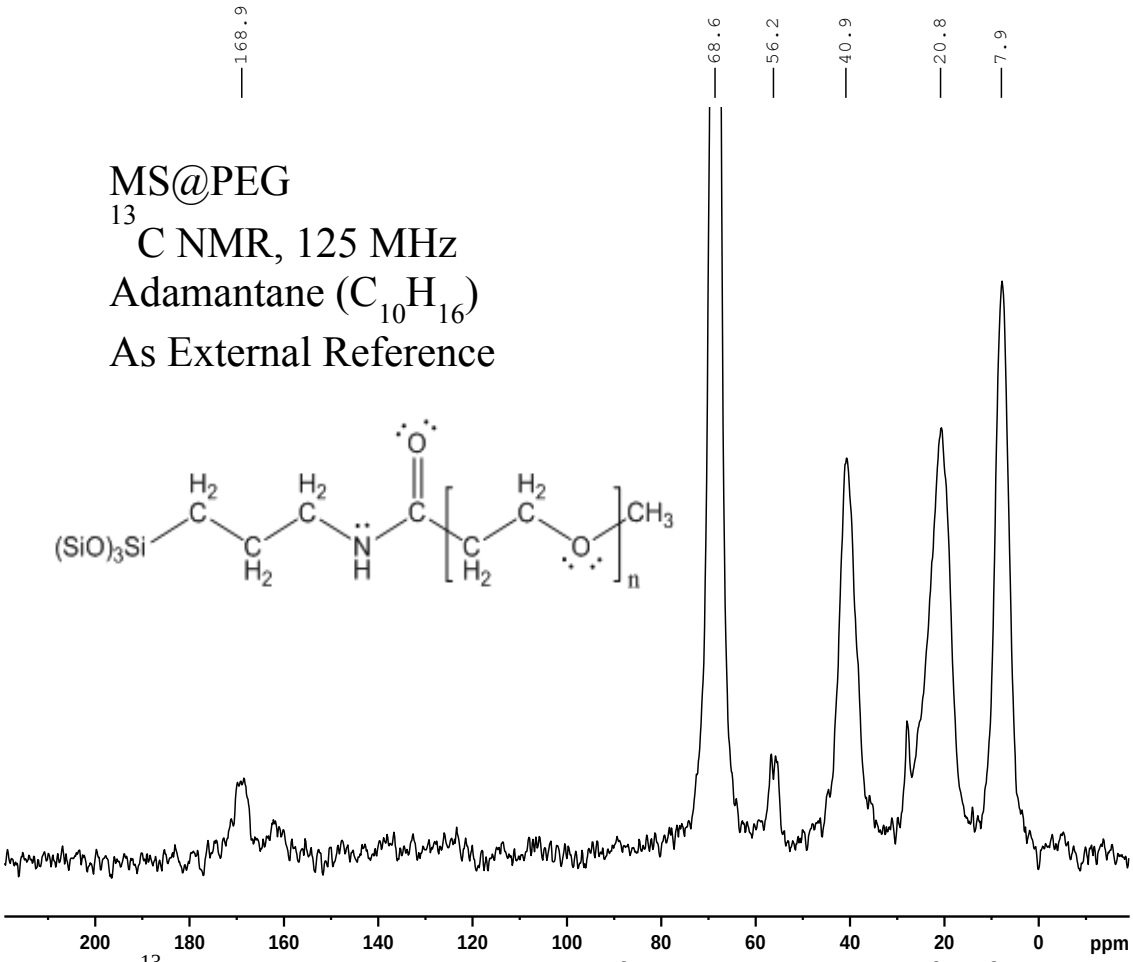

Figure 6.4 ^{13}C CP Solid-State NMR Spectrum of MS@PEG. Structure of surface-bonded PEG-APTES moiety is shown. The peaks at 7.4, 20.8, and 40.9 ppm correspond to the Si**C**$H_2CH_2CH_2NH_2$, $SiCH_2$**C**$H_2CH_2NH_2$, and $SiCH_2CH_2$**C**H_2NH_2 carbon atoms of the APTES moiety, respectively. The peaks at 56.2, 68.6, and 168. 9 ppm correspond to the H_3**C**$[OCH_2CH_2]_nCON$, $H_3C[O$**C**H_2**C**$H_2]_nCON$, $H_3C[OCH_2CH_2]_n$**C**ON carbon atoms of the PEG moiety, respectively.

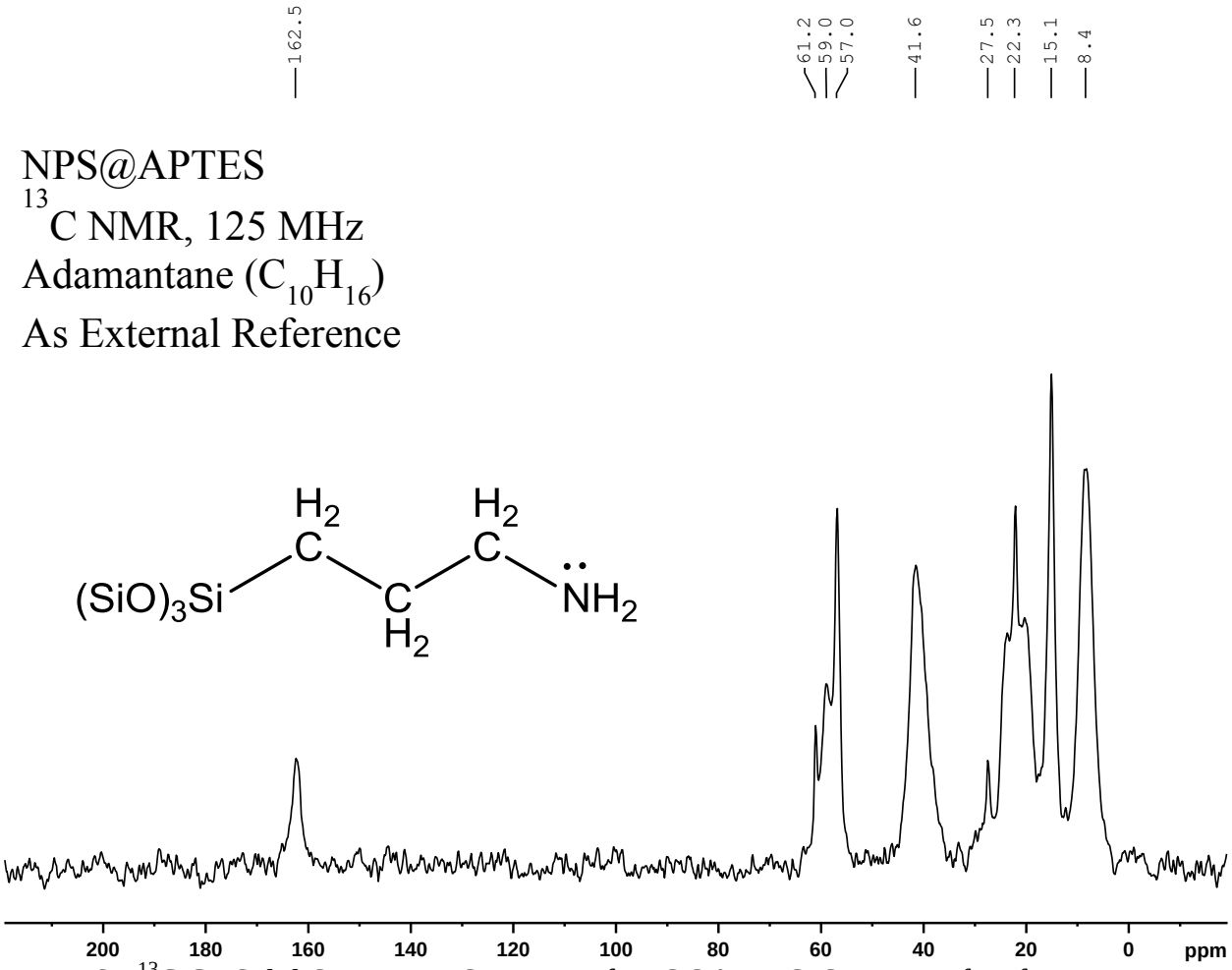

Figure 6.5 ^{13}C CP Solid-State NMR Spectrum of NPS@APTES. Structure of surface-bonded APTES moiety is shown. The peaks at 8.4, 22.2, and 41.6 ppm correspond to the Si**C**$H_2CH_2CH_2NH_2$, $SiCH_2$**C**$H_2CH_2NH_2$, and $SiCH_2CH_2$**C**H_2NH_2 carbon atoms, respectively. The remaining peaks in the spectrum are assigned to a carbonyl-containing impurity, either ethyl acetate or acetamide.

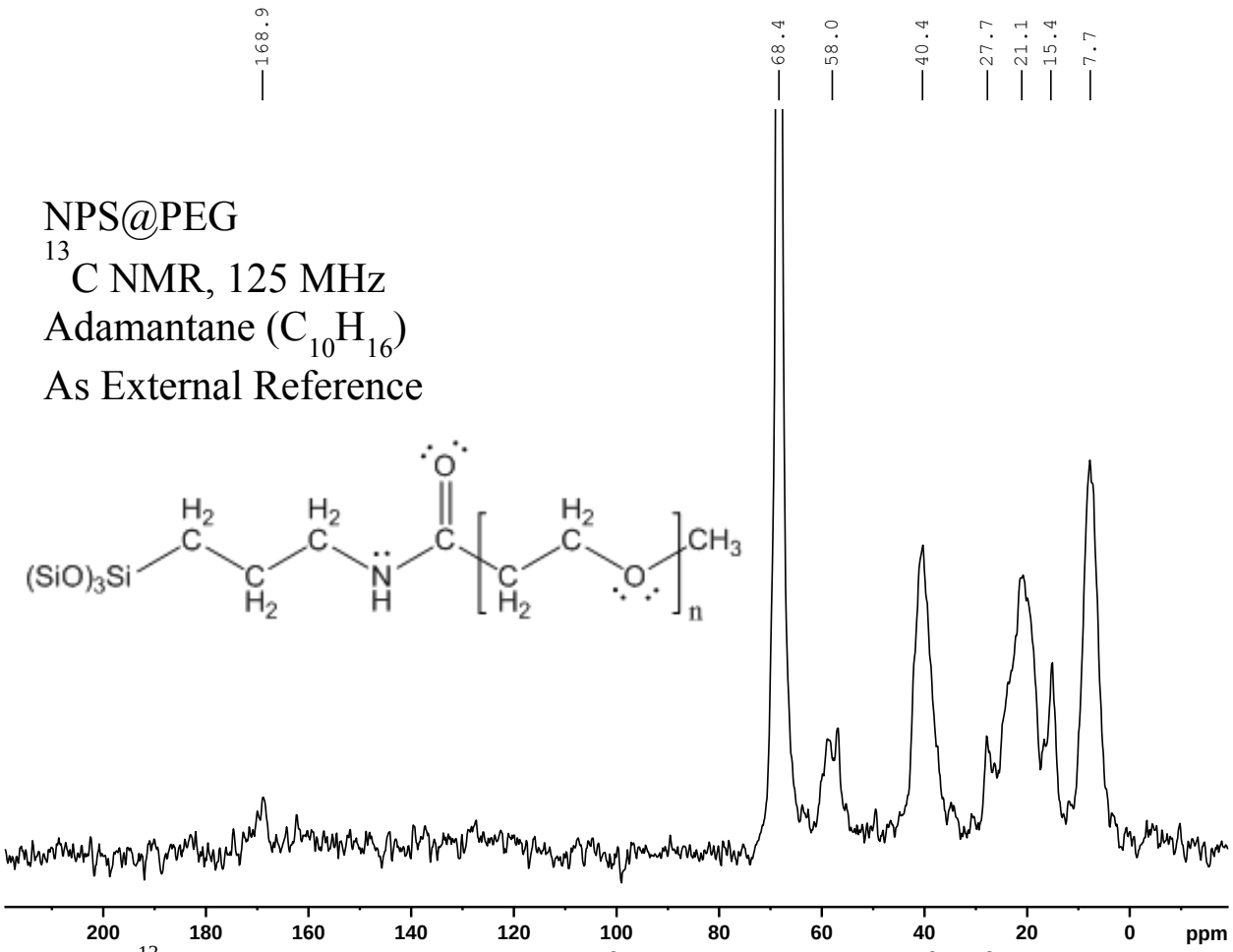

Figure 6.6 ^{13}C CP Solid-State NMR Spectrum of NPS@PEG. Structure of surface-bonded PEG-APTES moiety is shown. The peaks at 7.7, 21.1, and 40.4 ppm correspond to the Si**C**$H_2CH_2CH_2NH_2$, $SiCH_2$**C**$H_2CH_2NH_2$, and $SiCH_2CH_2$**C**H_2NH_2 carbon atoms of the APTES moiety, respectively. The peaks at 58.0, 68.4, and 168.9 ppm correspond to the H_3**C**$[OCH_2CH_2]_nCON$, $H_3C[O$**C**H_2**C**$H_2]_nCON$, $H_3C[OCH_2CH_2]_n$**C**ON carbon atoms of the PEG moiety, respectively.

In order to quantify and detect changes in the surface charge, zeta potential measurements were collected for all materials under different solution conditions (Figure 6.7).

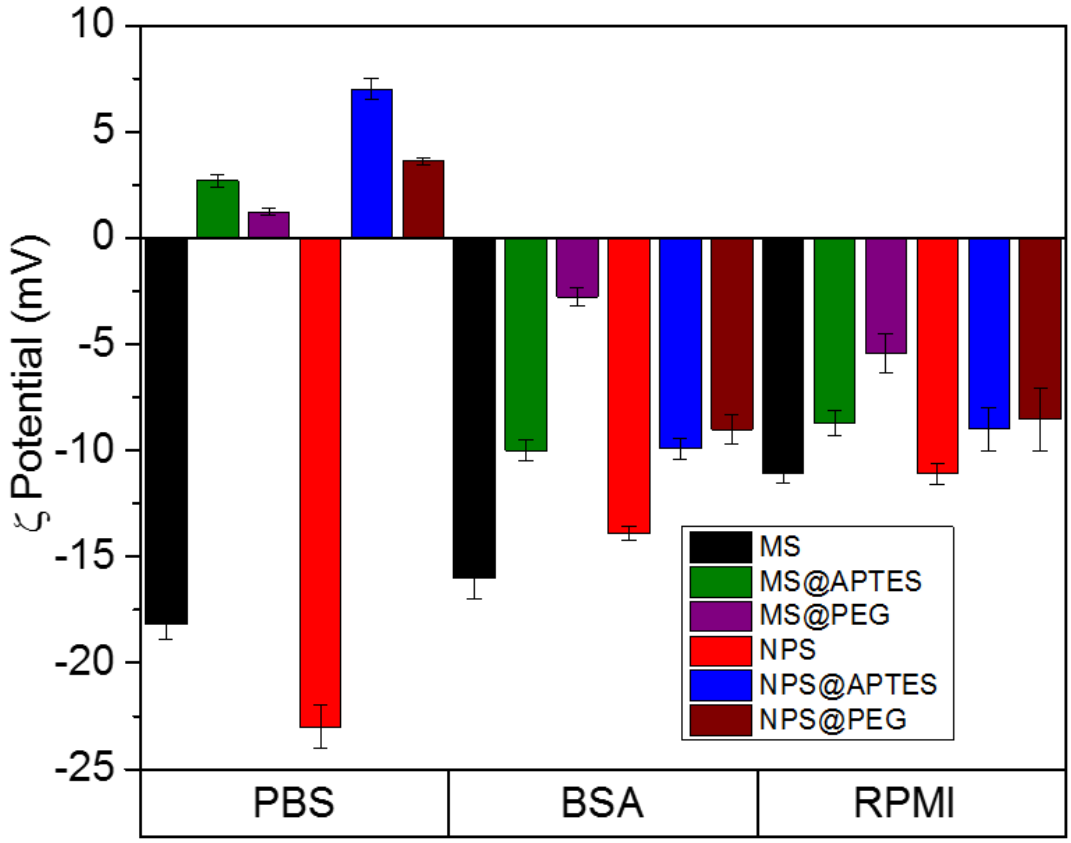

Figure 6.7 Zeta potential data of the nanomaterials in different media. The samples were incubated and then measured in the indicated media, all at pH = 7.4.

All solutions were at pH 7.4 to mimic physiological conditions, which is also the solution pH of RPMI culture medium. The first solution is phosphate-buffered saline (PBS), which is a typical solution to mimic physiological pH and ionic strength conditions. The results are as expected, with the bare nanomaterials in PBS showing negative zeta potentials, indicative of deprotonated silanols (as silicate anion) on the surface. The APTES-functionalized material demonstrates positive zeta potential due to the functionalization process; functionalization modifies free silanols to add a covalently-

bonded propylamine moiety, which is positively charged at pH 7.4. This tends to shift the zeta potential to a more positive value. The PEG moiety also leads to a more positive value in the zeta potential, but not as strongly as the APTES moiety as it chemically converts silanols to a non-ionic functionality.

In the RPMI culture medium, the zeta potential of all the materials in this study becomes very similar, ~-5 to -10 mV. Overall, serum albumin is negatively charged at physiological pH, and so this observation can be interpreted to mean that differing amounts of albumin from the RPMI medium have adsorbed onto the material surface. A qualitative check of this is given by the BSA (prepared in PBS) sample, which contained bovine serum albumin at the same concentration as that of the RPMI culture medium (~40 μM). This result is very similar to that of the RPMI, suggesting that the bovine serum albumin is the primary modulator of surface charge in this system. This finding suggests that upon adsorption of serum albumin protein, the adsorbed serum albumin molecules have negated the initial surface charge of the material present prior to exposure and adsorption.

Further explorations of the surface charge were carried out by incubating the samples in a medium of interest, then washing and transferring them to another solution for measurement. The results of this experiment can be seen in Figure 6.8. Here, the two experiments were incubated in RPMI, then transferred to either PBS or pure water. The first sample transferred to PBS looks altogether not too different from the RPMI sample above in Figure 6.7. Here, the change can be attributed to the removal of any associated molecules that are near the surface in the RPMI, but are washed away by PBS. The second case of the sample washed in and transferred to water looks very different. This

dramatic shift in the zeta potential is likely due to the low ionic strength environment of the water, which would disrupt any salt bridges in bound protein molecules on the surface.

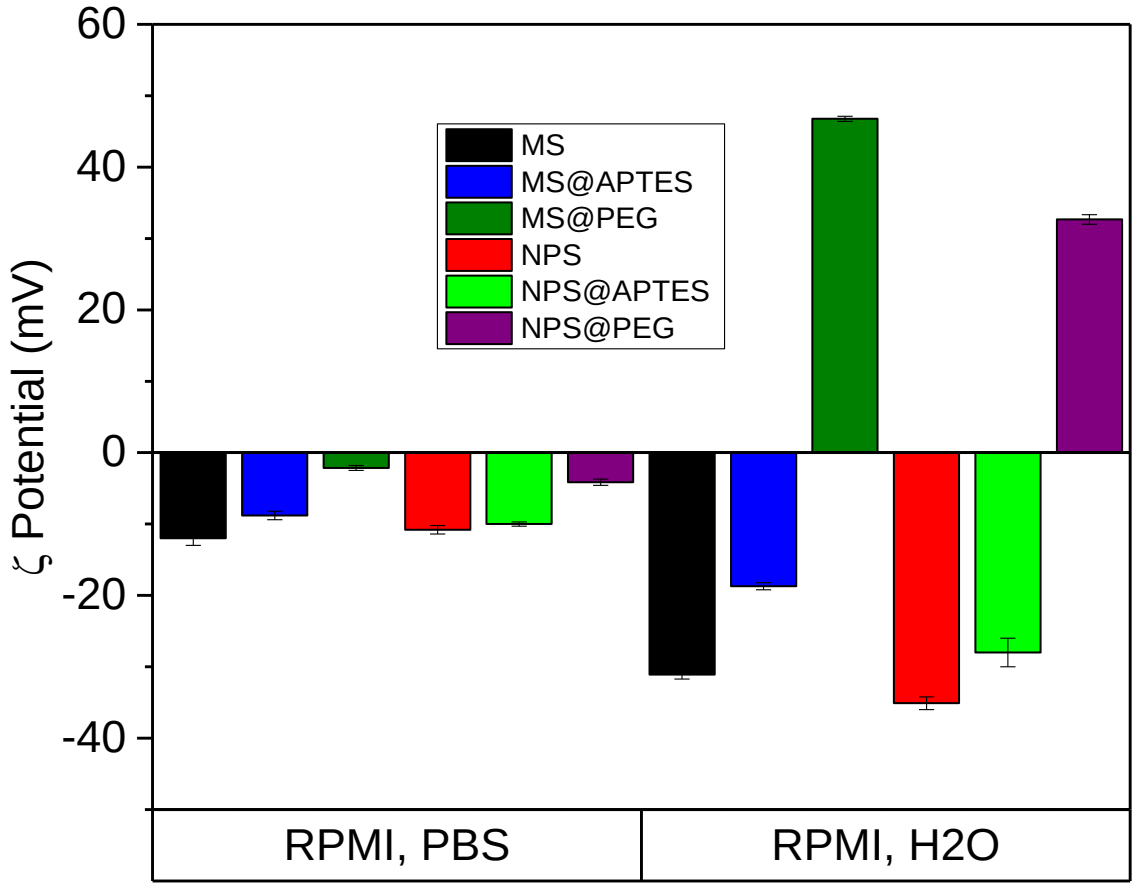

Figure 6.8 Zeta potential measurements in different media. The (x,y) notation describes how the sample was incubated in solution x, then washed in and transferred to solution y for zeta potential measurement.

6.4.2 Attenuated Total Reflectance-Fourier Transform Infrared Spectroscopy

In order to characterize the adsorption of the components of the RPMI culture medium, ATR-FTIR spectroscopy was carried out to monitor and quantitatively observe adsorption processes. Nanomaterials were deposited onto a ZnSe ATR element and allowed to dry. RPMI solution was introduced in the ATR-FTIR system through a flow system. After subtraction of the water contribution from the spectrum, the adsorption of

other solution-phase components can then be monitored spectroscopically. This methodology was applied to all of the materials. An initial spectrum of just the thin film of the WO-type mesoporous silica on the ZnSe element is shown in Figure 6.9 below. Here, the framework vibrations of the particles are shown around 1000 cm^{-1} in the data.

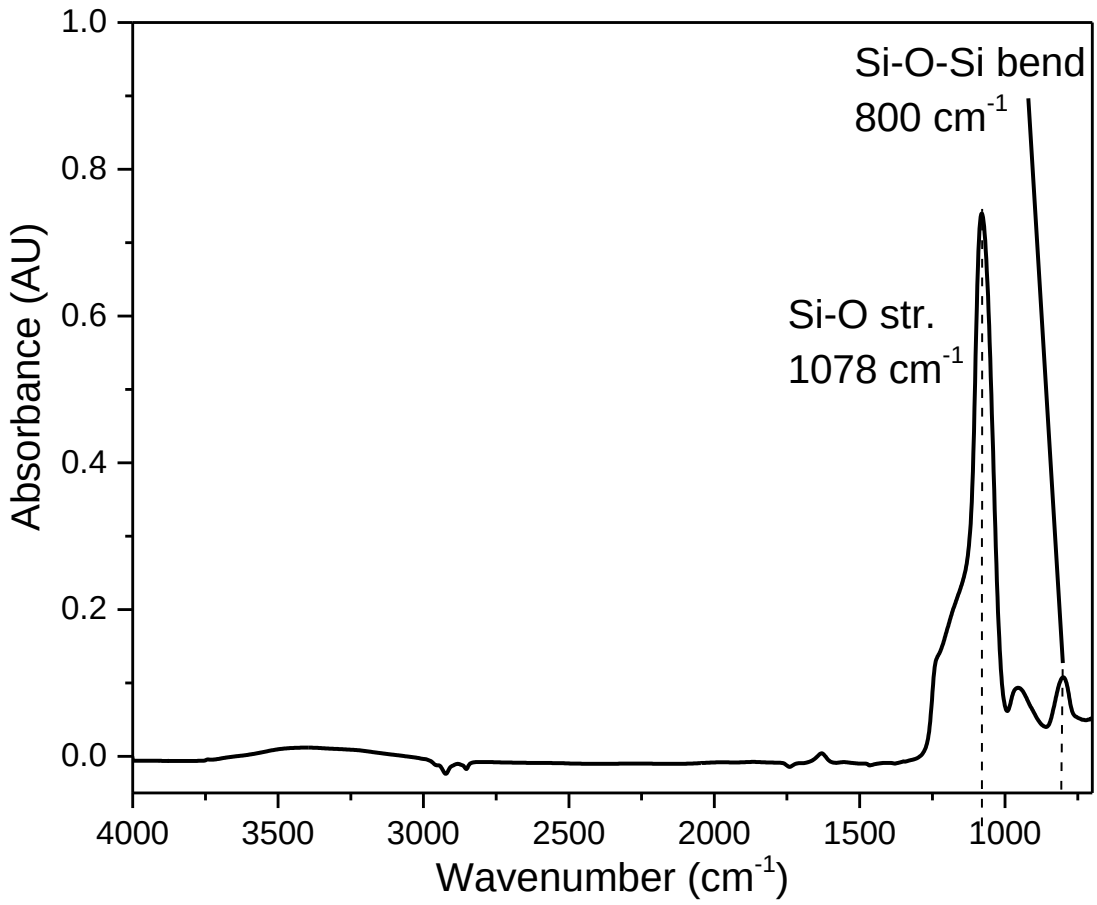

Figure 6.9 ATR-FTIR spectrum of the WO-type mesoporous silica on the ZnSe crystal. Peaks corresponding to the mesoporous silica framework are assigned.

Across the mid-IR range, signals appearing around 1600 cm^{-1} were indicative of surface-bound species. These peaks (see Figure 6.10) have been assigned to the Amide I and Amide II peaks of adsorbed protein molecules. The RPMI culture medium contains over 50 components, and the added fetal bovine serum adds many more.[157] While RPMI medium does contain a variety of amino acids, they are all in their free form. Free amino

acids do not possess an amide moiety, and thus would not be expected to give peaks in the amide region. Therefore, we assume that the observed signals come only from serum proteins, primarily BSA. The Amide I peak primarily arises from the carbonyl C=O stretching motion, whereas the Amide II peak primarily occurs due to the N-H bending motion. However, the motions are coupled to each other, and so the vibrational modes are more complex than the isolated fundamental vibrations.

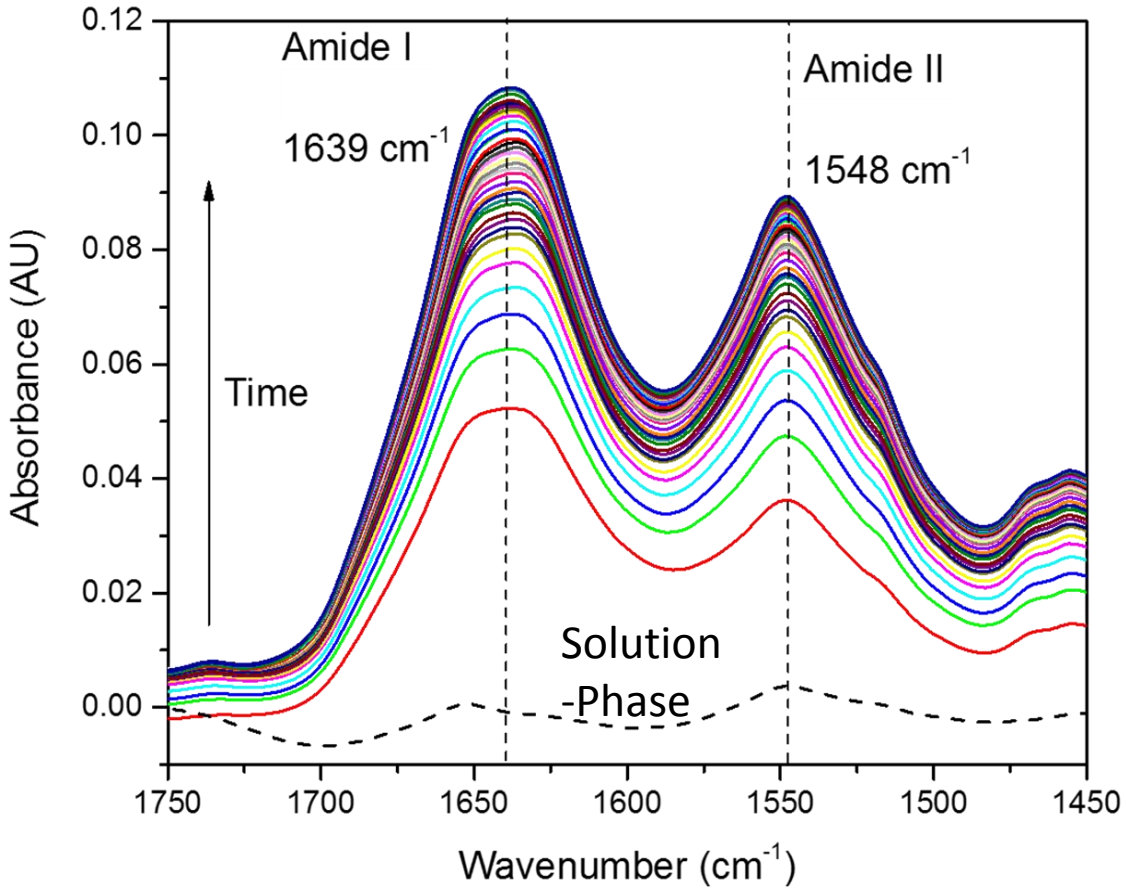

Figure 6.10 ATR-FTIR adsorption of protein from RPMI culture medium onto the mesoporous silica material collected as a function of time at a constant volumetric flow rate. The solution-phase spectrum of the RPMI is given by the dotted line near the bottom. Based on this, the solution-phase does not significantly contribute to the signal.

From the ATR-FTIR, the kinetics can be measured and rate constants for the adsorption process extracted. When the peak height is corrected for the background drift

and then plotted as a function of time, a classic kinetic curve takes shape (Figure 6.11). The Amide II peak (at ~ 1548 cm^{-1}) was selected for this analysis, as the Amide I peak is highly sensitive to the secondary structure of the protein, whereas the Amide II peak is not. Furthermore, the Amide I peak is at the same frequency as the water-bending mode near 1640 cm^{-1}. Although we subtract the water-bending mode contribution from the spectra, the Amide II peak is best used for kinetic analysis.

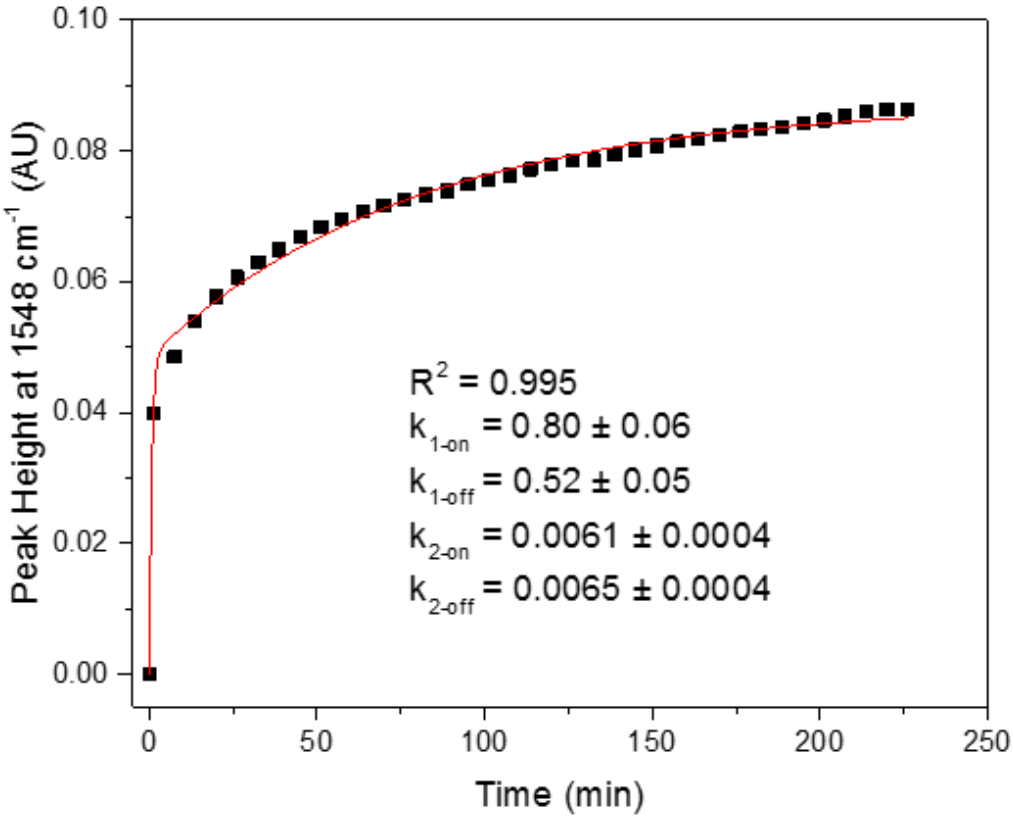

Figure 6.11 Kinetic analysis of the adsorption of RPMI culture medium protein onto the bare wormhole-type silica. The peak heights have been background corrected using a 200 cm^{-1} region from 1800-2000 cm^{-1} to give a corrected peak height, plotted above.

There are a multitude of models for these adsorptive processes. A recent review by Mudunkotuwa, et al. provides a framework for the fitting and analysis of this type of kinetic data.[158] The data presented in Figure 4 has been subjected to a bi-exponential expression corresponding to a two-site model, which can be given in full mathematical

form as the following:

$$A(t) = \frac{A_{max}k'_{1-on}(1-e^{-\left(k'_{1-on}+k'_{1-off}\right)*t}}{(k'_{1-on}+k'_{1-off})} + \frac{A_{max}k'_{2-on}(1-e^{-\left(k'_{2-on}+k'_{2-off}\right)*t}}{(k'_{2-on}+k'_{2-off})} \qquad (27)$$

A(t) is the measured absorbance at time t, A_{max} is the approached maximum value for the absorbance as it reaches saturation, and $k'_{1-on}, k'_{1-off}, k'_{2-on},$ and k'_{2-off} represent the forward and reverse rate constants for the first and second binding steps, respectively. The tick (′) represents that these are the apparent first-order rate constants obtained from the curve fit. As the process is an equilibrium process, there are both forward and reverse rate constants for the equilibration step, which can be written in a fundamental way:

$$P_{(aq)} \underset{k_{off}}{\overset{k_{on}}{\rightleftharpoons}} P_{(a)}$$

This describes how a protein molecule (P) can go from the aqueous (aq) phase into the adsorbed state (a) in the equilibrium process governed by the forward and reverse rate constants. Since the data were fit to a two-site model, this equilibration occurs twice. This follows logically when one considers the surface silanols to be the binding sites when compared to the significantly larger protein molecule. One can imagine that the protein molecule initially interacts with the surface via one silanol as it interacts with the outer exposed protein surface. This is the initial step, which is probably the rate-limiting step; upon which the second binding step can occur giving rise to a protein molecule that becomes adsorbed on the nanoparticle surface. We revisit this binding later in our discussion of thermodynamic considerations.

In the ATR experiments, the adsorption was performed in the RPMI culture medium with FBS added. To determine any losses, pure water at the same pH was used

to facilitate desorption from the nanoparticle surface. The total experimental data for the bare WO silica sample is given in Figure 6.12. The color marking denotes where the experiment was under adsorption conditions and when it was under desorption conditions. As can be seen, the change to the water causes a small change in signal. Overall this is indicative of irreversible adsorption to the surface. The loss of signal most probably arises from the removal of weakly-bound molecules that are associated with the proteinaceous coating on the nanoparticle surface at the liquid-solid interface. These molecules are likely only weakly electrostatically interacting with exposed domains of the protein and are thus washed away by the influx of water during the desorption step.

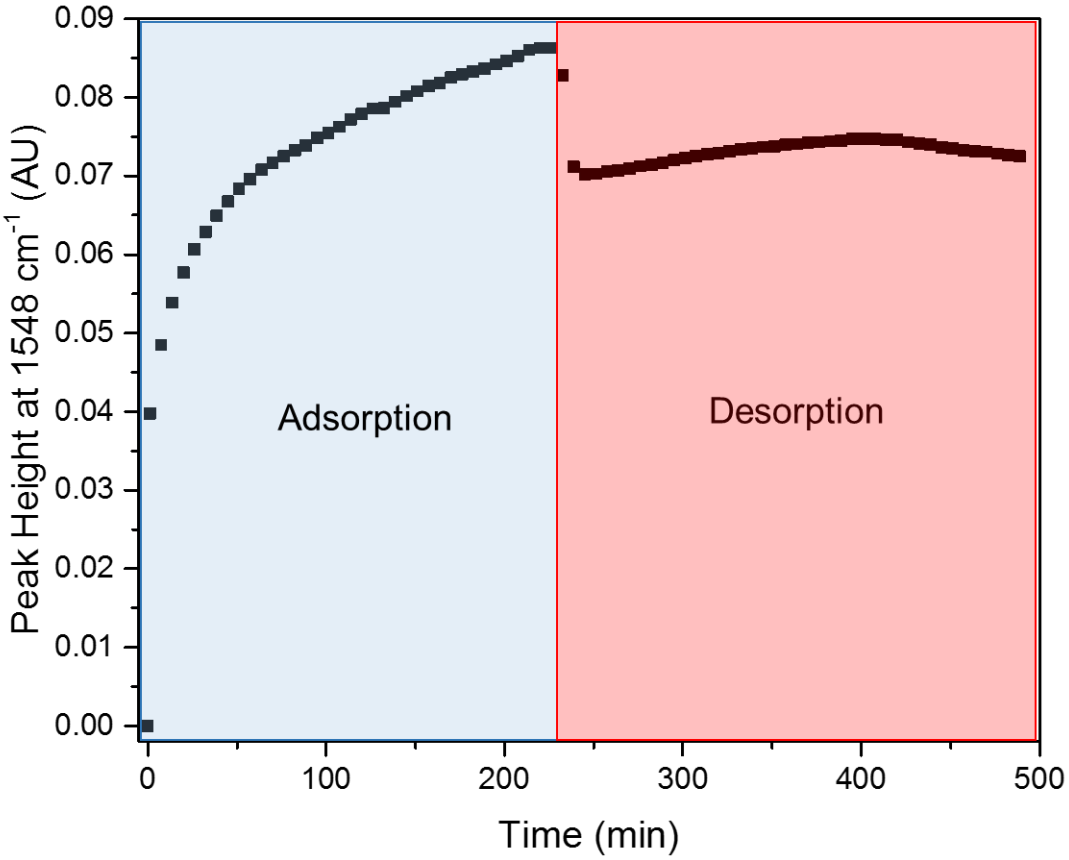

Figure 6.12 Total experimental ATR/FTIR data for the WO-type silica sample. The blue panel represents the adsorption of proteinaceous components from the RPMI culture medium. The red panel represents a change from RPMI to water to promote desorption of bound molecules. The small loss of signal is indicative of irreversible adsorption onto the nanomaterial surface.

The rate constants calculated for the two-site kinetic fit for all of the silica nanoparticle samples are shown in Table 6.2. The same model was applied to all of the samples, as a simple one-site model does not correctly fit to the measured kinetic curves. Desorption data for all of the materials are similar to that shown in Figure 6.12. Since this indicates irreversible adsorption, desorption data were not fit to a kinetic model as it was not indicated to take place for the observed adsorbed protein. Therefore, only adsorption rate constants are reported here, matching with the two-site equilibration model described above.

Table 6.2 Summary of Rate Constants Derived from Kinetic Fits of ATR-FTIR Data.

Sample	k'_{1-on} (min^{-1})	k'_{1-off} (min^{-1})	k'_{2-on} (min^{-1})	k'_{2-off} (min^{-1})	R^2 from fit
Mesoporous Silica (MS)	0.80 ± 0.06	0.52 ± 0.05	0.0061 ± 0.0004	0.0065 ± 0.0004	0.995
MS@APTES	0.88 ± 0.03	0.23 ± 0.02	0.0068 ± 0.0007	0.022 ± 0.001	0.997
MS@PEG	0.61 ± 0.02	0.37 ± 0.02	0.0057 ± 0.0004	0.013 ± 0.007	0.998
Nonporous Silica (NPS)	0.48 ± 0.02	0.37 ± 0.03	0.0080 ± 0.0005	0.0090 ± 0.0005	0.998
NPS@APTES	0.46 ± 0.02	0.38 ± 0.03	0.0097 ± 0.0006	0.0115 ± 0.0006	0.998
NPS@PEG	0.56 ± 0.06	0.26 ± 0.04	0.0039 ± 0.0004	0.009 ± 0.002	0.975

6.4.3 Thermodynamics of Protein Adsorption

Due to the fundamental relation between kinetic and thermodynamic quantities, the observed rate constants from the ATR/FTIR spectroscopic measurements can be used to derive thermodynamic parameters for the nanoparticle-protein chemical system. The equilibrium constant for the adsorption process as written above in Equation 1 can be given by:

$$K_{ads} = \frac{k'_{on}}{k'_{off}*[L]_0} \quad (28)$$

In this calculation, the on and off rate constants are those derived from the kinetic analysis given in Figure 6.10. The equilibrium constant depends also on the total initial ligand concentration $[L]_0$. In the case of RPMI culture medium containing 10% FBS the total BSA concentration is 40 μM. In the case of the bare wormhole-type silica, employing this calculation gives equilibrium constants of 35,000 and 17,600 for the first and second binding steps, respectively. This is not surprising considering other work in the field which has experimentally verified the thermodynamically favorable adsorption

of proteins from solution.[159]

From the equilibrium constants, binding free energies can be calculated via:

$$\Delta G = -RT \ln K_{ads} \quad (29)$$

Since these experiments were conducted at room temperature, T = 298 K, and R takes the usual value of 8.314 J*mol^{-1}*K^{-1}. From the measured adsorption equilibrium constants for the wormhole-type system, the free energies are determined to be -25.9 and -24.2 kJ/mol for the first and second binding step, respectively. The thermodynamic data calculated for all six samples is given in 6.3.

Table 6.3 Summary of Thermodynamic Parameters Derived from ATR-FTIR Data.

Sample	Binding Step	K_{ads} (AU)	ΔG (kJ/mol)
MS	1 (2)	35300 (17600)	-25.9 (-24.2)
MS@APTES	1 (2)	93800 (7500)	-28.4 (-22.1)
MS@PEG	1 (2)	40600 (10700)	-26.3 (-23.0)
NPS	1 (2)	31900 (21900)	-25.7 (-24.8)
NPS@APTES	1 (2)	29800 (20700)	-25.5 (-24.6)

Several key findings come from these data. First, these data show that mesoporous materials generally have lower free energies compared to nonporous

materials, which implies that protein adsorption onto mesoporous silica is generally more thermodynamically favorable. The APTES-functionalized mesoporous silica, in particular, has an adsorption equilibrium constant that is two to three times larger than all of the other samples for the first binding step. This indicates that initial binding of solution protein onto the surface is quite favored and perhaps explains why these materials tend to accumulate protein in biological media of any kind. The second step for the MS@APTES sample, however, is much lower in thermodynamic favorability than the other samples, implying that for this sample, the first step is an important step in the adsorption of proteinaceous molecules onto the nanoparticle surface. The highly favorable nature of the adsorption process is revealed by these data. In all cases, the second step is less thermodynamically favorable. This suggests that the adsorption process has an a potential energy curve with a well in which the system initially equilibrates, but then molecules fall into a second well that results in an overall irreversible process.

6.4.4 Quantitative Protein Adsorption via Thermogravimetric Analysis

The FTIR studies provide unique insight into the kinetics and thermodynamics of protein adsorption onto the nanoparticle surface. However, due to the nature of the experiment, in which solution flows over the sample on the ATR crystal, there is some sample loss over the course of the total experiment. This can be spectroscopically observed as the loss of signal at around 1000 cm^{-1}, which corresponds to the Si-O stretching motion of the silica nanoparticle framework. Due to this, quantification of the total amount of adsorbed protein is very difficult. However, thermogravimetric measurements can be used to calculate the equilibrium protein adsorption. This has been

employed for these samples to obtain a saturation protein adsorption measurement for all six materials in this study. The results of the quantification are given in Figure 6.13.

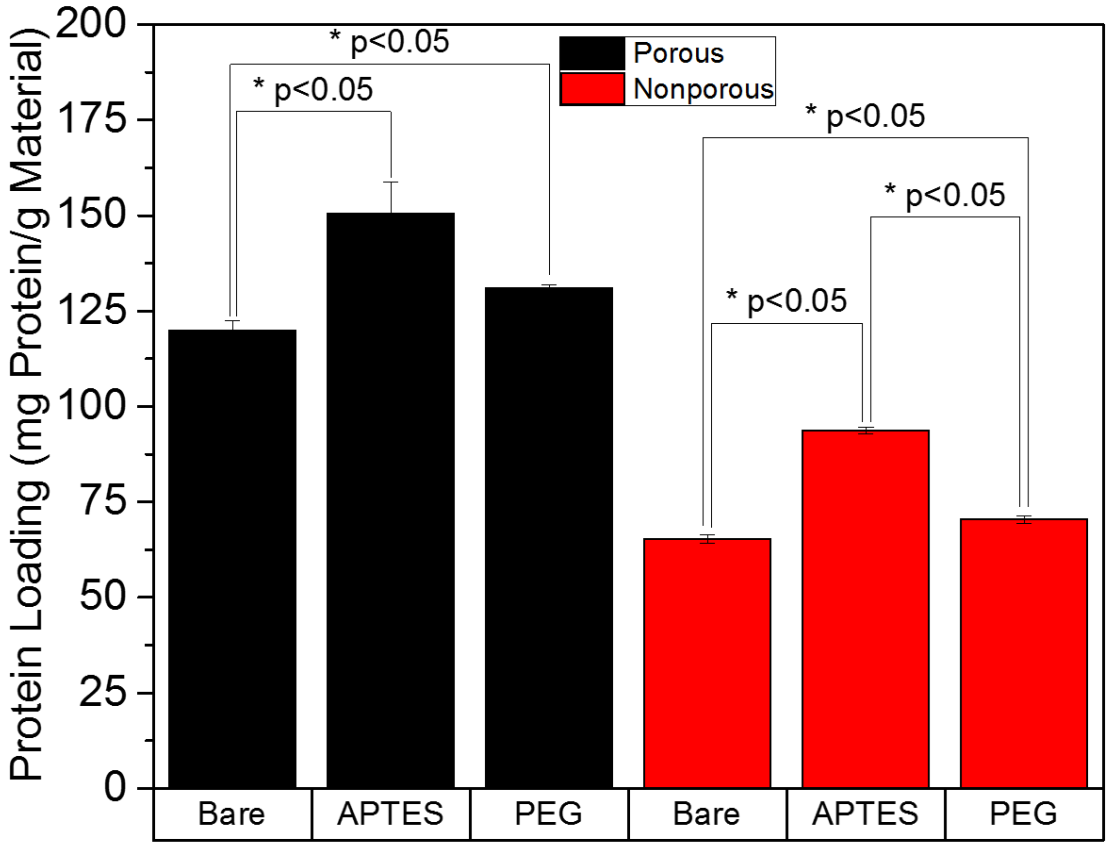

Figure 6.13 Quantitative protein adsorption via thermogravimetric analysis for samples incubated in RPMI. Differences between each sample were subjected to t-test (assuming equal or unequal variance depending on F-test results) at the $\alpha = 0.05$ level to determine statistically significant differences between samples.

The data represents the average of three replicate measurements, and were examined using a series of pairwise t-tests to determine if differences were statistically significant at the $\alpha = 0.05$ level. The results of the statistical analysis are also included in Figure 6.13. Within each porosity category (porous or nonporous) all of the differences observed are statistically significant with the exception of the porous functionalized materials (APTES vs. PEG). In this case, the p-value was 0.055, indicating the difference was almost statistically significant. In all the cases, an F-test was initially implemented to

determine if the variances were equal or not. Then this result was used to determine if the t-test was performed assuming equal or unequal variances. Furthermore, the data was subjected to a two-way analysis of variance (ANOVA), which results in the porosity and functionalization being significant variables affecting protein adsorption (porosity, $p = 4 \times 10^{-13}$; functionalization, $p = 3 \times 10^{-8}$). However, the interaction term between porosity and functionalization was not significant, nor was it expected to be. This further reinforces that nanomaterial porosity and surface chemistry strongly controls adsorption of protein at liquid-solid interfaces.

Overall, the porous materials adsorb much more protein per gram than the nonporous variants (~100% increase). This suggests that the effective surface that can adsorb protein is not just the external surface area but that some portion of the outer pores must also contribute to the adsorption surface area. A recent report in the literature implies that this observation arises from improved deposition of lower molecular weight molecules via a size exclusion effect.[160] Also, in both the porous and nonporous silica, the APTES-functionalized materials adsorb more protein than the bare materials. This indicates that the APTES moiety can enhance the extent of adsorption. This likely occurs due to the nucleophilic nature of the amine moiety and the flexibility of the aminopropyl moiety due to the aliphatic chain in the molecule.

The PEG-functionalized samples actually show more protein adsorption than the bare materials, but yet less than the APTES-functionalized materials. This result is unexpected as extensive literature suggests that PEG can diminish or completely block protein adsorption.[161-164] The only conclusion that can be drawn from this is that the PEG does interfere with protein adsorption when compared to the APTES, but still must have

some effect on the uptake and bonding. One possibility is that the PEG used in this study is of 550 average molecular weight (M_n). Differing work in the literature describes that the molecular weight as well as the brush density are important for limiting protein adsorption. From TGA measurements, the PEG loading can be approximated to be 0.314 and 0.146 mmol/g for the porous and nonporous samples, respectively. These loadings are relatively small, and can be interpreted to mean that-for the mesoporous silica-some PEG is bonded at the pore opening, but does not fully fill the porosity, as one would expect for PEG considering its large size and molecular flexibility. For complete protein blocking, the literature suggests molecular weight of several kDa for the PEG. Based on the TGA results, the nonporous silica, for example, has a density of ~1.71 PEG/nm^2, based on BET surface area and number of particles per gram (NPS = 6.9 x 10^{15} particles/g, via the method of Lin and Haynes).[102] This is a higher density than others reported in the literature, but the repeat unit is not of sufficient length to prevent protein adsorption.[165] Thus the molecules do not form a dense enough layer on the material surface to prevent adsorption, especially considering the highly favorable thermodynamics of that process.

Quantification of adsorbed protein has not been widely reported in the literature. Some studies by Clemments, et al. measured protein binding in terms of organic weight percent.[166] In that work, the protein loading is extracted as a difference between the protein-exposed material and the as-synthesized functionalized material. That work reports the loading of unfunctionalized mesoporous silica as 10.1% and amine-functionalized as 14.4%. The functionality was propylamine in that case. In our study, if the protein loading is simply considered as weight percent for the bare mesoporous

material, it gives a value of 8.2%; whereas for the amine-functionalized it is 13.3%. Thus the result that functionalization increases protein adsorption concurs with other results that have been previously reported in the literature.

6.4.5 Structural Characterization Using Circular Dichroism Spectroscopy

Infrared spectroscopy can be used to measure thermodynamic and kinetic parameters, but other complementary spectroscopic methods such as circular dichroism (CD) are often used to characterize secondary structure in proteins. The secondary structure is probed by ultraviolet radiation that has been circularly polarized. The alpha helical and beta sheet structures are sensitive to changes in their structure, and this can be monitored spectroscopically using CD spectroscopy. The alpha helical structure is particularly sensitive around 210 nm and is often used monochromatically to probe secondary structure. More often the secondary structure is characterized in free solution, but here it has been used to probe the secondary structure of adsorbed protein on the nanoparticle surface.

Numerous algorithms are available for the processing and analysis of CD spectroscopic data. The raw data is given in units of ellipticity, typically in mdeg. The protein concentration must be known precisely, as well as its molecular weight. For the analysis given here, the protein concentration was calculated based on the thermogravimetric analysis data. The protein identity was assumed to be entirely bovine serum albumin, so the molecular weight of BSA was used in the analysis. Herein, CONTIN has been applied to the data. This results in its conversion to units of mean molar ellipticity, $deg*cm^{2}*dmol^{-1}$ (see Figures 6.14 and 6.15 for the solution-phase BSA and protein-exposed nanoparticle CD spectra, respectively).

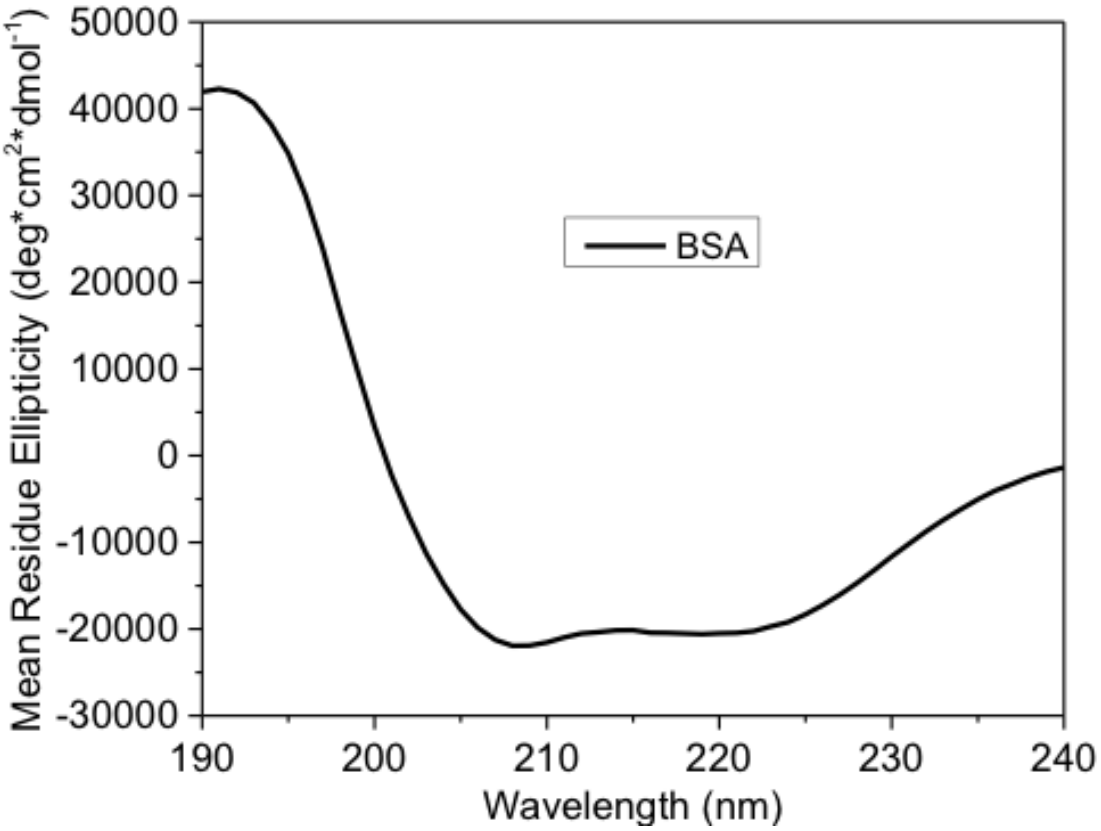

Figure 6.14 Circular dichroism spectrum of bovine serum albumin standard in chloride-free sodium phosphate buffer.

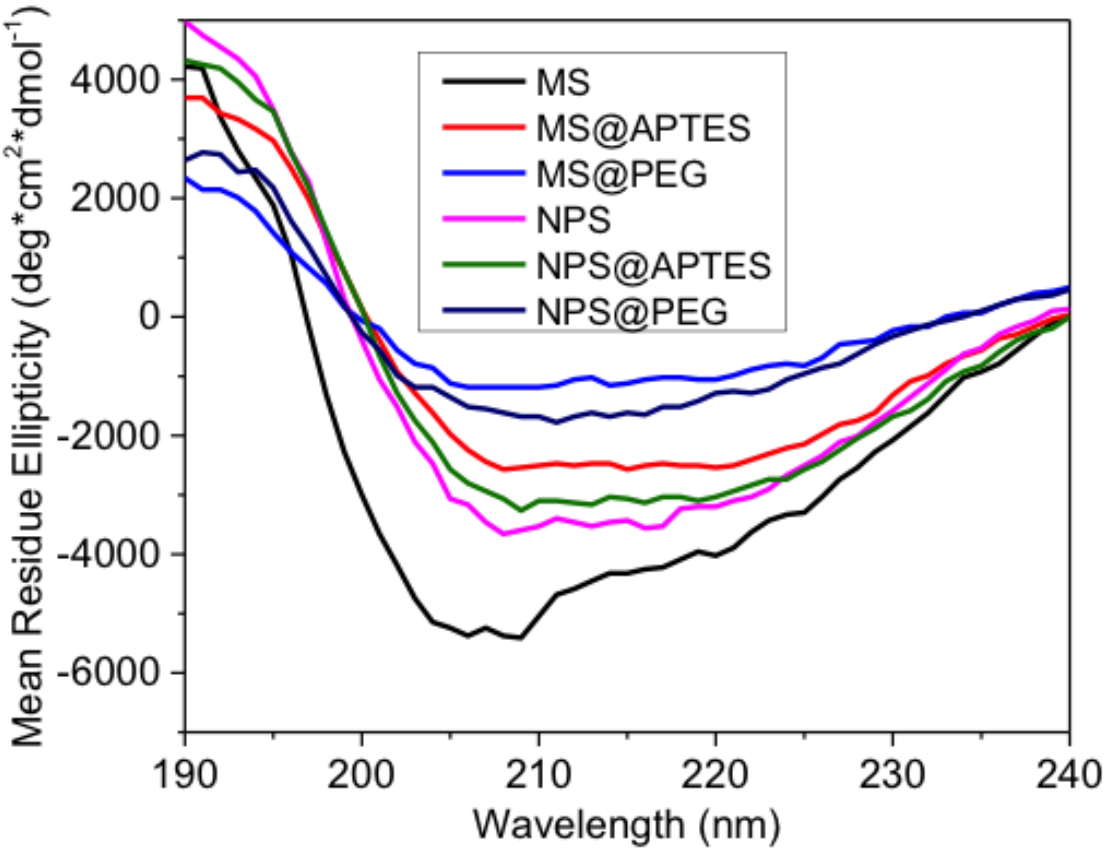

Figure 6.15 Circular dichroism spectra of the silica nanoparticle materials with adsorbed protein as measured in chloride-free buffer.

By using a fitting algorithm, the secondary structure contributions to the total CD spectrum can be extracted. The results of the CONTIN analysis and fitting are given in Table 6.4. This breaks down the secondary structure into intact and deformed alpha helix, intact and deformed beta sheet, turns, and random coils. The quantitative parameter for fitting is given as the NRMSD (normalized root-mean-square deviation). Typically, analysis requires a NRMSD value less than 0.05, which is not observed for most of the data. However, one must consider that the samples used in this measurement are solids dispersed in solution, and so there could be some interference. Measurements on the nanoparticles dispersed in solution do not give substantial spectra, so one can conclude that the particles themselves do not significantly contribute to the observed signals.

Table 6.4 Circular Dichroism Spectrum Fitting Results: Secondary Structure Characterization.

Sample	α-Helix (intact)	α-Helix (distorted)	β-Sheet (intact)	β-Sheet (distorted)	Turns	Random Coil	NRMSD
MS	5%	7%	18%	10%	18%	43%	0.08
MS@APTES	4%	6%	22%	11%	18%	40%	0.36
MS@PEG	1%	5%	24%	12%	19%	39%	1.03
NPS	4%	6%	21%	11%	19%	38%	0.24
NPS@APTES	4%	6%	21%	11%	19%	39%	0.27
NPS@PEG	2%	5%	23%	12%	20%	39%	0.73
BSA (Solution)	38%	19%	0%	3%	14%	27%	0.02

Previously reported results in the literature suggest that BSA is highly alpha helical in nature (~68%) with some substantial fraction of beta sheet (~18%) with the remainder consisting of random coils.[167] However, other reports suggest that the amount of beta sheet structure is significantly less than this (~3%).[168] As our pure solution spectrum of BSA matches more closely with the latter of these measurements, this has been used as our standard in this study (see Table 6.4 for solution-phase BSA CD secondary structure). The fitted secondary structure contributions then result in several important phenomena. First, all samples lose a great deal of alpha helical content upon adsorption onto the nanoparticle surface. This is consistent with the work of others, which demonstrates irreversible conformational changes that take place upon adsorption (*vide supra*). Secondly, a large amount of beta sheet (intact or distorted) structure appears

across the nanoparticle-containing samples. This suggests, then, that as the protein denatures, the alpha helices unfold to give beta sheet-like structures. In addition, some substantial fraction (~20%) of alpha helices unfold completely, resulting in an increase of total random coils in the protein structure.

Qualitatively the secondary structure contributions look very similar. The CD data imply that neither porosity nor the surface chemistry has a substantial effect on the secondary structure of the adsorbed protein molecules. One would expect that the different interactions between the surface moieties and the protein molecules as the adsorption process occurs would result in different structures. However, this is not the case. The CD spectroscopy, however, is an end-point measurement. It says nothing about the path through which the denaturation proceeds. So perhaps the functional moieties change the total energy landscape, thus changing how the proteins unfold. Although, given the highly thermodynamically favorable nature of the denaturation, it might not be as surprising that the end product is highly similar in all the materials. As we have no evidence for the time-dependence of the denaturation process, this line of thought is purely speculative at this time.

6.4.6 Calculated Protein Surface Coverage

The protein adsorption values obtained from thermogravimetry enable quantitative characterization of the end-state adsorption. However, to more fully understand what the nanoparticle looks like at the solid-liquid interface, these values must be converted to molecular surface coverage. A full calculation relies on the TGA measurements as well as surface areas obtained by BET adsorption isotherms. Employing these values, the molecular surface coverage can be calculated as shown in Table 6.5.

Table 6.5 Calculated Molecular Surface Coverage of BSA on Nanomaterials.

Sample	Molecular Coverage (Molecules BSA/g Material)	Molecular Coverage (Molecules BSA/cm^2)
MS	1.09 (± 0.02) x 10^{18}	9.9 (± 0.4) x 10^{10}
MS@APTES	1.36 (± 0.08) x 10^{18}	1.9 (± 0.1) x 10^{11}
MS@PEG	1.186 (± 0.008) x 10^{18}	4.7 (± 0.2) x 10^{11}
NPS	3.2 (± 0.1) x 10^{17}	4.8 (± 0.3) x 10^{11}
NPS@APTES	8.49 (± 0.07) x 10^{17}	2.02 (± 0.08) x 10^{12}
NPS@PEG	6.38 (± 0.09) x 10^{17}	1.24 (± 0.05) x 10^{12}

The nonporous material is straightforward in its calculation, but the mesoporous material is less so. The values given in Table 6.5 are those calculated based on the full BET surface area, which in the case of bare mesoporous silica is ~1100 m^2g^{-1}. If this raw BET surface area of 1100 m^2g^{-1} is used, for example, the calculated fractional surface coverage is only 0.3%, which is extremely small. This value is unrealistic in these materials for a surface coverage calculation, as the protein cannot (fully) penetrate the pore. Therefore, the true coverage values must be larger than those calculated here. If the assumption is made that the protein can somewhat penetrate into the pores, and one arbitrarily assumes a penetration depth of ~1.5 nm, then a revised surface area for the mesoporous silica sample would result in a value of ~165 m^2g^{-1}. When this value is employed, the molecular surface coverage of the material then becomes ~6.56 x 10^{11} molecules cm^{-2}. Therefore, the surface coverage would be ~2%. This is not a rigorous approximation, but is merely employed to highlight that the true molecular surface

coverage must be higher than the values reported in Table 6.5.

We also report here the number of molecules per gram of material, which has no assumptions as the number of molecules is directly calculated from the TGA data. Due to the complex nature of binding to the porous materials, it is somewhat more difficult to extract the true molecular surface coverage. The surface area calculated from BET measurements gives the total accessible surface area, but the protein cannot penetrate completely into the pores as it is too large. In addition, during its denaturation, serum albumin molecules would block the pores, preventing further entrance and adsorption. However if only a true approximated spherical external surface area was available to the protein molecules for adsorption, one would expect the bare nanomaterials to exhibit identical protein adsorption, or, if anything, that the nonporous would exhibit larger surface adsorption. This arises from the fact that if one considers the void spaces that compose the pores as inactive areas for protein adsorption, there must be less effective surface area for adsorption to occur. However, in the calculated molecular coverage, this is not what is observed, as in fact all of the porous materials show more protein adsorption on a per gram basis. This implies that some of the protein molecules must penetrate into the pores, giving a total adsorptive surface area, which is larger than just a pure external calculation, but still much smaller than that determined by BET adsorption isotherm, as implicated above.

6.4.7 Implications for Nano-Bio Interactions, Biological Assays and Biological Response

The data presented here give an important multi-faceted approach to understanding the adsorption of protein from culture medium onto silica nanomaterials. The data demonstrate that the kinetic process of protein adsorption is highly

thermodynamically favorable and that structural changes take place upon binding. The implications for these results are for *in vitro* assays that are implemented to measure cellular toxicity of engineered nanomaterials. There is some time-dependence to the adsorption process, and one can only assume protein adsorption affects cellular recognition and toxicity. When these assays are implemented to measure cellular toxicity, the nanomaterials are often dispersed in the culture medium. The data presented in this study demonstrates that dynamic changes take place at the solid-liquid interface that can alter the surface that these materials present when introduced into the cellular environment. A schematic of the modified-nanoparticles is shown in Figure 6.16 to visualize the end-point of the materials after exposure to the RPMI culture medium. In this schematic representation, the protein molecules have been visually distorted to represent their denatured status. However, as we do not have any evidence of the specific 3D structure in the denatured state, we cannot give a truly accurate picture of what these molecules look like, only a generalized schematic representation. Thus, we demonstrate the different surface chemistry and its direct impact on silica nanoparticle modifications in protein-containing culture media. This ultimately impacts all of the relevant interfacial processes nanoparticles are involved in including adsorption and cell interactions.

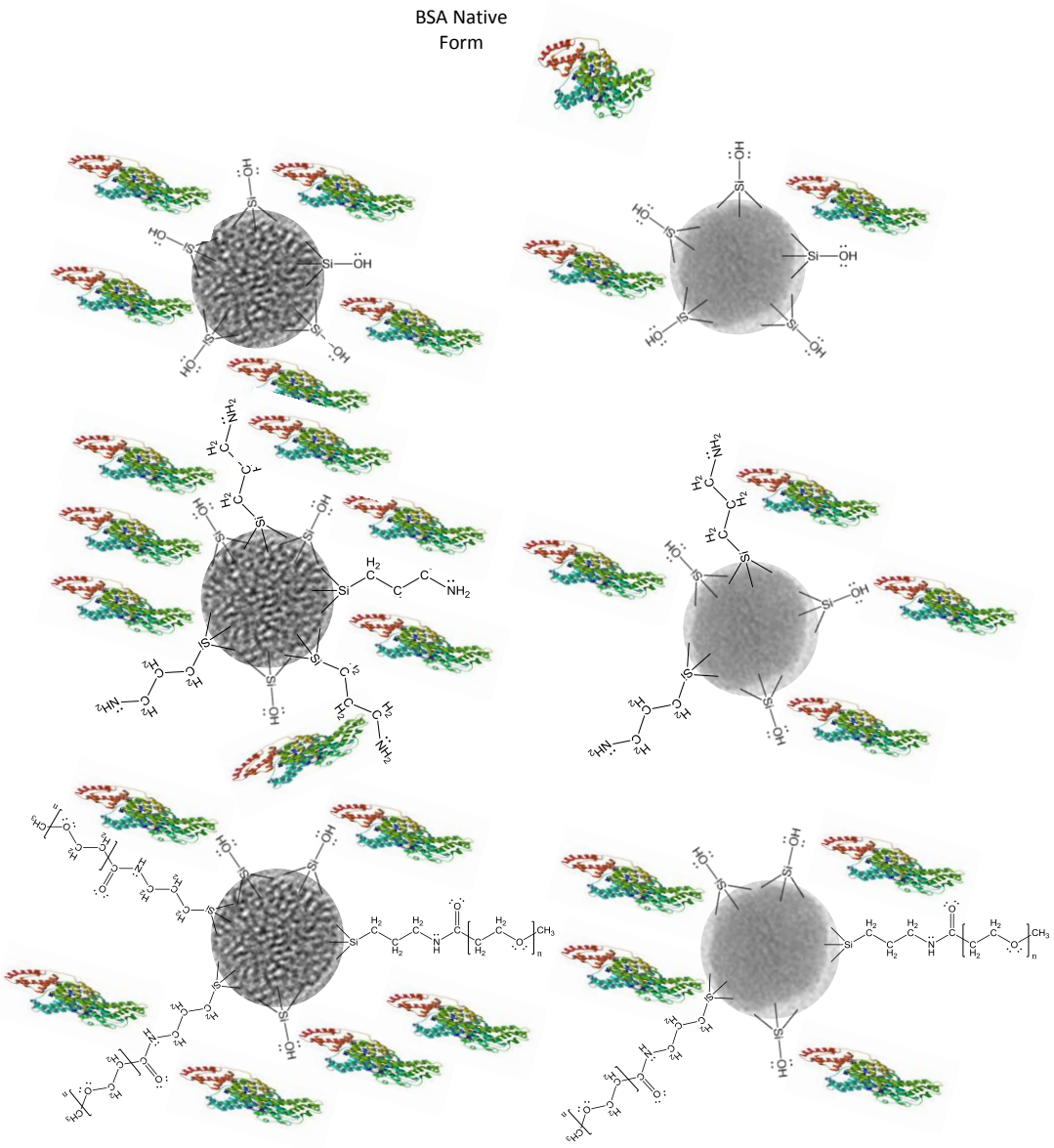

Figure 6.16 Schematic diagram of protein adsorption. The relative adsorption of BSA is shown, along with depictions of each material and its surface chemistry, consisting of surface silanols and other functional moieties, if applicable. The mesoporous materials are on the left, and the nonporous on the right. From top to bottom the surface chemistries are: bare, APTES-functionalized, PEG-functionalized. The protein molecules are shown in a distorted configuration to represent that these are the denatured protein molecules bound to the nanoparticle surface.

In *in vivo* events, there is much evidence of protein corona formation upon exposure to biological media such as serum. We demonstrate here that this also occurs in fundamental assays as a means of predicting and understanding biological responses to

nanomaterial exposures. However, RPMI contains only approximately 50 chemical components, whereas human serum contains hundreds. Thus, true biological exposure to serum could be expected to be an even more complex phenomenon. This is somewhat represented by the FBS added to the RPMI medium in this report. One could hypothesize that this exposure ultimately mitigates and/or controls *in vivo* toxicity. However, if serum albumin is truly the primary adsorptive species, as we suggest here and others have suggested elsewhere, fundamental understanding of albumin binding can facilitate better understanding of nanomaterial behavior and measurement in differing assays of significance. Considering how the interactions of nanomaterial surfaces affect cellular toxicity is critical, and is an important conclusion of this study. Indeed, the phenomena on nanoparticle surfaces seem to control many of its properties including its cytotoxicity, as we describe in a recently published report.[169] These interactions need to be measured and understood when *in vitro* data are assessed in order to determine all factors that control cellular responses. As the literature describes, the protein corona structure directly affects important biological processes such as cellular uptake, hemolysis, and apoptosis.[120, 130, 170] Thus, characterizing the structure of the protein corona is of paramount importance to ensure that nanomaterials of interest are employed effectively in critical applications such as drug delivery and biomedical imaging. The study presented here provides a benchmark for what that characterization might entail, and demonstrates the relevant implications for careful characterization of protein corona formation that occurs at solid-liquid interfaces in biological and environmental systems.

6.5 Conclusions

Overall, we conclude from this study that binding of serum albumin to the silica nanoparticles results in a surface whose charge looks very similar irrespective of surface functionalization. We assert that serum albumin is the dominant species, which adsorbs upon exposure to FBS-containing RPMI culture medium, and that it dominates the surface chemistry of the silica nanoparticles. PEG functionalization of the silica diverges from the literature, in that protein adsorption was observed on the PEG-ylated surfaces. This can be attributed to the smaller size/molecular weight of the PEG moiety. The TGA results demonstrate that functional moieties are able to recruit protein to the nanoparticle interface, which controls how biological systems view the nanoparticle-protein conjugate. Thermodynamic and kinetic measurements reveal the highly favorable nature of protein binding to nanoparticle surfaces in biological media. By obtaining a deeper understanding of the chemical changes that take place when nanomaterials are exposed to biological matrices, we can better understand how to implement these materials in applications.

CHAPTER 7
INITIAL NMR CHARACTERIZATION AND ADSORPTION STUDIES OF GLYCINE ONTO SMALL POROUS SILICA

7.1 Abstract

The work in this chapter is a set of initial studies for the application of NMR spectroscopy on small silica of less than 30 nm in primary particle size. The approach was solution-phase ^{1}H NMR to characterize the functionalized silica nanoparticles and also to study the adsorption of a small organic molecule, the amino acid glycine. The general results provide a quantitative measure of glycine adsorption as well as a direct test of the hypothesis that DOSY NMR may have an upper size limit to which it applies.

7.2 Introduction

In reference to work in Chapter 4, a question arose as to whether DOSY has a size limitation to detect and measure molecules diffusing slower than a hydrodynamic sphere of ~20 nm. As the silica studied in Chapter 4 was larger than this, it was of interest to test this hypothesis by using functionalized silica of less than ~50 nm in primary diameter. The crux of this idea is that small silica will be able to freely diffuse throughout the solution to give broadened-but detectable-proton resonances in the NMR spectrum. Furthermore, PEG is a molecule of great interest for the functionalization of nanoparticles. As an extension of the work in Chapter 4 the viability of DOSY for measuring the diffusion of small silica was tested, as well as the solution stability of PEG on the silica nanoparticle surface.

Another aspect of note is the adsorption of organic molecules onto the silica surface as detailed in Chapter 6 above.[171] So the silica was exposed to glycine to see if it would adsorb onto the surface. This represents an initial study of the viability of solution-phase NMR to measure and quantify amino acid adsorption onto the silica nanoparticle

surface. Glycine was selected due to its relatively simple structure and uncomplicated NMR spectrum. A proton NMR approach was implemented to determine if adsorption occurred, and if it could be understood in a quantitative, solution-dependent fashion.

Overall, the work in this Chapter involves application of previously described solution NMR methods to bare and functionalized silica nanoparticles of varying surface chemistry. The underlying idea is to be able to measure solution-phase events in terms of ligand stability and small organic molecular adsorption processes. The advantage of using NMR to study adsorption, in particular, is that since (almost) every organic molecule has protons within its chemical structure, it is directly amenable to adsorption studied by proton NMR. This is a direct consequence of the applicability of the methodology and approach described in this Chapter.

7.3 Methods

7.3.1 Silica Nanoparticles and Functionalization

Small porous silica (P-Type) of approximately 20 nm in size was obtained from US Research Nanomaterials (Houston, TX, USA). Functionalization with APTES and PEG functional groups was carried out using the procedure described in Chapter 2, Sections 2.4.1 and 2.4.3, respectively.

7.3.2 Sample Preparation

Samples were prepared for solution ^{1}H NMR by sonicating approximately 2 mg of functionalized MSNs in 600 μL of D_2O for 30 min. Suspended samples were transferred to standard 5 mm NMR tubes immediately prior to analysis. Sample pH was measured using a Corning 320 pH meter with a micro pH electrode and corrected using a

known isotopic correction calculation.[57] The samples were sonicated for approximately 30 minutes immediately before the NMR measurements.

7.3.3 Solution NMR Experimental Setup

1D NMR and DOSY experiments were conducted on a Bruker Avance III spectrometer operating at 400 MHz (B_0 = 9.4 T). 2D NOESY experiments were conducted on a Bruker Avance 500 MHz instrument. All ^{1}H chemical shifts were referenced to the residual solvent proton signal (for HDO this is a broad singlet centered at 4.69 ppm).

All one-dimensional ^{1}H NMR experiments were performed using a single-pulse sequence (Bruker zg pulse sequence). Pulse widths were optimized as necessary. The relevant experimental parameters were as follows: TD = 64k, NS= 16-128, and D1=1-10s. TD, NS and D1 refer to the time-domain data points, number of scans, and relaxation delay, respectively. The data were processed using Topspin 2.1 software with a 64k zero-filling and a 0.3 Hz exponential line broadening parameter. Following processing steps including phasing and baseline correction, peaks of interest were integrated to enable quantitative calculations.

7.3.4 Diffusion Ordered Spectroscopy (DOSY) Parameters

DOSY experiments were conducted using an automatic tuning and matching BBFO probe equipped with a z-gradient coil. Samples were thermally equilibrated at 298 K for 15 min before data collection. All diffusion measurements were made using the stimulated echo pulse sequence with bipolar gradient pulses (stebpgp1s pulse sequence). The diffusion delay (Δ) varied from 20 to 40 ms, and the gradient pulse duration (δ) from 1.5 to 5 ms and were optimized in order to obtain 1-5% residual signal at 95% of the

maximum gradient strength. The recycle delay varied between 5-10 s. Rectangular shapes were used for the gradients and a linear gradient of 16 increments between 2% and 95% of the maximum gradient strength was applied. The gradient strength (56.0 Gauss/cm at a current of 10 A) was calibrated by measuring the self-diffusion of the residual HDO signal in a pure D_2O (99.98 % D) sample at 298K (1.90 x 10^{-9} m^2/s). Diffusion coefficients were calculated by integrating the peaks of interest and direct curve-fitting to the Stejskal–Tanner equation:

$$I = I_0 * \exp[-\gamma^2 G^2 \delta^2 \left(\Delta - \frac{\delta}{3}\right) D] \qquad (22)$$

where I, I_0, γ, and G are the observed intensity, signal intensity in the absence of the gradient, the proton magnetogyric ratio and the gradient strength, respectively. The T_1/T_2 analysis program in Topspin was used to carry out the processing and curve-fitting for all peaks/nuclei.

7.3.5 Glycine Adsorption

Silica nanoparticles were exposed to glycine and measured for adsorption. To measure an adsorption isotherm, 10 mg of silica was massed out into dry, clean microcentrifuge tubes. To these samples, solutions of glycine hydrochloride in D_2O of varying concentrations were added to the silica and held at 4 °C for 48 hours to allow adsorption to proceed to completion. The pH of the solution was not adjusted as the glycine itself is capable of buffering the samples, being zwitterionic. The samples were centrifuged and the supernatant removed. Maleic acid in D_2O was used as an internal standard for quantitation. An aliquot of maleic acid was added to each sample and then the solutions were transferred to NMR tubes for analysis. Proton NMR spectra were recorded under quantitative conditions, the peaks of interest were integrated, and the

known concentration of maleic acid was used to calculated the residual concentration of glycine in the supernatants was calculated. The amount of adsorbed glycine was calculated by difference from the initial solution, these values were converted to adsorbed amount (mg Gly/g SPS) and plotted to give a Freundlich adsorption isotherm.

7.4 Results and Discussion

7.4.1 Material Characterization

The purchased silica nanoparticles (small porous silica, SPS) were characterized using typical physical and chemical methods. Transmission electron microscopy was used to confirm the primary particle size as shown in Figure 7.1. The particle size is approximately 20 nm for the primary particles. The particles are clearly aggregated, but this is not surprising considering their high intrinsic surface energy due to their small particle size. The materials were also characterized using methods such as gas adsorption isotherms and thermogravimetric analysis. The results of the characterization are shown in below.

Table 7.1 Characterization Data for Bare and Functionalized Small Porous Silica (SPS).

Sample	Surface Area (m^2/g)	Pore Volume (mL/g)	Pore Diameter (nm)	Functional Group Loading (mmol/g)
Small Porous Silica (SPS)	580 (± 20)	0.28 (± 0.02)	3.712 (± 0.001)	N/A
SPS@APTES	24 (± 1)	0.077 (± 0.005)	3.150 (± 0.007)	2.289 (± 0.004)
SPS@PEG	35 (± 1)	0.125 (± 0.007)	9.89 (± 0.02)	0.288 (± 0.001)

Of note is the dramatic decrease in surface area upon functionalization of the surface with either the APTES or PEG functionalities. The measured pore diameter seems to increase for the PEG-ylated sample, which seems an anomalous result. The functional group loading is as expected, with the APTES material showing higher loading than the much

larger PEG moiety. The diminished measured pore volumes are consistent with functionalization.

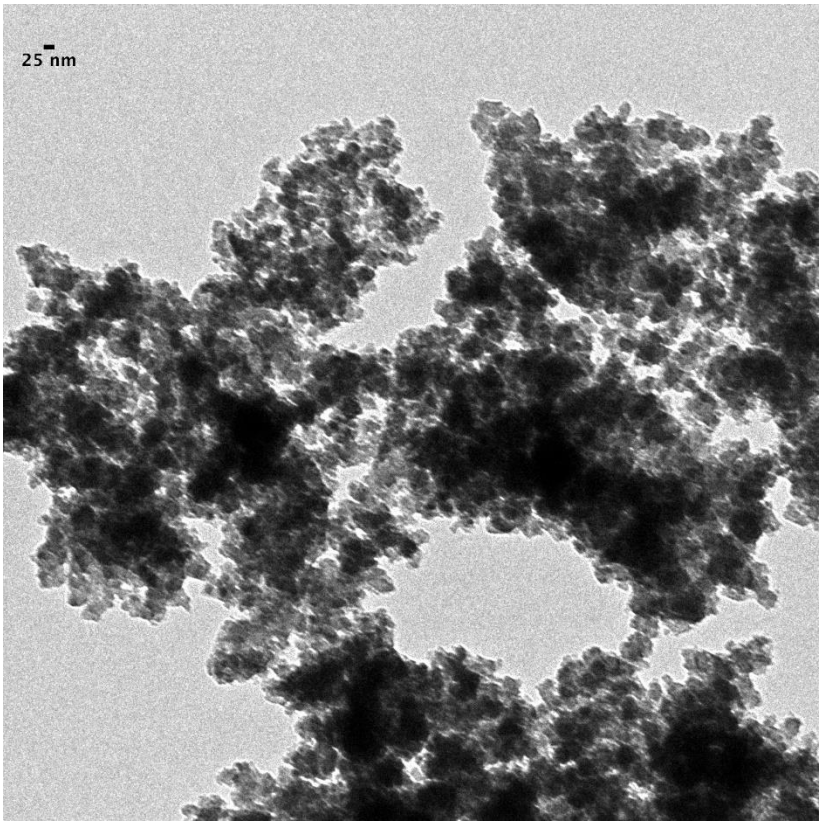

Figure 7.1 Small porous silica used in these studies. The scale bar is 25 nm.

7.4.2 1D Proton NMR Ligand Characterization

A combination of 1D proton NMR, DOSY, and 2D NOESY was used to characterize the functionalized materials. The initial 1D ^{1}H NMR was used to confirm the functional group identity and ensure the species of interest was grafted onto the nanoparticle surface. The ^{1}H NMR spectra of the functionalized materials can be seen in Figures 7.2 and 7.3. The APTES functionality should give rise to three groups of protons, as observed in Figure 7.2. The chemical shifts of the methylene protons confirm the identity, as well as the integrated intensities. The PEG functionalized material was also characterized using 1D ^{1}H NMR and the signals observed seen in Figure 7.3 are not what was expected. The solution-phase spectrum of the PEG molecule itself in solution is

given in Figure 7.4 and shows extra signals that do not appear in the spectrum of the functionalized material itself. This can be due to the motional broadening of those signals as the material diffuses throughout the solution.

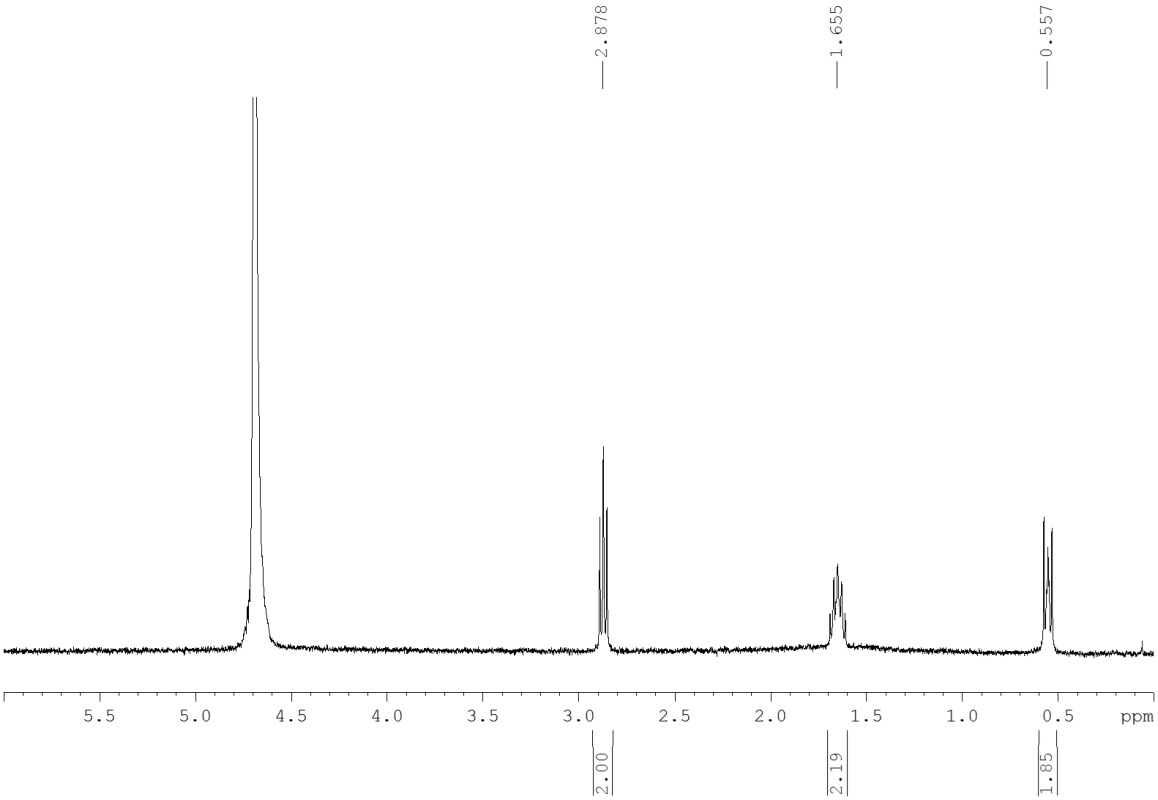

Figure 7.2 Proton NMR spectrum of SPS@APTES in D_2O. The three characteristic groups of methylene protons are visible with their chemical shift values (above) as well as integrated intensities (below).

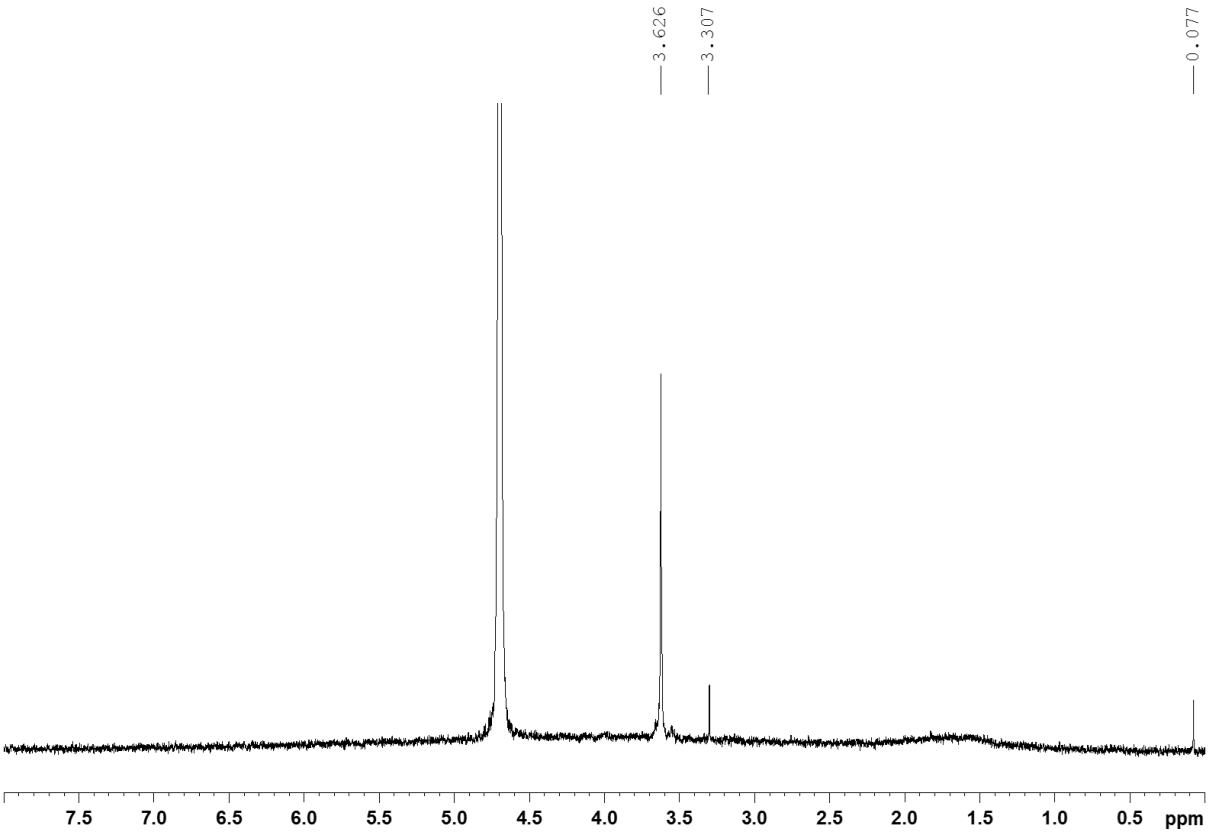

Figure 7.3 Proton NMR spectrum of SPS@PEG in D_2O. The main signal corresponding to the repeat chain unit in the polymer are detected at 3.6 ppm. The other signal at 3.3 ppm corresponds to the terminal methyl group protons.

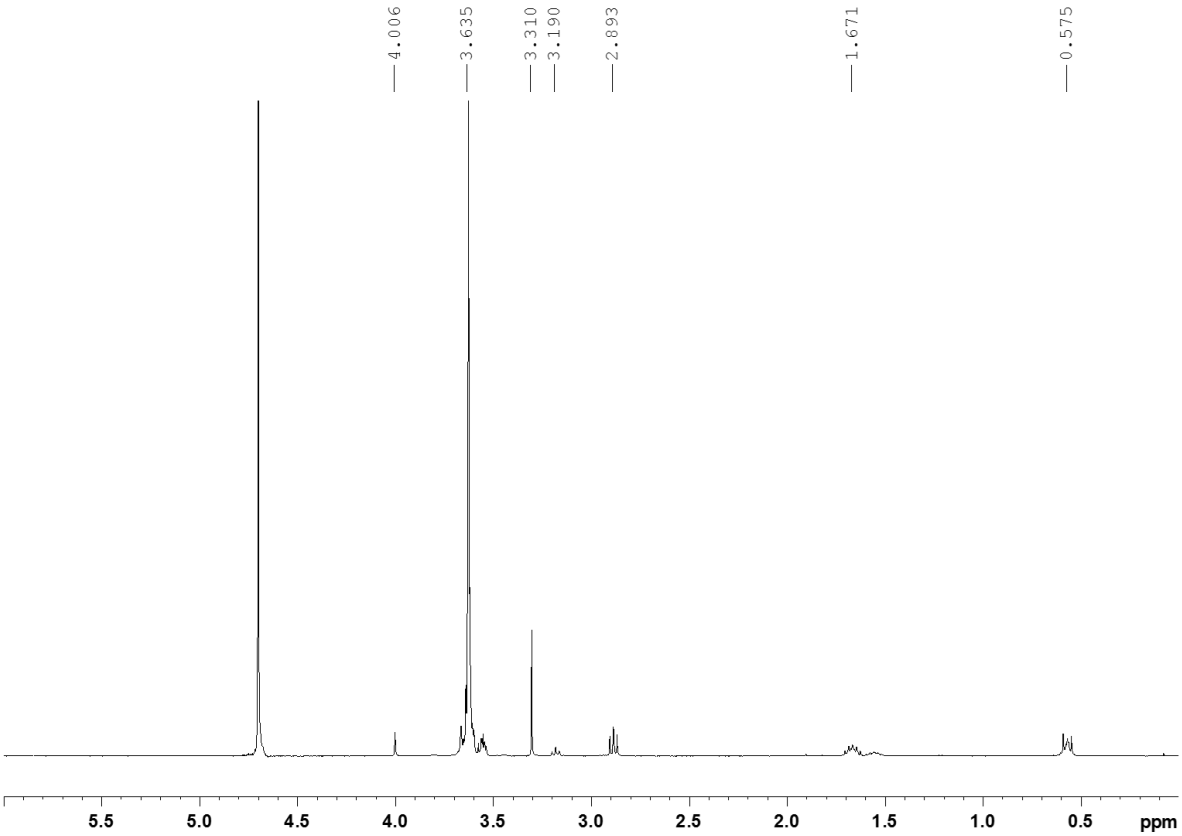

Figure 7.4 Proton NMR spectrum of PEG-APTES conjugate used to functionalize the silica. A variety of signals from the PEG chain and signals from the APTES moiety are shown.

7.4.3 2D NMR Ligand Characterization

Due to the hypothesis that DOSY NMR is size-limited and that it cannot detect molecules attached to particles larger than approximately 30 nm, the functionalized materials probed herein provide a means to directly test this hypothesis. DOSY NMR was employed on both the free ligands as well as the functionalized materials to experimentally measure the diffusion coefficients of the chemical systems. The results of this analysis are shown in Table 7.2.

Table 7.2 Diffusion Coefficients Measured by DOSY for Free and Functionalized Forms.

Sample	APTES	SPS@APTES	PEG	SPS@PEG
Average (± SD)	3.04 (± 0.06) x 10^{-10}	5.19 (± 0.05) x 10^{-10}	4.0 (± 1) x 10^{-10}	2.53 x 10^{-10}

As is apparent from the measured diffusion coefficients, in the APTES system, there seems to be faster diffusion in the bound system. This is indicated by the larger diffusion coefficient for the SPS@APTES system. The bound ligands are expected to have a diffusion coefficient of ~1.7 x 10^{-11} m^2s^{-1}. This result is anomalous, and requires further experimentation to resolve the discrepancy. The PEG system, however shows a more expected (although still puzzling) result in that the measured diffusion coefficient of the free molecule is larger than the functionalize material. The change is in the expected direction, but the measured diffusion coefficient is too large for the primary particle size. The data suggests that the molecule is diffusing faster than the bounded ligand would if it was bonded to the particle. A possible explanation of this may be that the molecule is rapidly exchanging between bound and free forms, and that most of the molecules is in the free state, heavily weighting the measured average toward that of the free molecule.

7.4.4. Glycine Adsorption Characterization

Glycine was allowed to interact with the silica nanoparticles in aqueous (D_2O) solution. The solution-phase ^1H NMR spectrum of glycine is quite simple in that it consists of only a single (singlet) peak. This is due to the chemical and magnetic equivalence of the two backbone protons in the structure. The amino and carboxylic protons undergo rapid exchange in aqueous solution and so are not detectable in D_2O solution. By using careful experimental methodology, a glycine adsorption isotherm on the bare and APTES functionalized materials was measured. The results of the measured adsorption isotherms are shown in Figures 7.7 and 7.8. The data for each isotherm were fit to the Freundlich adsorption isotherm equation:

$$q_e = k * {C_e}^b \text{ (x)}$$

Here, q_e is the adsorption capacity given in mmol Gly/g material, C_e is the initial adsorption capacity in mM, k is the adsorption constant, and b is the Freundlich constant.[172] The value of the Freundlich constant (b) as being near one indicates that the adsorption proceeds in an independent fashion. What is meant by this is that the adsorption of each adsorbate molecule does not depend on the adsorption of other molecules. Thus, there is neither a competitive nor cooperative mechanism of binding for glycine onto the silica surfaces. This is probably only a caveat of the low concentration regime, which is predicted to be more non-linear at higher concentrations.

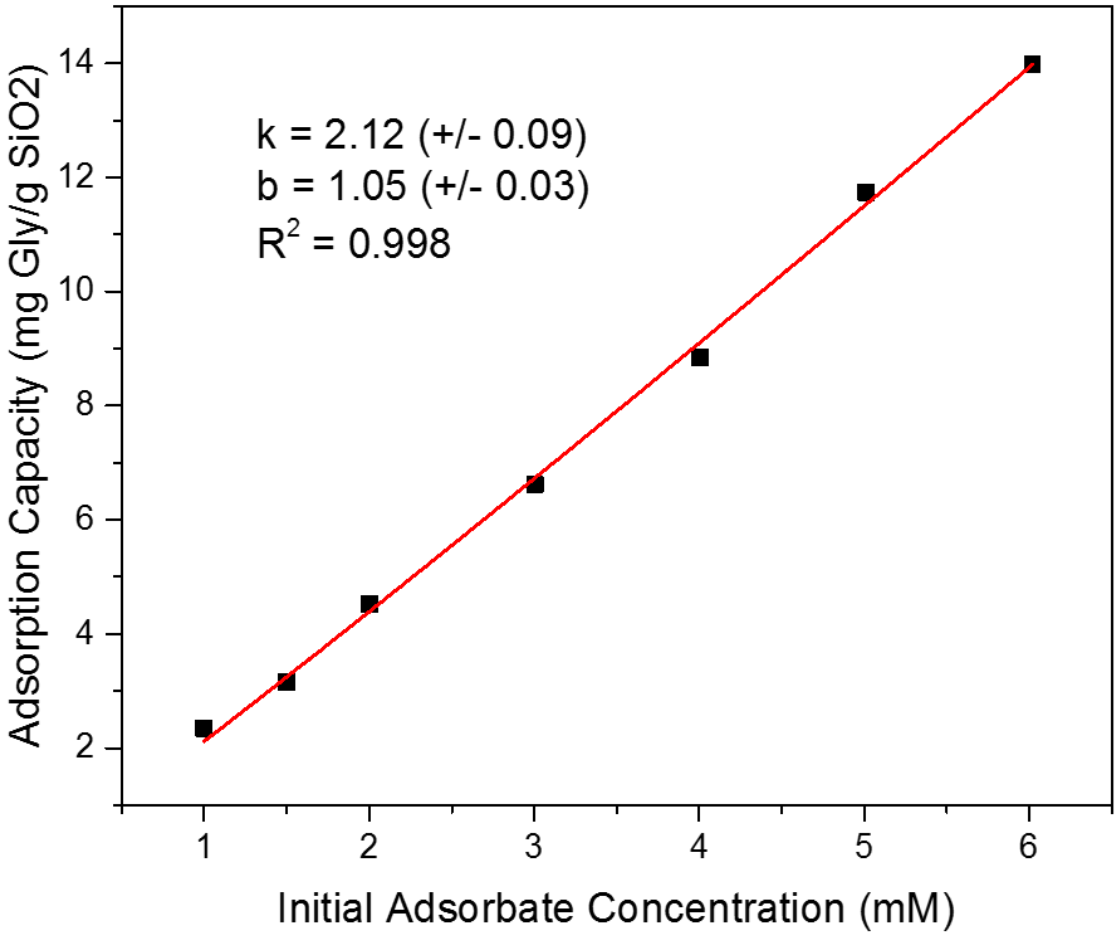

Figure 7.5 Freundlich adsorption isotherm for glycine on SPS.

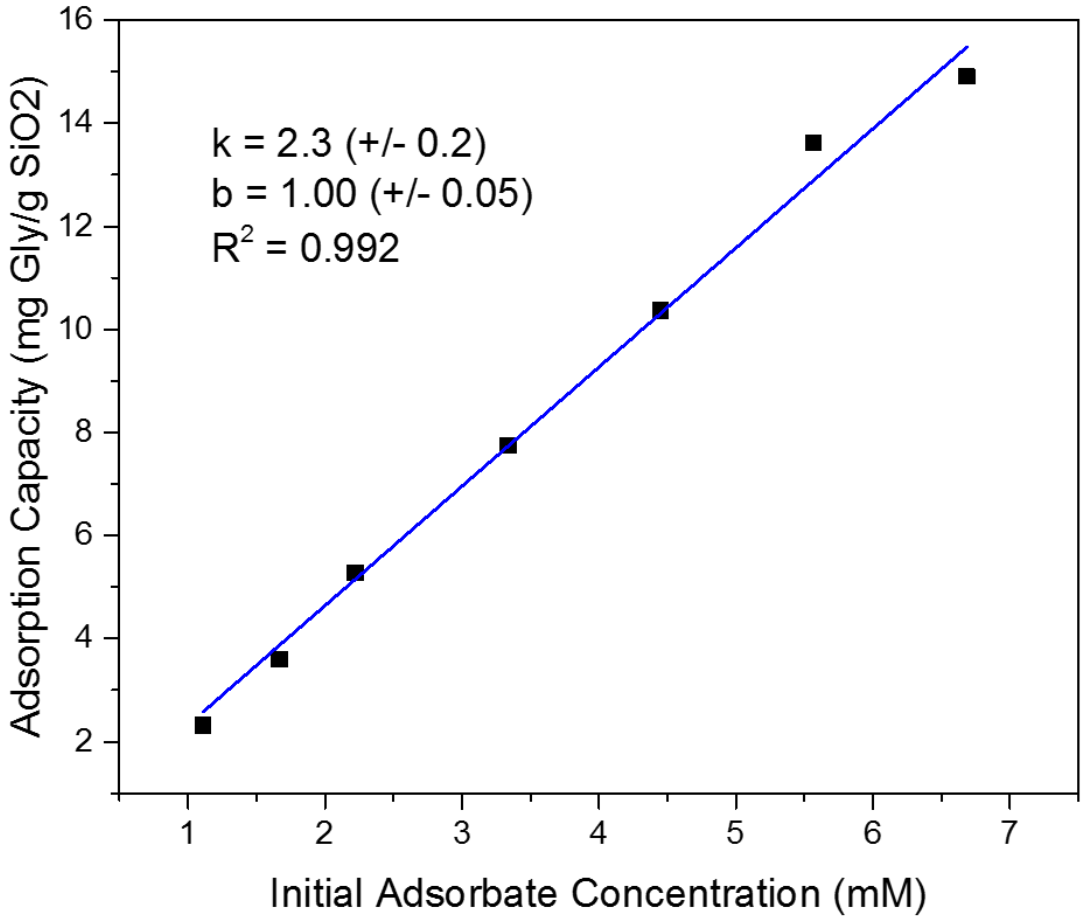

Figure 7.6 Freundlich adsorption isotherm for glycine on SPS@APTES.

The internal standard used for the adsorption isotherms was maleic acid. Maleic acid is an appropriate standard owing to its single proton resonance centered at 6.30 ppm from the two equivalent protons and its high aqueous solubility (~4 M). The maleic acid resonance is very well resolved from the glycine resonance around 3.70 ppm. Both of the peaks are also well resolved from the broad residual proton signal at 4.69, which can interfere with accurate integration and thus quantification.

In order to determine if the bound glycine could be detected, two samples were prepared. Glycine at ~ 3.5 mM (in D_2O) was added to 2.5 mg of bare SPS and allowed to equilibrate at 4 °C for 48 hours. Then one sample was sonicated for 30 min to disperse the silica and the proton spectrum recorded. The other sample was washed in triplicate

with D_2O to remove free and weakly bound glycine, then sonicated and transferred for proton NMR spectroscopy. The results of these experiments are shown together in Figure 7.6. Here both spectra are superimposed together to highlight key spectral differences.

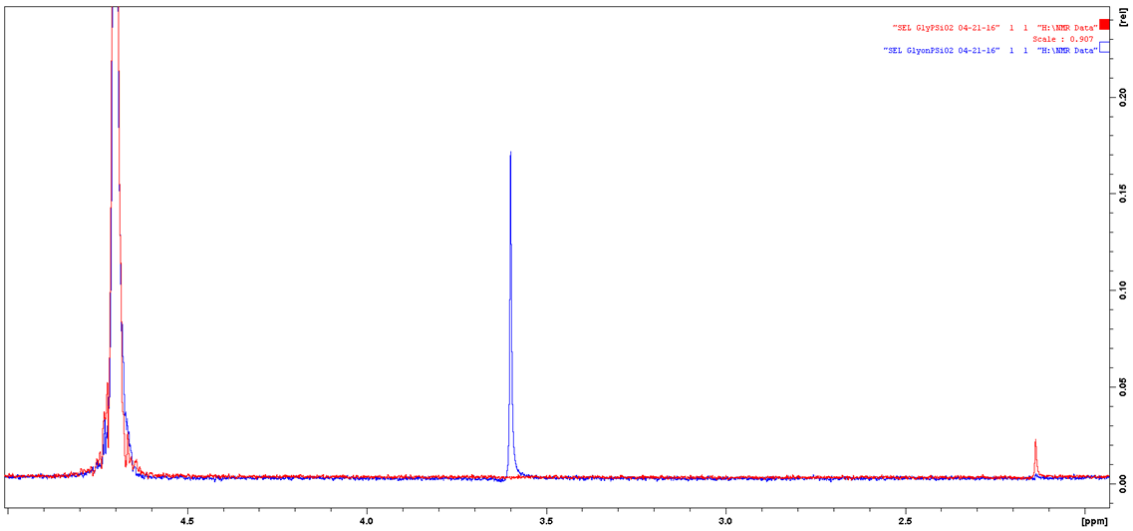

Figure 7.7 Stacked spectra of SPS in 3.5 mM glycine (blue) and glycine-exposed SPS that was washed and transferred into D_2O for measurement (red).

It is of note that the peak at 3.6 ppm shifts dramatically in the washed sample by almost 1.5 ppm to ~2.1 ppm. This suggests the local electronic environment has changed. Due to the upfield shift of the peak, it can be inferred that what is actually observed is adsorbed glycine on the nanoparticle surface. This follows logically when one considers the shielding nature of the surface silicon atoms in the nanoparticle. It is also possible to see the same shifted peak in the initial 3.5 mM glycine solution, albeit at a much diminished intensity. Overall, the intensity of the glycine in the washed sample is much attenuated, and since these two samples were collected under identical experimental conditions, it can be assumed that the loss of the main signal around 3.6 ppm for solution-phase glycine can be attributed to the washing away of residual molecules during the wash step.

7.5 Conclusions

Taken together, the data obtained thus far imply that the PEG molecules on the nanoparticle surface are not sufficiently mobile for true solution-phase measurement. However, the concurrent result of the APTES molecule also suggests that only the free molecule is observed in solution. Perhaps, then, it is not the size of the particle that determines detectable phenomena when probed by solution-phase NMR, but rather depends on the length and mobility of the ligand bonded to the surface. The glycine adsorption measurements show that glycine adsorbs in a linear, concentration-dependent fashion over the range of concentrations studied here. The final experiment implies that distinct chemical shifts can be observed for bonded species that directly interact with the silica nanoparticle surface.

CHAPTER 8
CONCLUSIONS AND FUTURE WORK

8.1 Conclusions

The work reported in this thesis describes a series of spectroscopic studies carried out on silica nanoparticles varied in porosity, surface chemistry, and size. Spectroscopic characterization ranges from the most fundamental of functionalized particles with ligands to applied characterization of free radical generation at the surface. Spectroscopy, in particular, is well-suited to provide detailed molecular-level understanding about surface phenomena that are of interest when implementing these materials in various applications of interest. Silica nanoparticles have made great strides in recent years for key applications including biomedical, environmental, and catalytic areas of interest. However, a deeper understanding of how interfacial and surface phenomena control their properties is needed before they can be truly implemented in these key areas.

The work carried out for this thesis demonstrates several key findings that can be considered when these materials are implemented in applications. Ligands were shown to be dynamic entities undergoing complex chemical exchange, with structural dependence on their bonding and release. It was also demonstrated that free radical generation at the silica nanoparticle surface can be directly correlated to the observed toxicity of the silica nanoparticles, and that the production of ROS is a surface-catalyzed process. An extension of the toxicity studies measured protein adsorption from cell culture medium commonly used for toxicological assessment. Furthermore, the adsorption of protein was treated in a quantitative way to provide deeper understanding into how protein modifies the surface of the silica nanoparticles upon exposure. The ultimate implication of this

work is to demonstrate how extensive material characterization can facilitate better silica nanomaterial design and implementation for applications of interest and human safety.

8.2 Future Work

Despite the results reported in this thesis, more work still could be done to expand upon the studies already carried out. In the initial characterization of the ligands by NMR, several questions remain. In particular, the dependence of the release on sample pH could be investigated to determine what effect, if any, it would have on the systems studied. The studies could also be expanded to look at non-ionic moieties to see if the absence of acid-base chemistry would alter the measured results. Additionally, it is-at least in principle-possible to measure the kinetic rate constants for the exchange process using a series of NOESY experiments at incremented mixing times under full relaxation conditions. It would also be of interest to see the effect higher ionic strength has on ligand release and binding to more closely mimic biological or environmental media.

The toxicity studies could be expanded by using a variety of materials and studying them under different conditions. In particular, the surface chemistry could be expanded to see its effect on observed toxicity as well as free radical production. The EPR experiments could be replicated and extended to verify the proposed mechanism through mechanistic study. The equivalent experiments in RPMI without the FBS could also be carried out to determine if the protein adsorption process impacts the free radical generation and/or toxicity. It would also be of interest to redo the experiments by first adsorbing protein onto the surfaces by exposing them to the culture medium, then measuring ROS produced at the surface by the EPR methodology. Also, by grafting a high density of PEG with long chain lengths, it would be possible to see if the toxicity and ROS production is affected as people have hypothesized that the large polymeric

moieties block protein adsorption and are the resultant cause behind diminished observed biological toxicity in various cellular and organismal assays.

It would also be of interest to do more experiments in the biological media, as well as seeing the effect of protein concentration on adsorption to determine any concentration-dependence. Concentration effects on protein structure and adsorbed quantity would also be of interest, although one might expect that these end-point experiments will not vary much as a function of the concentration. Isothermal titration calorimetry could also be used to measure thermodynamics of the binding process, although it was not very successful when the initial experiments were attempted. It might be more useful to try it with smaller silica particles, but the experiments themselves are technically challenging with profuse washing and sample equilibration in the RPMI buffer without the FBS necessary. It could also be carried out by doing a simplified version of the experiment in a pure PBS solution-with and without FBS-as an initial test to determine the general conditions required for successful isotherm development.

An extension of the overall work would be to use very small silica (<20 nm) as most of the nanoparticles used in these studies were around the 50-70 nm regime. The overall conclusions may change particularly for the toxicity and protein adsorption studies. The size is predicted to have less of an effect on the ligand binding and release but the NMR may be experience better resolution at smaller sizes. The final chapter implies that for much smaller silica, the binding of molecules on the surface-and even the ligands themselves-may be more amenable to direct spectroscopic detection by NMR. Finally, the glycine adsorption work could be expanded into full study by examining the effect of pH as well as selective adsorption in the presence of other amino acids.

REFERENCES

1. Lu, Q.; Chen, D.; Jiao, X. Fabrication of Mesoporous Silica Microtubules Through the Self-Assembly Behavior of β-Cyclodextrin and Triton X-100 in Aqueous Solution. *Chem. Mater.* **2005,** *17*, 4168-4173.
2. Nooney, R. I.; Thirunavukkarasu, D.; Chen, Y.; Josephs, R.; Ostafin, A. E. Synthesis of Nanoscale Mesoporous Silica Spheres with Controlled Particle Size. *Chem. Mater.* **2002,** *14* (11), 4721-4728.
3. Lehman, S. E.; Larsen, S. C. Zeolite and Mesoporous Silica Nanomaterials: Greener Syntheses, Environmental Applications and Biological Toxicity. *Environ. Sci.: Nano* **2014,** *1*, 200-213.
4. IUPAC. *Compendium of Chemical Terminology* [Online]; Blackwell Scientific Publications: Oxford, UK, 2014.
5. Kobler, J.; Möller, K.; Bein, T. Colloidal Suspensions of Functionalized Mesoporous Silica Nanoparticles. *ACS Nano* **2008,** *2* (4), 791-799.
6. Stöber, W.; Fink, A.; Bohn, E. Controlled Growth of Monodisperse Silica Spheres in the Micron Size Range. *J. Colloid Inter. Sci.* **1968,** *26* (1), 62-69.
7. Nozawa, K.; Gilhanou, H.; Raison, L.; Panizza, P.; Ushiki, H.; Sellier, E.; Delville, J. P.; Delville, M. H. Smart Control of Monodisperse Stöber Silica Particles: Effect of Reactant Addition Rate on Growth Process. *Langmuir* **2005,** *21* (4), 1516-1523.
8. Tao, Z. M.; Toms, B. B.; Goodisman, J.; Asefa, T. Mesoporosity and Functional Group Dependent Endocytosis and Cytotoxicity of Silica Nanomaterials. *Chem. Res. Toxicol.* **2009,** *22* (11), 1869-1880.
9. Maurer-Jones, M. A.; Lin, Y.-S.; Haynes, C. L. Functional Assessment of Metal Oxide Nanoparticle Toxicity in Immune Cells. *ACS Nano* **2010,** *4* (6), 3363-3373.
10. Napierska, D.; Thomassen, L. C.; Lison, D.; Martens, J. A.; Hoet, P. H. The Nanosilica Hazard: Another Variable Entity. *Particle and Fibre Toxicology* **2010,** *7* (39).
11. Yu, Y.; Li, Y.; Wang, W.; Jin, M.; Du, Z.; Li, Y.; Duan, J.; Yu, Y.; Sun, Z. Acute Toxicity of Amorphous Silica Nanoparticles in Intravenously Exposed ICR Mice. *PLoS One* **2013** **,** *8* (4).
12. Zhang, H. Y.; Dunphy, D. R.; Jiang, X. M.; Meng, H.; Sun, B. B.; Tarn, D.; Xue, M.; Wang, X.; Lin, S. J.; Ji, Z. X.; Li, R. B.; Garcia, F. L.; Yang, J.; Kirk, M. L.; Xia, T.; Zink, J. I.; Nel, A.; Brinker, C. J. Processing Pathway Dependence of Amorphous Silica Nanoparticle Toxicity: Colloidal vs Pyrolytic. *Journal of the American Chemical Society* **2012,** *134* (38), 15790-15804.
13. Lin, Y. S.; Haynes, C. L. Synthesis and Characterization of Biocompatible and Size-Tunable Multifunctional Porous Silica Nanoparticles. *Chemistry of Materials* **2009,** *21* (17), 3979-3986.
14. Tarn, D.; Ashley, C. E.; Xue, M.; Carnes, E. C.; Zink, J. I.; Brinker, C. J. Mesoporous Silica Nanoparticle Nanocarriers: Biofunctionality and Biocompatibility. *Accounts of Chemical Research* **2013,** *46* (3), 792-801.
15. Wu, S.-H.; Lin, Y.-S.; Hung, Y.; Chou, Y.-H.; Hsu, Y.-H.; Chang, C.; Mou, C.-Y. Multifunctional Mesoporous Silica Nanoparticles for Intracellular Labeling and Animal Magnetic Resonance Imaging Studies. *ChemBioChem* **2008,** *9*, 53-57.

16. Samri, M. T. A.; Biradar, A. V.; Alsuwaidi, A. R.; Balhaj, G.; Al-Hammadi, S.; Shehab, S.; Al-Salam, S.; Tariq, S.; Pramathan, T.; Benedict, S.; Asefa, T.; Souid, A.-K. In Vitro Biocompatibility of Calcined Mesoporous Silica Nanoparticles and Fetal Blood Cells. *International Journal of Nanomedicine* **2012,** *7*, 3111-3121.
17. Zhang, H. Y.; Dunphy, D. R.; Jiang, X. M.; Meng, H.; Sun, B. B.; Tarn, D.; Xue, M.; Wang, X.; Lin, S. J.; Ji, Z. X.; Li, R. B.; Garcia, F. L.; Yang, J.; Kirk, M. L.; Xia, T.; Zink, J. I.; Nel, A.; Brinker, C. J. Processing Pathway Dependence of Amorphous Silica Nanoparticle Toxicity: Colloidal vs Pyrolytic. *J. Am. Chem. Soc.* **2012,** *134* (38), 15790-15804.
18. Valentine, J. S.; Wertz, D. L.; Lyons, T. J.; Liou, L.-L.; Goto, J. J.; Gralla, E. B. The Dark Side of Dioxygen Biochemistry *Current Opinion in Chemical Biology* **1998,** *2*, 253-262.
19. Hudson, S. P.; Padera, R. F.; Langer, R.; Kohane, D. S. The biocompatibility of mesoporous silicates. *Biomaterials* **2008,** *29* (30), 4045-4055.
20. Yu, T.; Hubbard, D.; Ray, A.; Ghandehari, H. In vivo biodistribution and pharmacokinetics of silica nanoparticles as a function of geometry, porosity and surface characteristics. *Journal of Controlled Release* **2012,** *163* (1), 46-54.
21. Li, S. D.; Chen, Y. C.; Hackett, M. J.; Huang, L. Tumor-Targeted Delivery of siRNA by Self-Assembled Nanoparticles. *Molecular Therapeutics* **2008,** *16*, 163-169.
22. Aisen, P.; Leibman, A.; Zweier, J. Stoichiometric and Site Characteristics of the Binding of Iron to Human Transferrin. *Journal of Biological Chemistry* **1978,** *253* (6), 1930-1937.
23. Ahmad, J.; Ahamed, M.; Akhtar, M. J.; Alrokayan, S. A.; Siddigui, M. A.; Musarrat, J.; A., A.-K. A. Apoptosis Induction by Silica Nanoparticles Mediated Through Reactive Oxygen Species in Human Liver Cell Line HepG2. *Toxicology and Applied Pharmacology* **2012,** *259* (2), 160-168.
24. Murray, C.; Derro, E. L.; Sechler, T. D.; Lester, M. I. Weakly Bound Molecules in the Atmosphere: A Case Study of HOOO. *Accounts of Chemical Research* **2009,** *42* (3), 419-427.
25. Ghiazza, M.; Polimeni, M.; Fenoglio, I.; Gazzano, E.; Ghigo, D.; Fubini, B. Does Vitreous Silica Contradict the Toxicity of the Crystalline Silica Paradigm? *Chem. Res. Toxicol.* **2010,** *23* (3), 620-629.
26. Yildirim, A.; Ozgur, E.; Bayindir, M. Impact of Mesoporous Silica Nanoparticle Surface Functionality on Hemolytic Activity, Thrombogenicity and Non-Specific Protein Adsorption. *Journal of Materials Chemistry B* **2013,** *1*, 1909-1920.
27. Townson, J. L.; Lin, Y.-S.; Agola, J. O.; Carnes, E. C.; Leong, H. S.; Lewis, J. D.; Haynes, C. L.; Brinker, C. J. Re-examining the Size/Charge Paradigm: Differing in Vivo Characteristics of Size- and Charge-Matched Mesoporous Silica Nanoparticles. *Journal Of The American Chemical Society* **2013,** *135* (43), 16030-16033.
28. Cai, Q.; Luo, Z.-S.; Pang, W.-Q.; Fan, Y.-W.; Chen, X.-H.; Cui, F.-Z. Dilution Solution Routes to Various Controllable Morphologies of MCM-41 Silica with a Basic Medium. *Chem. Mater.* **2001,** *13* (2), 258-263.
29. Moller, K.; Kobler, J.; Bein, T. Colloidal Suspensions of Nanometer-Sized Mesoporous Silica. *Adv. Funct. Mater.* **2007,** *17* (4), 605-612.

30. Barrera, C.; Herrera, A. P.; Rinaldi, C. Colloidal Dispersions of Monodisperse Magnetite Nanoparticles Modified with Poly(Ethylene Glycol). *J. Colloid Inter. Sci* **2009,** *329*, 107-113.
31. Brunauer, S.; Emmett, P. H.; Teller, E. Adsorption of Gases in Multimolecular Layers. *J. Am. Chem. Soc.* **1938,** *60* (2), 309-319.
32. Barrett, E. P.; Joyner, L. G.; Halenda, P. P. The Determination of Pore Volume of Area Distributions in Porous Substances. I. Computations from Nitrogen Isotherms. *J. Am. Chem. Soc.* **1951,** *73* (1), 373-380.
33. McCusker, L. B.; Liebau, F.; Engelhardt, G. Nomenclature of Structural and Compositional Characteristics of Ordered Microporous and Mesoporous Materials with Inorganic Hosts. *Pure Appl. Chem.* **2001,** *73* (2), 381-394.
34. Konvalina, G.; Haick, H. Sensors for Breath Testing: From Nanomaterials to Comprehensive Disease Detection. *Acc. Chem. Res.* **2014,** *47* (1), 66-76.
35. Hammond, P. T. Virtual Issue on Nanomaterials for Drug Delivery. *ACS Nano* **2011,** *5* (2), 681-684.
36. Sethi, M.; Pacardo, D. B.; Knecht, M. R. Biological Surface Effects of Metallic Nanomaterials for Applications in Assembly and Catalysis. *Langmuir* **2010,** *26* (19), 15121-15134.
37. Park, J.-U.; Lee, J. H.; Paik, U.; Lu, Y.; Rogers, J. A. Nanoscale Patterns of Oligonucleotides Formed by Electrodynamic Jet Printing with Applications in Biosensing and Nanomaterials Assembly. *Nano Lett.* **2008,** *8* (12), 4210-4216.
38. Han, L.; Zhou, Y.; He, T. One-Pot Morphology-Controlled Synthesis of Various Shaped Mesoporous Nanoparticles. *J. Mater. Sci.* **2013,** *48* (17), 5718-5726.
39. Zhang, K.; Xu, L. L.; Jiang, J.-G.; Calin, N.; Lam, K.-F.; Zhang, S.-J.; Wu, H.-H.; Wu, G.-D.; Albela, B.; Bonneviot, L.; Wu, P. Facile Large-Scale Synthesis of Monodisperse Mesoporous Silica Nanospheres with Tunable Pore Structure. *J. Am. Chem. Soc.* **2013,** *135* (7), 2427-2430.
40. Zhang, H.; Dunphy, D. R.; Jiang, X.; Meng, H.; Sun, B.; Tarn, D.; Xue, M.; Wang, X.; Lin, S.; Ji, Z.; Li, R.; Garcia, F. L.; Yang, J.; Kirk, M. L.; Xia, T.; Zink, J. I.; Nel, A.; Brinker, C. J. Processing Pathway Dependence of Amorphous Silica Nanoparticle Toxicity: Colloidal vs. Pyrolytic. *J. Am. Chem. Soc.* **2012,** *134* (38), 15790-15804.
41. Mackowiak, S. A.; Schmidt, A.; Weiss, V.; Argyo, C.; von Schirnding, C.; Bein, T.; Bräuchle, C. Targeted Drug Delivery in Cancer Cells with Red-Light Photoactivated Mesoporous Silica Nanoparticles. *Nano Lett.* **2013,** *13* (6), 2576-2583.
42. Pan, L.; He, Q.; Liu, J.; Chen, Y.; Ma, M.; Zhang, L.; Shi, J. Nuclear-Targeted Drug Delivery of TAT Peptide-Conjugated Monodisperse Mesoporous Silica Nanoparticles. *J. Am. Chem. Soc.* **2012,** *134* (13), 5722-5725.
43. Zou, Z.; He, D.; He, X.; Wang, K.; Yang, X.; Qing, Z.; Zhou, Q. Natural Gelatin Capped Mesoporous Silica Nanoparticles for Intracellular Acid-Triggered Drug Delivery. *Langmuir* **2013,** *29* (41), 12804-12810.
44. Li, Y.; Wei, J.; Luo, W.; Wang, C.; Li, W.; Feng, S.; Yue, Q.; Wang, M.; Elzatahry, A. A.; Deng, Y.; Zhao, D. Tricomponent Coassembly Approach to Synthesize Ordered Mesoporous Carbon/Silica Nanocomposites and Their Derivative Mesoporous Silicas with Dual Porosities. *Chem. Mater.* **2014,** *26* (7), 2438-2444.

45. Bibent, N.; Charpentier, T.; Devautour-Vinot, S.; Mehdi, A.; Gaveau, P.; Henn, F.; Silly, G. Solid-State NMR Spectroscopic Studies of Propylphosphonic Acid Functionalized SBA-15 Mesoporous Silica: Characterization of Hydrogen-Bonding Interactions. *Eur. J. Inorg. Chem.* **2013,** *2013* (13), 2350-2361.
46. Policianova, O.; Brus, J.; Hruby, M.; Urbanova, M.; Zhigunov, A.; Kredatusova, J.; Kobera, L. Structural Diversity of Solid Dispersions of Acetylsalicylic Acid as Seen by Solid-State NMR. *Mol. Pharmaceutics* **2014,** *11* (2), 516-530.
47. Mao, K.; Kobayashi, T.; Wiench, J. W.; Chen, H.-T.; Tsai, C.-H.; Lin, V. S.-Y.; Pruski, M. Conformations of Silica-Bound (Pentefluorophenyl)propyl Groups Determined by Solid-State NMR Spectroscopy and Theoretical Calculations. *J. Am. Chem. Soc.* **2010,** *132* (35), 12452-12457.
48. Hara, K.; Akahane, S.; Wiench, J. W.; Burgin, B. R.; Ishito, N.; Lin, V. S.-Y.; Fukuoka, A.; Pruski, M. Selective and Efficient Silylation of Mesoporous Silica: A Quantitative Assessment of Synthetic Strategies by Solid-State NMR. *J. Phys. Chem. C* **2012,** *116* (12), 7083-7090.
49. Lee, D.; Monin, G.; Duong, N. T.; Lopez, I. Z.; Bardet, M.; Mareau, V.; Gonon, L.; De Paëpe, G. Untangling the Condensation Network of Organosiloxanes on Nanoparticles using 2D ^{29}Si-^{29}Si Solid-State NMR Enhanced by Dynamic Nuclear Polarization. *J. Am. Chem. Soc.* **2014,** *136* (39), 13781-13788.
50. Dai, F.-R.; Sambasivam, U.; Hammerstrom, A. J.; Wang, Z. Synthetic Supercontainers Exhibit Distinct Solution Versus Solid State Guest-Binding Behavior. *J. Am. Chem. Soc.* **2014,** *136* (20), 7480-7491.
51. Fritzinger, B.; Capek, R. K.; Lambert, K.; Martins, J. C.; Hens, Z. Utilizing Self-Exchange to Address the Binding of Carboxylic Acid Ligands to CdSe Quantum Dots. *J. Am. Chem. Soc.* **2010,** *132*, 10195-10201.
52. Donakowski, M. D.; Godbe, J. M.; Sknepnek, R.; Knowles, K. E.; de la Cruz, M. O.; Weiss, E. A. A Quantitative Description of the Binding Equilibria of para-Substituted Aniline Ligands and CdSe Quantum Dots. *J. Phys. Chem. C* **2010,** *114* (51), 22526-22534.
53. Moreels, I.; Martins, J. C.; Hens, Z. Solution NMR Techniques for Investigating Colloidal Nanocrystal Ligands: A Case Study on Trioctylphophine Oxide at InP Quantum Dots. *Sens. Actuators, B* **2006,** *126* (1), 283-288.
54. Yu, C.; Zhu, L.; Zhang, R.; Wang, X.; Guo, C.; Sun, P.; Xue, G. Investigation on the Mechanism of the Synthesis of Gold(I) Thiolate Complexes by NMR. *J. Phys. Chem. C* **2014,** *118* (19).
55. Hens, Z.; Martins, J. C. A Solution NMR Toolbox for Characterizing the Surface Chemistry of Colloidal Nanocrystals. *Chem. Mater.* **2013,** *25* (8), 1211-1221.
56. Brühwiler, D. Postsynthetic Functionalization of Mesoporous Silica. *Nanoscale* **2010,** *2* (887-892), 887.
57. Krezel, A.; Bal, W. A Formula for Correlating pK_a Values Determined in D_2O and H_2O. *J. Inorg. Biochem.* **2004,** *98*, 161-166.
58. Li, X.; Shantz, D. F. PFG NMR Investigations of Tetraalkylammonium-Silica Mixtures. *J. Phys. Chem. C* **2010,** *114* (18), 8449-8458.
59. Li, X. A.; Shantz, D. F. PFG NMR Investigations of TPA-TMA-Silica Mixtures. *Langmuir* **2011,** *27* (7), 3849-3858.

60. Rao, Y.; Antalek, B.; Minter, J.; Mourey, T.; Blanton, T.; Slater, G.; Slater, L.; Fornalik, J. Organic Solvent-Dispersed TiO_2 Nanoparticle Characterization. *Langmuir* **2009,** *25* (21), 12713-12720.
61. Rivas-Cardona, A.; Shantz, D. F. Pulsed Field Gradient NMR Investigations of Alkyltripropylammonium-Silica Mixtures. *J. Phys. Chem. C* **2010,** *114* (47), 20178-20188.
62. Rivas-Cardona, A.; Shantz, D. F. *In Situ* PFG NMR of Silicalite-1 Synthesis Mixtures. *J. Phys. Chem. C* **2011,** *115* (26), 13016-13026.
63. Hassinen, A.; Moreels, I.; de Mello Donegá, C.; Martins, J. C.; Hens, Z. Nuclear Magnetic Resonance Spectroscopy Demonstrating Dynamic Stabilization of CdSe Quantum Dots by Alkylamines. *J. Phys. Chem. Lett.* **2010,** *1* (2577-2581), 2577.
64. Coppel, Y.; Spataro, G.; Pagés, C.; Chaudret, B.; Maisonnat, A.; Kahn, M. L. Full Characterization of Colloidal Solutions of Long-Alkyl-Chain-Amine-Stabilized ZnO Nanoparticles by NMR Spectroscopy: Surface State, Equilibria, and Affinity. *Chem. - Eur. J.* **2012,** *18*, 5384-5393.
65. Fritzinger, B.; Moreels, I.; Lommens, P.; Koole, R.; Hens, Z.; Martins, J. C. *In Situ* Observation of Rapid Ligand Exchange in Colloidal Nanocrystal Suspensions Using Transfer NOE Nuclear Magnetic Resonance Spectroscopy. *J. Am. Chem. Soc.* **2009,** *131*, 3024-3032.
66. Barile, E.; Pellecchia, M. NMR-Based Approaches for the Identification and Optimization of Inhibitors of Protein-Protein Interactions. *Chem. Rev.* **2014,** *114* (9), 4749-4763.
67. Chen, J.; Brooks, I., C. L.;; Scheraga, H. A. Revisiting the Carboxylic Acid Dimers in Aqueous Solution: Interplay of Hydrogen Bonding, Hydrophobic Interactions, and Entropy. *J. Phys. Chem. B* **2008,** *112*, 242-249.
68. Macoas, E. M. S.; Myllyperkio, P.; Kunttu, H.; Pettersson, M. Vibrational Relaxation of Matrix-Isolated Carboxylic Acid Dimers and Monomers. *J. Phys. Chem. A* **2009,** *113*, 7227-7234.
69. Gomes, R.; Hassinen, A.; Szczygiel, A.; Zhao, Q.; Vantomme, A.; Martins, J. C.; Hens, Z. Binding of Phosphonic Acids to CdSe Quantum Dots: A Solution NMR Study. *J. Phys. Chem. Lett.* **2011,** *2* (3), 145.
70. Caragheorgheopol, A.; Chechik, V. Mechanistic Aspects of Ligand Exchange in Au Nanoparticles. *Phys. Chem. Chem. Phys.* **2008,** *10*, 5029-5041.
71. Wu, D.; Chen, A.; Johnson Jr., C. S. An Improved Diffusion-Ordered Spectroscopy Experiment Incorporating Bipolar-Gradient Pulses. *J. Magn. Reson., Ser. A* **1995,** *115*, 260-264.
72. Chen, L. Q.; Fang, L.; Ling, J.; Ding, C. Z.; Kang, B.; Huang, C. Z. Nanotoxicity of Silver Nanoparticles to Red Blood Cells: Size Dependent Adsorption, Uptake, and Hemolytic Activity. *Chem. Res. Toxicol.* **2015,** *28* (3), 501-509.
73. Seabra, A. B.; Paula, A. J.; de Lima, R.; Alves, O. L.; Durán, N. Nanotoxicity of Graphene and Graphene Oxide. *Chem. Res. Toxicol.* **2014,** *27* (2), 159-168.
74. Huang, C.-C.; Tsai, C.-Y.; Sheu, H.-S.; Chuang, K.-Y.; Su, C.-H.; Jen, U.-S.; Cheng, F.-Y.; Su, C.-H.; Lei, H.-Y.; Yeh, C. S. Enhancing Transversal Relaxation for Magnetite Nanoparticles in MR Imaging Using Gd^{3+}-Chelated Mesoporous Silica Shells. *ACS Nano* **2011,** *5* (5), 3905-3916.

75. Nayab, S.; Farrukh, A.; Oluz, Z.; Tuncel, E.; Tariq, S. R.; ur Rahman, H.; Kirtchhoff, K.; Duran, H.; Yameen, B. Design and Fabrication of Branched Polyamine Functionalized Mesoporous Silica: An Efficient Absorbent for Water Remediation. *ACS Appl. Mater. Interfaces* **2014,** *6* (6), 4408-4417.
76. Partlett, C. M. A.; Bruce, D. W.; Hondow, N. S.; Lee, A. F.; Wilson, K. Support-Enhanced Selective Aerobic Alcohol Oxidation over Pd/Mesoporous Silicas. *ACS Catal.* **2011,** *1* (6), 636-640.
77. Yang, G.; Gai, S.; Qu, F.; Yang, P. SiO_2@YBO_3:Eu^{3+} Hollow Mesoporous Spheres for Drug Delivery Vehicle. *ACS Appl. Mater. Interfaces* **2013,** *5* (12), 5788-5796.
78. Asefa, T.; Tao, Z. Biocompatibility of Mesoporous Silica Nanoparticles. *Chem. Res. Toxicol.* **2012,** *25* (11), 2265-2284.
79. Zhang, H. Processing Pathway Dependence of Amorphous Silica Nanoparticle Toxicity-Colloidal Versus Pyrolytic. *J. Am. Chem. Soc.* **2012,** *134* (38), 15790-15804.
80. Duan, J.; Yu, Y.; Li, Y.; Yu, Y.; Li, Y.; Zhou, X.; Huang, P.; Sun, Z. Toxic Effect of Silica Nanoparticles on Endothelial Cells Through DNA Damage Response Via Chk1-Dependent G2/M Checkpoint. *PLoS One* **2013,** *8* (4).
81. Rimola, A.; Costa, D.; Sodupe, M.; Lambert, J.-F.; Ugliengo, P. Silica Surface Features and Their Role in the Adsorption of Biomolecules: Computational Modeling and Experiments. *Chem. Rev.* **2013,** *113* (6), 4216-4313.
82. Samri, M. T. A.; Biradar, A. V.; Alsuwaidi, A. R.; Balhaj, G.; Al-Hammadi, S.; Shehab, S.; Al-Salam, S.; Tariq, S.; Pramathan, T.; Benedict, S.; Asefa, T.; Souid, A.-K. In Vitro Biocompatibility of Calcined Mesoporous Silica Particles and Fetal Blood Cells. *Int. J. Nanomed.* **2012,** *7*, 3111-3121.
83. Murashov, V.; Harper, M.; Demchuk, E. Impact of Silanol Surface Density on the Toxicity of Silica Aerosols Measured by Erythrocyte Haemolysis *J. Occup. Environ. Hyg.* **2006,** *3* (12), 718-723.
84. Ghiazza, M.; Polimeni, M.; Fenoglio, I.; Gazzano, E.; Ghigo, D.; Fubini, B. Does Vitreous Silica Contradict the Toxicity of the Crystalline Silica Paradigm? *Chem. Res. Toxicol.* **2010,** *23*, 620-629.
85. Zhang, H.; Ji, Z.; Xia, T.; Meng, H.; Low-Kam, C.; Liu, R.; Pokhrel, S.; Lin, S.; Wang, X.; Liao, Y.-P.; Wang, M.; Li, L.; Rallo, R.; Damoiseaux, R.; Telesca, D.; Mädler, L.; Cohen, Y.; Zink, J. I.; Nel, A. E. Use of Metal Oxide Nanoparticle Band Gap to Develop a Predictive Paradigm for Oxidative Stress and Acute Pulmonary Inflammation. *ACS Nano* **2012,** *6* (5), 4349-4368.
86. Xia, T.; Kovochich, M.; Liong, M.; Mädler, L.; Gilbert, B.; Shi, H.; Yeh, J. I.; Zink, J. I.; Nel, A. E. Comparison of the Mechanism of Toxicity of Zinc Oxide and Cerium Oxide Nanoparticles Based on Dissolution and Oxidative Stress Properties. *ACS Nano* **2008,** *2* (10), 2121-2134.
87. Xia, T.; Kovochich, M.; Brant, J.; Hotze, M.; Sempf, J.; Oberley, T.; Sioutas, C.; Yeh, J. I.; Wiesner, M. R.; Nel, A. E. Comparison of the Abilities of Ambient and Manufactured Nanoparticles to Induce Cellular Toxicity According to an Oxidative Stress Paradigm. *Nano Lett.* **2006,** *6* (8), 1794-1807.
88. Yildirim, A.; Ozgur, E.; Bayindir, M. Impact of Mesoporous Silica Nanparticle Surface Functionality on Hemolytic Activity, Thrombogenicity, and Non-Specific Protein Adsorption. *J. Mater. Chem. B* **2013,** *1*, 1909-1920.

89. Marzaioli, V.; A., A.-P. J.; Weichenmeier, I.; Luxenhofer, G.; Wiemann, M.; Landsiedel, R.; Wohlleben, W.; Eiden, S.; Mempel, M.; Behrendt, H.; Schmidt-Weber, C.; Gutermuth, J.; Alessandrini, F. Surface Modification of Silica Nanoparticles are Crucial for Their Inert Versus Proinflammatory and Immunomodulatory Properties. *Int. J. Nanomed.* **2014,** *9*, 2815-2832.
90. Townson, J. L.; Lin, Y.-S.; Agola, J. O.; Carnes, E. C.; Leong, H. S.; Lewis, J. D.; Haynes, C. L.; Brinker, C. J. Re-Examining the Size/Charge Paradigm: Differing *in Vivo* Characteristics of Size- and Charge-Matched Mesoporous Silica Nanoparticles. *J. Am. Chem. Soc.* **2013,** *135* (43), 16030-16033.
91. He, X.; Nie, H.; Wang, K.; Tan, W.; Wu, X.; Zhang, P. *In Vivo* Study of Biodistribution and Urinary Excretion of Surface-Modified Silica Nanoparticles. *Anal. Chem.* **2008,** *80* (24), 9597-9603.
92. Lehman, S. E.; Tataurova, Y.; Mueller, P. S.; Santhana Mariappan, S. V.; Larsen, S. C. Ligand Characterization of Covalently-Functionalized Mesoporous Silica Nanoparticles: An NMR Toolbox Approach. *J. Phys. Chem. C* **2014,** *118* (51), 29943-29951.
93. Lee, J. Y.; Kim, Y.-J.; Kim, H. J.; Kim, Y.-S.; Park, W. Immunostimulatory Effect of Laminarin on RAW 264.7 Mouse Macrophages. *Molecules* **2012,** *17*, 5404-5411.
94. Kusaka, T.; Nakayama, M.; Nakamura, K.; Ishimiya, M.; Furusawa, E.; Ogasawara, K. Effect of Silica Particle Size on Macrophage Inflammatory Responses. *PLoS One* **2014,** *9* (3).
95. Ahmad, J.; Ahamed, M.; Akhtar, M. J.; Alrokayan, S. A.; Siddigui, M. A.; Musarrat, J.; Al-Khedhairy, A. A. Apoptosis Induction by Silica Nanoparticles Mediated Through Reactive Oxygen Species in Human Liver Cell Line HepG2. *Toxicol. Appl. Pharmacol.* **2012,** *259*, 160-168.
96. Yu, T.; Malugin, A.; Ghandehari, H. Impact of Silica Nanoparticle Design on Cellular Toxicity and Hemolytic Activity. *ACS Nano* **2011,** *5* (7), 5717-5728.
97. Villamena, F. A.; Hadad, C. M.; Zweier, J. L. Kinetic Study and Theoretical Analysis of Hydroxyl Radical Trapping and Spin Adduct Decay of Alkoxycarbonyl and Dialkoxyphosphoryl Nitrones in Aqueous Media. *J. Phys. Chem. A* **2003,** *107*, 4407-4414.
98. Sanglioglu, S.; Williams, C. M.; Samavati, L.; Butler, N. S.; Wang, G.; McCray, P. B.; Ritchies, T. C.; Hunninghake, G. W.; Zandi, E.; Englehardt, J. F. Lipopolysaccharide Induces Rac1-Dependent Reactive Oxygen Species Formation and Coordinates Tumor Necrosis Factor-α. *J. Biol. Chem.* **2001,** *276* (32), 30188-30198.
99. Lind, J.; Merényi, G. Kinetic and Thermodynamic Properties of the Aminoxyl ($NH_2O^{\cdot}$) Radical. *J. Phys. Chem. A* **2006,** *110*, 192-197.
100. Buettner, G. R.; Scott, B. D.; Kerber, R. E.; Mugge, A. Free Radicals from Plastic Syringes. *Free Radicals Biol. Med.* **1991,** *11*, 69-70.
101. Stoll, S.; Schweiger, A. EasySpin, a Comprehensive Software Package for Spectral Simulation and Analysis in EPR. *J. Magn. Reson.* **2006,** *178* (1), 42-55.
102. Lin, Y.-S.; Haynes, C. L. Impacts of Mesoporous Silica Nanoparticle Size, Pore Ordering, and Pore Integrity on Hemolytic Activity. *J. Am. Chem. Soc.* **2010,** *132* (13), 4834-4842.

103. Michel, C.; Herzog, S.; de Capitani, C.; Burkhardt-Holm, P.; Pietsch, C. Natural Mineral Particles Are Cytotoxic to Rainbow Trout Gill Epithelial Cells *In Vitro*. *PLoS One* **2014,** *9* (7), 1-10.
104. Fridovich, I. Superoxide Radical and Superoxide Dismutases. *Annu. Rev. Biochem.* **1995,** *64*, 97-112.
105. Kurtz-Chalot, A.; Klein, J.-P.; Pourchez, J.; Boudard, D.; Bin, V.; Sabido, O.; Marmuse, L.; Cottier, M.; Forest, V. Quantification of Nanoparticle Endocytosis Based on Double Fluorescent pH-Sensitive Nanoparticles. *Biomed Microdevices* **2015,** *17* (2), 1-12.
106. Giorgio, M.; Trinei, M.; Migliaccio, E.; Pelicci, P. G. Hydrogen Peroxide: A Metabolic By-Product or a Common Mediator of Ageing Signals? *Nat. Rev. Mol. Cell Biol.* **2007,** *8*, 722-728.
107. Zhang, H.; Chen, T.; Jiang, J.; Wong, Y.-S.; Yang, F.; Zheng, W. Selenium-Containing Allophycocyanin Purified from Selenium-Enriched *Spirulina platensis* Attenuates AAPH-Induced Oxidative Stress in Human Erythrocytes through Inhibition of ROS Generation. *J. Agric. Food Chem* **2011,** *59* (16), 8683-8690.
108. Imlay, J. Pathways of Oxidative Damage. *Annu. Rev. Microbiol.* **2003,** *57*, 395-418.
109. Ponniah, M.; Billett, E. E.; De Girolamo, L. A. Bisphenol A Increases BeWo Tophoblast Survival in Stress-Induced Paradigms through Regulation of Oxidative Stress and Apoptosis. *Chem. Res. Toxicol.* **2015,** *28*, 1693-1703.
110. Du, Y.; Rabani, J. Flocculation-Induced Homolysis of Hydrogen Peroxide in Aqueous Colloid Solution of Titanium Dioxide Nanoparticles. *J. Phys. Chem. B* **2006,** *110*, 6123-6128.
111. Fogolari, F.; Corazza, A.; Toppo, S.; Tosatto, S. C. E.; Viglino, P.; Ursini, F.; Esposito, G. Studying Interactions by Molecular Dynamics Simulations at High Concentration. *J. Biomed. Biotechnol.* **2012,** *2012*, 1-9.
112. Saripalli, K. P.; Serne, R. J.; Meyer, P. D.; McGrail, B. P. Prediction of Diffusion Coefficients in Porous Media Using Tortuosity Factors Based on Interfacial Areas. *Groundwater* **2002,** *40* (4), 346-352.
113. Zhang, H.; Hassanali, A. A.; Shin, Y. K.; Knight, C.; Singer, S. J. The Water-Amorphous Silica Interface: Analysis of the Stern Layer and Surface Conduction. *J. Chem. Phys.* **2011,** *134* (1-10).
114. Maiolo, D.; Bergese, P.; Mahon, E.; Dawson, K. A.; Monopoli, M. P. Surfactant Titration of Nanoparticle-Protein Corona. *Anal. Chem.* **2014,** *86* (24), 12055-12063.
115. Hu, W.; Peng, C.; Lv, M.; Li, X.; Zhang, Y.; Chen, N.; Fan, C.; Huang, Q. Protein Corona-Mediated Mitigation of Cytotoxicity of Graphene Oxide. *ACS Nano* **2011,** *5* (5), 3693-3700.
116. Gebauer, J. S.; Malissek, M.; Simon, S.; Knauer, S. K.; Maskos, M.; Stauber, R. H.; Peukert, W.; Treuel, L. Impact of the Nanoparticle-Protein Corona on Colloidal Stability and Protein Structure. *Langmuir* **2012,** *28* (25), 9673-9679.
117. Treuel, L.; Brandholt, S.; Maffre, P.; Wiegele, S.; Shang, L.; Nienhaus, G. U. Impact of Protein Modification on the Protein Corona on Nanoparticles and Nanoparticle-Cell Interactions. *ACS Nano* **2014,** *8* (1), 503-513.

118. Fleischer, C. C.; Payne, C. K. Nanoparticle Surface Charge Mediates the Cellular Receptors Used by Protein-Nanoparticle Complexes. *J. Phys. Chem. B* **2012,** *116* (30), 8901-8907.
119. Casals, E.; Pfaller, T.; Duschl, A.; Oostingh, G. J.; Puntes, V. Time Evolution of the Nanoparticle Protein Corona. *ACS Nano* **2010,** *4* (7), 3623-3632.
120. Tenzer, S.; Docter, D.; Kuharev, J.; Musyanovych, A.; Fetz, V.; Hecht, R.; Schlenk, F.; Fischer, D.; Kiouptsi, K.; Reinhardt, C.; Landfester, K.; Schild, H.; Maskos, M.; Knauer, S. K.; Stauber, R. H. Rapid Formation of Plasma Protein Corona Critically Affects Nanoparticle Pathophysiology. *Nat. Nanotechnol.* **2013,** *8*, 772-781.
121. Zhao, X.; Lu, D.; Hao, F.; Liu, R. Exploring the Diameter and Surface Dependent Conformational Changes in Carbon Nanotube-Protein Corona and the Related Cytotoxicity. *J. Hazard. Mater.* **2015,** *292*, 98-107.
122. Elward, J. M.; Iruayanathan, F. J.; Nangia, S.; Chakraborty, A. Optical Signature of Formation of Protein Corona in the Firefly Luciferase-CdSe Quantum Dot Complex. *J. Chem. Theory Comput.* **2014,** *10* (12), 5224-5228.
123. Lynch, I.; Dawson, K. A. Protein-Nanoparticle Interactions. *Nano Today* **2008,** *3*, 40-47.
124. Cifuentes-Rius, A.; de Puig, H.; Kah, J. C. Y.; Borros, S.; Hamad-Schifferli, K. Optimizing the Properties of the Protein Corona Surrounding Nanoparticles for Tuning Payload Release. *ACS Nano* **2013,** *7* (11), 10066-10074.
125. Milani, S.; Bombelli, F. B.; Pitek, A. S.; Dawson, K. A.; Rädler, J. Reversible *versus* Irreversible Binding of Transferrin to Polystyrene Nanoparticles: Soft and Hard Corona. *ACS Nano* **2012,** *6* (3), 2532-2541.
126. Murphy, C. J.; Vartanian, A. M.; Geiger, F. M.; Hamers, R. J.; Pedersen, J.; Cui, Q.; Haynes, C. L.; Carlson, E. E.; Hernandez, R.; Klaper, R. D.; Orr, G.; Rosenzweig, Z. Biological Responses to Engineered Nanomaterials: Needs for the Next Decade. *ACS Cent. Sci.* **2015,** *1* (3), 117-123.
127. Liu, W.; Rose, J.; Plantevin, S.; Auffan, M.; Bottero, J.-Y.; Vidaud, C. Protein Corona Formation for Nanomaterials and Proteins of a Similar Size: Hard or Soft Corona? *Nanoscale* **2013,** *5* (4), 1658-1668.
128. Wan, S.; Kelly, P. M.; Mahon, E.; Stöckmann, H.; Rudd, P. M.; Caruso, F.; Dawson, K. A.; Yan, Y.; Monopoli, M. P. The "Sweet" Side of the Protein Corona: Effects of Glycosylation on Nanoparticle-Cell Interactions. *ACS Nano* **2015,** *9* (2), 2157-2166.
129. Mudalige, T. K.; Qu, H.; Linder, S. W. Asymmetric Flow-Field Flow Fractionation Hypenated ICP-MS as an Alternative to Cloud Point Extraction for Quantification of Silver Nanoparticles and Silver Speciation: Application for Nanoparticles with a Protein Corona. *Anal. Chem.* **2015,** *87* (14), 7395-7401.
130. Ritz, S.; Schöttler, S.; Kotman, N.; Baier, G.; Musyanovych, A.; Kuharev, J.; Landfester, K.; Schild, H.; Jahn, O.; Tenzer, S.; Mailänder, V. Protein Corona of Nanoparticles: Distinct Proteins Regulate the Cellular Uptake. *Biomacromolecules* **2015,** *16* (4), 1311-1321.
131. Barnard, A. S. How Can *Ab Initio* Simulations Address Risks in Nanotech? *Nat. Nanotechnol.* **2009,** *4*, 332-335.

132. Tavanti, F.; Pedone, A.; Menziani, M. C. A Closer Look Into the Ubiquitin Corona on Gold Nanoparticles by Computational Studies. *New J. Chem.* **2015,** *39*, 2474-2482.
133. Stebounova, L. V.; Guio, E.; Grassian, V. H. Silver Nanoparticles in Simulated Biological Media: A Study of Aggregation, Sedimentation, and Dissolution. *J. Nanopart. Res.* **2013,** *13* (1), 233-244.
134. Nymark, P.; Alstrup, J. K.; Suhonen, S.; Kembouche, Y.; Vippola, M.; Kleinjans, J.; Catalán, J.; Norppa, H.; van Delft, J.; Briedé, J. J. Free Radical Scavenging and Formation by Multi-Walled Carbon Nanotubes in Cell Free Conditions and in Human Bronchial Epithelial Cells. *Part. Fibre Toxicol.* **2014,** *11* (4), 1-18.
135. Borisova, D.; Möhwald, H.; Shchukin, D. G. Mesoporous Silica Nanoparticles for Active Corrosion Protection. *ACS Nano* **2011,** *5* (3), 1939-1946.
136. Kaya, M.; Zahmakiran, M.; Özkar, S.; Volkan, M. Copper(0) Nanoparticles Supported on Silica-Coated Cobalt Ferrite Magnet Particles: Cost Effective Catalyst in the Hydrolysis of Ammonia-Borane with an Exceptional Reusability Performance. *ACS Appl. Mater. Interfaces* **2012,** *4* (8), 3866-3873.
137. Liberman, A.; Wu, Z.; V., B. C.; Viveros, R.; Blair, S. L.; Ellies, L. G.; Vera, D. R.; Mattrey, R. F.; Kummel, A. C.; Trogler, W. C. Color Doppler Ultrasound and Gamma Imaging of Intratumorally Injected 500 nm Iron-Silica Nanoshells. *ACS Nano* **2013,** *7* (7), 6367-6377.
138. Zhang, Y.; Ang, C. Y.; Li, M.; Tan, S. Y.; Qu, Q.; Luo, Z.; Zhao, Y. Polymer Coated Hollow Mesoporous Silica Nanoparticles for Triple-Responsive Drug Delivery. *ACS Appl. Mater. Interfaces* **2015,** *7* (32), 18179-18187.
139. Lin, C.-J.; Huang, S.-H.; Lai, N.-C.; Yang, C.-M. Efficient Room-Temperature Aqueous-Phase Hydrogenation of Phenol to Cyclohexanone Catalyzed by Pd Nanoparticles Supported on Mesoporous MMT-1 Silica with Unevenly Distributed Functionalities. *ACS Catal.* **2015,** *5* (7), 4121-4129.
140. Pal, S.; Patra, A. S.; Ghorai, S.; Sarkar, A. K.; Das, R.; Sarkar, S. Modified Guar Gum/SiO_2: Development and Application of a Novel Hybrid Nanocomposite as a Flocculant for the Treatment of Wastewater. *Environ. Sci.: Water Res. Technol.* **2015,** *1*, 84-95.
141. Giménez, C.; de la Torre, C.; Gorbe, M.; Aznar, E.; Sancenón, F.; Murguía, J. R.; Martínez-Máñ. Gated Mesoporous Silica Nanoparticles for the Controlled Delivery of Drugs in Cancer Cells. *Langmuir* **2015,** *31* (12), 3753-3762.
142. Huang, X.; Zhang, T.; Goswami, A.; Luo, F.; Asefa, T. Glutathione-Triggered Release of Model Drug Molecules from Mesoporous Silica Nanoparticles *via* a Non-Redox Process. *RSC Adv.* **2015,** *5*, 28836-28839.
143. Aburawi, E. H.; Qureshi, M. A.; Oz, D.; Jayaprakash, P.; Tariq, S.; Hameed, R. S.; Das, S.; Goswami, A.; Biradar, A.; Asefa, T.; Souid, A. K.; Adgehate, E.; Howarth, F. C. Biocompatibility of Calcined Mesoporous Silica Particles with Ventricular Myocyte Structure and Function. *Chem. Res. Toxicol.* **2013,** *26* (1), 26-36.
144. Foroozandeh, P.; Aziz, A. A. Merging Worlds on Nanomaterials and Biological Environment: Factors Governing Protein Corona Formation on Nanoparticles and Its Biological Consequences. *Nanoscale Res. Lett.* **2015,** *10*, 1-12.

145. Lee, Y. K.; Choi, E.-J.; Webster, T. J.; Kim, S.-H.; Khang, D. Effect of the Protein Corona on Nanoparticles for Modulating Cytotoxicity and Immunotoxicity. *Int. J. Nanomed.* **2015,** *10*, 97-113.
146. Shahabi, S.; Treccani, L.; Dringen, R.; Rezwan, K. Modulation of Silica Nanoparticle Uptake into Human Osteoblast Cells by Variation of the Ratio of Amino and Sulfonate Surface Groups: Effects of Serum. *ACS Appl. Mater. Interfaces* **2015,** *7* (25), 13821-13833.
147. Mudunkotuwa, I. A.; Grassian, V. H. Biological and Environmental Media Conrol Oxide Nanoparticle Surface Composition: The Roles of Biological Components (Proteins and Amino Acids), Inorganic Oxyanions and Humic Acid. *Environ. Sci.: Nano* **2015,** *2*, 429-439.
148. Tenzer, S.; Docter, D.; Rosfa, S.; Wlodarski, A.; Kuharev, J.; Rekik, A.; Knauer, S. K.; Bantz, C.; Nawroth, T.; Bier, C.; Sirirattanapan, J.; Mann, W.; Treuel, L.; Zellner, R.; Maskos, M.; Schild, H.; Stauber, R. H. Nanoparticle Size is a Critical Physico-chemical Determinant of the Human Blood Plasma Corona: A Comprehensive Quantitative Proteomic Analysis. *ACS Nano* **2011,** *5* (9), 7155-7167.
149. Vertegel, A. A.; Siegel, R. W.; Dordick, J. S. Silica Nanoparticle Size Influences the Structure and Enzymatic Activity of Adsorbed Lysozyme. *Langmuir* **2004,** *20* (16), 6800-6807.
150. McClellan, S. J.; Franses, E. I. Adsorption of Bovine Serum Albumin at Solid/Aqueous Interfaces. *Colloids Surf., A* **2005,** *260*, 265-275.
151. Su, T. J.; Lu, J. R.; Thomas, R. K.; Cui, Z. F. Effect of pH on the Adsorption of Bovine Serum Albumin at the Silica/Water Interface Studied by Neutron Reflection. *J. Phys. Chem. B* **1999,** *103* (18), 3727-3736.
152. Yeung, K. M.; Lu, Z. J.; Cheung, N. H. Adsorption of Bovine Serum Albumin on Fused Silica: Elucidation of Protein-Protein Interactions by Single-Molecule Fluorescence Microscopy. *Colloids Surf., B* **2009,** *69* (246-250), 246.
153. Greenfield, N. J. Using Circular Dichroism Spectra to Estimate Protein Secondary Structure. *Nat. Protoc.* **2006,** *1* (6), 2876-2890.
154. Whitmore, L.; Wallace, B. A. Protein Secondary Structure Analyses from Circular Dichroism Spectroscopy: Methods and Reference Databases. *Biopolymers* **2008,** *89*, 392-400.
155. Sreerama, N.; Venyaminov, S. Y.; Woody, R. W. Estimation of Protein Secondary Structure from Circular Dichroism Spectra. *Anal. Biochem.* **2000,** *287*, 243-251.
156. Na, H. B.; Palui, G.; Rosenberg, J. T.; Ji, X.; Grant, S. C.; Mattoussi, H. Multidentate Catechol-Based Polyethylene Glycol Oligomers Provide Enhanced Stability and Biocompatibility to Iron Oxide Nanoparticles. *ACS Nano* **2012,** *6* (1), 389-399.
157. Moore, G. E.; Gerner, R. E.; Franklin, H. A. Culture of Normal Human Leukocytes. *JAMA* **1967,** *199* (8), 519-524.
158. Mudunkotuwa, I. A.; Al-Minshid, A.; Grassian, V. H. ATR-FTIR Spectroscopy as a Tool to Probe Surface Adsorption on Nanoparticles at the Liquid-Solid Interface in Environmentally and Biologically Relevant Media. *Analyst* **2014,** *139*, 870-881.
159. Boulos, S. P.; Davis, T. A.; Yang, J.-A.; Lohse, S. E.; Alkilany, A. M.; Holland, L. A.; Murphy, C. J. Nanoparticle-Protein Interactions: A Thermodynamic and Kinetic

Study of the Adsorption of Bovine Serum Albumin to Gold Nanoparticle Surfaces. *Langmuir* **2013,** *29* (48), 14984-14996.
160. Clemments, A. M.; Botella, P.; Landry, C. C. Protein Adsorption From Biofluids on Silica Nanoparticles: Corona Analysis as a Function of Particle Diameter and Porosity. *ACS Appl. Mater. Interfaces* **2015,** *7* (39), 21682-21689.
161. Soteropulos, C. E.; Zurick, K. M.; Bernards, M. T.; Hunt, H. K. Tailoring the Protein Adsorption Properties of Whispering Gallery Mode Optical Biosensors. *Langmuir* **2012,** *28* (44), 15743-15750.
162. Michel, R.; Pasche, S.; Textor, M.; Castner, D. G. Influence of PEG Architecture on Protein Adsorption and Conformation. *Langmuir* **2005,** *21* (26), 12327-12332.
163. Benhabbour, S. R.; Sheardown, H.; Adronov, A. Protein Resistance of PEG-Functionalized Dendronized Surfaces: Effect of PEG Molecular Weight and Dendron Generation. *Macromolecules* **2008,** *41*, 4817-4823.
164. Larson, T. A.; Joshi, P. P.; Sokolov, K. Preventing Protein Adsorption and Macrophage Uptake of Gold Nanoparticles *via* a Hydrophobic Shield. *ACS Nano* **2012,** *6* (10), 9182-9190.
165. Perry, J. L.; Reuter, K. G.; Kai, M. P.; Herlihy, K. P.; Jones, S. W.; Luft, J. C.; Napier, M.; Bear, J. E.; DeSimone, J. M. PEGylated PRINT Nanoparticles: The Impact of PEG Density on Protein Binding, Macrophage Association, Biodistribution, and Pharmacokinetics. *Nano Lett. 12* (10), 5304-5310.
166. Clemments, A. M.; Muniesa, C.; Landry, C. C.; Botella, P. Effect of Surface Properties in Protein Corona Development on Mesoporous Silica Nanoparticles. *RSC Adv.* **2014,** *4*, 29314-29138.
167. Reed, R. G.; Feldhoff, R. C.; Clute, O. L.; Peters, J. T. Fragments of Bovine Serum Albumin Produced by Limited Proteolysis. Conformation and Ligand Binding. *Biochemistry* **1975,** *14* (21), 4578-4583.
168. Takeda, K.; Shigeta, M.; Aoki, K. Secondary Structures of Bovine Serum Albumin in Anionic and Cationic Surfactant Solutions. *J. Colloid Inter. Sci* **1987,** *117* (1), 120-126.
169. Lehman, S. E.; S., M. A.; Mueller, P. S.; Salem, A. K.; Grassian, V. H.; Larsen, S. C. Silica Nanoparticle-Generated ROS as a Predictor of Cellular Toxicity: Mechanistic Insights and Safety by Design. *Environ. Sci.: Nano* **2015,** *3*, 56-66.
170. Salvati, A.; Pitek, A. S.; Monopoli, M. P.; Prapainop, K.; Bombelli, F. B.; Hristov, D. R.; Kelly, P. M.; Aberg, C.; Mahon, E.; Dawson, K. A. Transferrin-Functionalized Nanoparticles Lose Their Targeting Capabilities When a Biomolecule Corona Adsorbs on the Surface. *Nat. Nanotechnol.* **2013,** *8* (2), 137-143.
171. Lehman, S. E.; Mudunkotuwa, I. A.; Grassian, V. H.; Larsen, S. C. Nano-Bio Interactions of Porous and Nonporous Silica Nanoparticles of Varied Surface Chemistry: A Structural, Kinetic, and Thermodynamic Study of Protein Adsorption from RPMI Culture Medium. *Langmuir* **2016,** *32* (3), 731-742.
172. Egodawatte, S.; Datt, A.; Burns, E. A.; Larsen, S. C. Chemical Insight Into the Adsorption of Chromium(III) on Iron Oxide/Mesoporous Silica Nanocomposites. *Langmuir* **2015,** *31* (27), 7553-7562.